Phase-Matched Four-Wave Mixing of Isolated Waveguide Modes of High-Intensity Femtosecond Pulses in a Hollow Photonic-Crystal Fiber

S. O. Konorov[1], E. E. Serebryannikov[1], A. A. Ivanov[1], D. A. Akimov[2], M. V. Alfimov[2], and A. M. Zheltikov[1, 3, *]

[1] *Physical Department, Moscow State University, Vorob'evy gory, Moscow, 119899 Russia*
* e-mail: zheltikov@top.phys.msu.su
[2] *Center of Photochemistry, Russian Academy of Sciences, ul. Novatorov 7a, Moscow, 117421 Russia*
[3] *International Laser Center, Moscow State University, Vorob'evy gory, Moscow, 119899 Russia*
Received March 12, 2004

Hollow-core photonic-crystal fibers with a special dispersion profile are shown to allow phase-matched nonlinear optical interactions of isolated air-guided modes of high-intensity femtosecond laser pulses confined in the hollow fiber core. We present theoretical and experimental studies of the four-wave mixing of fundamental and second-harmonic pulses of a Cr:forsterite laser with an initial pulse duration of about 50 fs and an intensity on the order of 10^{14} W/cm^2 in waveguide modes of a hollow photonic-crystal fiber with a core diameter of about 13 μm. © 2004 MAIK "Nauka/Interperiodica".

PACS numbers: 42.65.Wi; 42.81.Qb; 42.70.Qs

Nonlinear optics of high-intensity ultrashort laser pulses is one of the most interesting and rapidly growing areas of optical physics. Nonlinear optical interactions of high-intensity femtosecond laser pulses are at the heart of several new physical phenomena, including high-order harmonic generation [1, 2], and allow unprecedentedly short, attosecond pulses to be synthesized [3–5].

Hollow waveguides [6] are intensely used in modern high-power laser systems that provide large nonlinear-optical interaction lengths for intense laser pulses, thereby improving the efficiency of nonlinear-optical processes [7]. Such waveguides allow the efficient nonlinear-optical spectral transformations of high-intensity ultrashort pulses with no damage of the waveguide core as a result of optical breakdown. Self-phase modulation [8] and stimulated Raman scattering [9] in a gas filling the core of a hollow waveguide open the ways to synthesize pulses as short as a few cycles of the optical field. Hollow waveguides can also radically enhance high-order harmonic generation [10–12] and improve the sensitivity of gas-phase analysis based on four-wave mixing spectroscopy [13, 14].

Air-guided modes in standard hollow waveguides with a solid dielectric cladding are leaky [6], with the loss magnitude scaling as λ^2/a^3 with the fiber inner radius a and the radiation wavelength λ, which dictates the choice of hollow waveguides with a core diameter of 100–500 μm for nonlinear-optical experiments. Such waveguides are essentially multimode, with higher-order air-guided modes often having a notice-

able impact on nonlinear-optical interactions of ultrashort pulses [14, 15].

Optical losses of air-guided modes can be radically reduced by using hollow fibers with a two-dimensionally periodic microstructure cladding—photonic-crystal fibers (PCFs) [16, 17]. The periodic structure of the cladding in such fibers gives rise to photonic band gaps—frequency ranges where radiation cannot penetrate into the periodic structure. The reflectivity of the periodic cladding within these frequency ranges is much higher than the reflectivity of the cladding material, substantially reducing the losses of air-guided modes in the hollow fiber core [16–18]. Hollow PCFs can support isolated modes guided in the gas filling the PCF core [17, 18], radically enhancing a broad class of nonlinear-optical interactions in the gas phase, including stimulated Raman scattering [19], four-wave mixing (FWM) [20], and self-phase modulation [21]. Recent experiments [22] have demonstrated a transmission of megawatt optical pulses in hollow PCFs in the regime of temporal solitons.

In this work, we will show that hollow-core PCFs with a special dispersion profile allow phase-matched nonlinear-optical interactions of isolated air-guided modes of high-intensity femtosecond laser pulses confined in the hollow fiber core. We will present theoretical and experimental studies of the four-wave mixing of fundamental and second-harmonic pulses of a Cr:forsterite laser with an initial pulse duration of about 50 fs and an intensity on the order of 10^{14} W/cm^2 in
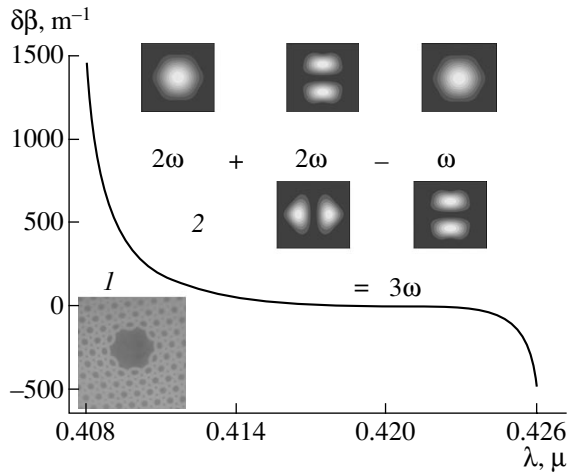
Fig. 1. The mismatch $\delta\beta = \beta_{3\omega} - \beta'_{2\omega} - \beta''_{2\omega} + \beta_\omega$ of the propagation constants β_ω, $\beta'_{2\omega}$, $\beta''_{2\omega}$, and $\beta_{3\omega}$ of air-guided modes involved in the four-wave mixing $3\omega = 2\omega + 2\omega - \omega$ (2ω and ω are the frequencies of the pump field) in a hollow PCF with a period of the photonic-crystal cladding equal to 4.6 μm and a core diameter of approximately 13 μm. The insets show (*1*) an image of the PCF cross section and (*2*) intensity profiles for the air-guided modes of the hollow PCF involved in the FWM process.

waveguide modes of a hollow PCF with a core diameter of about 13 μm.

Hollow-core PCFs designed for the purposes of these experiments had a period of the photonic-crystal cladding of about 4.6 μm and a core diameter of approximately 13 μm. A typical structure of the PCF cross section is shown in inset *1* in Fig. 1. The PCFs were fabricated with the use of a standard technology, described in detail elsewhere [18]. Transmission spectra of hollow-core PCFs display characteristic well-pronounced isolated passbands, related to the photonic band gaps of the cladding. The passbands in PCF transmission were tuned by changing the structure of the fiber cladding [23].

To design the dispersion of waveguide modes and transmission spectra of hollow PCFs, we developed a numerical procedure solving [24] the vectorial wave problem for the transverse components of the electric field, $E_x(x, y)$ and $E_y(x, y)$:

$$\left[\frac{\nabla^2_\perp}{k^2} + n^2(x, y)\right]E_x$$

$$+ \frac{1}{k^2}\frac{\partial}{\partial x}\left(E_x\frac{\partial \ln(n^2)}{\partial x} + E_y\frac{\partial \ln(n^2)}{\partial y}\right) = \frac{\beta^2}{k^2}E_x, \tag{1}$$

$$\left[\frac{\nabla^2_\perp}{k^2} + n^2(x, y)\right]E_y$$

$$+ \frac{1}{k^2}\frac{\partial}{\partial y}\left(E_x\frac{\partial \ln(n^2)}{\partial x} + E_y\frac{\partial \ln(n^2)}{\partial y}\right) = \frac{\beta^2}{k^2}E_y, \tag{2}$$

where β is the propagation constant, k is the wave number, $\nabla_\perp$ is the gradient operator in the (x, y) plane, and $n(x, y)$ is the profile of the refractive index.

The transverse distribution of the electric field in the PCF cross section is represented as a series expansion in a set of orthonormalized Hermite–Gauss polynomials:

$$E_x = \sum_{n, m = 0}^{F - 1} \xi^x_{n, m}\psi_n\left(\frac{x}{\Lambda}\right)\psi_m\left(\frac{y}{\Lambda}\right),$$

$$E_y = \sum_{n, m = 0}^{F - 1} \xi^y_{n, m}\psi_n\left(\frac{x}{\Lambda}\right)\psi_m\left(\frac{y}{\Lambda}\right). \tag{3}$$

The profile of the refractive index is expanded in Hermite–Gauss polynomials and a set of orthogonal periodic functions:

$$n^2(x, y) = \sum_{n, m = 0}^{N_d - 1}\left(D_{n, m}\psi_n\left(\frac{x}{w}\right)\psi_m\left(\frac{y}{w}\right)\right)$$

$$+ \sum_{k, l}^{N_p - 1} P_{k, l}\cos\left(\frac{2\pi kx}{T_x}\right)\cos\left(\frac{2\pi ly}{T_y}\right), \tag{4}$$

where N_d and N_p are the dimensions of the basis of expansion functions; $D_{n, m}$ and $P_{k, l}$ are constant coefficients; T_x and T_y are the periods of the structure of the PCF cladding along the x and y axes, respectively; and Λ and w are the spatial scales of the PCF cross section [24]. Dispersion and mode properties of hollow PCFs were simulated with field and refractive-index expansions in 80×80 Hermite–Gauss polynomials and 150×150 trigonometric functions.

Substitution of series expansions (3) and (4) into wave equations (1) and (2) reduces the initial problem to an eigenfunction and eigenvalue problem of a matrix equation, which allows the propagation constants and transverse field profiles to be determined for the air-guided modes of hollow PCFs. Figure 1 displays the mismatch $\delta\beta = \beta_{3\omega} - \beta'_{2\omega} - \beta''_{2\omega} + \beta_\omega$ of the propagation constants β_ω, $\beta'_{2\omega}$, $\beta''_{2\omega}$, and $\beta_{3\omega}$ of air-guided modes in the PCF involved in the FWM process $3\omega = 2\omega + 2\omega - \omega$ (2ω and ω are the frequencies of the pump field). The results presented in this plot indicate a nearly perfect phase matching for the FWM of the fundamental mode of fundamental radiation ω of a Cr:forsterite laser, the fundamental mode of one of the second-harmonic fields 2ω, a higher order guided mode of the other second-harmonic field 2ω, and a higher guided mode of the
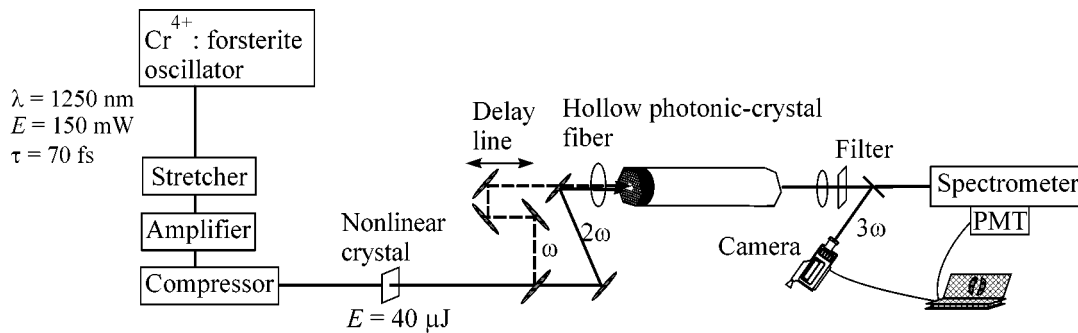
Fig. 2. Diagram of the femtosecond laser system for the investigation of nonlinear-optical interactions of high-intensity ultrashort laser pulses in a hollow photonic-crystal fiber.

nonlinear signal (see inset *2* in Fig. 1). The phase matching, as can be seen from Fig. 1, is achieved within a spectral range with a width of about 10 nm, allowing the highly efficient FWM of broadband, femtosecond laser pulses. The results of our experiments, presented below in this paper, are fully consistent with this theoretical analysis.

The laser system employed in our experiments (Fig. 2) consisted of a Cr^{4+}:forsterite master oscillator, a stretcher, an optical isolator, a regenerative amplifier, a compressor, and a crystal for frequency doubling. The master oscillator, pumped with a fiber ytterbium laser, generated 30–50 fs light pulses with a repetition rate of 120 MHz, a central wavelength of 1250 nm, and a mean power of about 180 mW. These pulses were then transmitted through a stretcher and an isolator to be amplified in a Nd:YLF-laser-pumped amplifier. Amplified pulses with an energy up to 100 μJ were recompressed to a 50–100 fs pulse duration in a grating compressor. Approximately 50% of the radiation energy was lost at this stage. An LBO crystal was used to generate the second harmonic of amplified Cr:forsterite-laser radiation.

Femtosecond pulses of 1.25-μm fundamental radiation and 625-nm second-harmonic radiation of the Cr: forsterite laser with pulse energies ranging from 0.1 up to 10 μJ were used as pump fields ω and 2ω in the FWM process 3ω = 2ω + 2ω − ω. These pulses were coupled into a 5-cm hollow PCF with the period of the cladding equal to 4.6 μm and a core diameter of about 13 μm, placed on a three-dimensional translation stage, with a standard microobjective. Fundamental radiation was focused in such a way as to provide the maximum efficiency of beam coupling into the fundamental mode of the PCF (inset *1* in Fig. 3). The second harmonic was coupled into a mixture of the fundamental and higher-order air-guided modes (inset *2* in Fig. 3). The FWM of these two pump fields induced by the third-order nonlinearity of the atmospheric-pressure air filling the PCF resulted in the generation of a signal with a central wavelength of 417 nm (Fig. 3). The maximum efficiency of FWM frequency conversion achieved in our experiments is estimated as 0.2%. Because of a poor phase matching, direct third-harmonic generation 3ω =

ω + ω + ω, giving rise to a nonlinear signal with the same central wavelength, was several orders of magnitude less efficient in our experiments than the two-color FWM 3ω = 2ω + 2ω − ω.

Analysis of the transverse intensity profile of the FWM signal at the output of the hollow PCF shows that the nonlinear signal is generated in a stable isolated well-resolved higher-order air-guided mode of the PCF (inset *3* in Fig. 3). This finding agrees well with our theoretical analysis of phase matching for the considered FWM process in the hollow PCF (cf. inset *2* in Fig. 1 and insets *1–3* in Fig. 3). We can argue, therefore, that the spatial beam profile of the FWM signal generated in a PCF as a result of nonlinear-optical interaction of isolated air-guided modes of pump radiation is dictated and stabilized by phase-matching conditions. This remarkable property of FWM in a hollow PCF provides
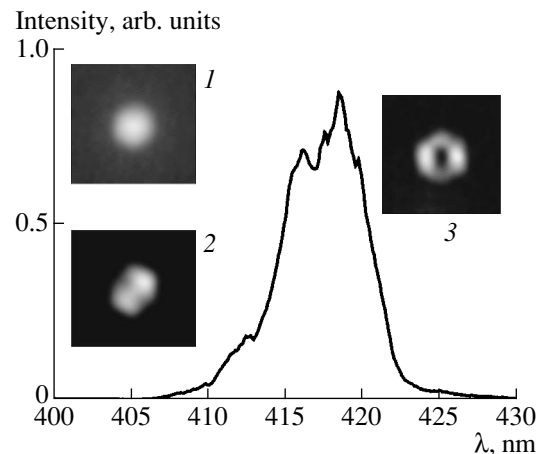

Fig. 3. The spectrum of the FWM signal generated in the hollow photonic-crystal fiber by the pulses of fundamental radiation and the second harmonic of the Cr:forsterite laser with input energies of 2 and 3 μJ, respectively. The initial duration of the pump pulses of fundamental radiation is about 50 fs. The insets show the spatial beam profiles measured for the fundamental (*1*) and second-harmonic (*2*) pump beams and the FWM signal (*3*) at the output of the PCF.

a high beam quality of the nonlinear signal at the output of the fiber and suggests an exciting opportunity of mode-controlled nonlinear-optical processing of high-intensity laser pulses.

The spatial beam profile of the FWM signal at the output of the PCF remained stable up to an energy of input pump pulses of about 6 μJ, corresponding to a light-field intensity of about 9×10^{13} W/cm^2. Spatial self-action and ionization effects started to play a noticeable role above this level of input laser intensities, leading to instabilities and distortions in output beam profiles of the pump and FWM fields. Laser pulses with energies exceeding 10 μJ produced optical damage on PCF inner walls in our experiments, resulting in an irreversible degradation of fiber transmission and a substantial lowering of the FWM efficiency.

The results of experimental and theoretical studies presented in this paper show that hollow-core photonic-crystal fibers with a special dispersion profile allow phase-matched nonlinear-optical interactions of isolated air-guided modes of high-intensity femtosecond laser pulses confined in the hollow fiber core. Phase matching of isolated air-guided modes of high-intensity femtosecond laser pulses involved in nonlinear-optical interactions in a hollow PCF provides a high efficiency of frequency conversion for ultrashort laser pulses with an intensity on the order of 10^{14} W/cm^2 and stabilizes the spatial intensity profile of the output FWM signal.

REFERENCES

1. Ch. Spielmann, N. H. Burnett, S. Sartania, *et al.*, Science **278**, 661 (1997).

2. Z. H. Chang, A. Rundquist, H. W. Wang, *et al.*, Phys. Rev. Lett. **79**, 2967 (1997).

3. P. M. Paul, E. S. Toma, P. Breger, *et al.*, Science **292**, 1689 (2001).

4. M. Drescher, M. Hentschel, R. Kienberger, *et al.*, Science **291**, 1923 (2001).

5. M. Hentschel, R. Kienberger, Ch. Spielmann, *et al.*, Nature **414**, 509 (2001).

6. E. A. J. Marcatili and R. A. Schmeltzer, Bell Syst. Tech. J. **43**, 1783 (1964).

7. A. M. Zheltikov, Usp. Fiz. Nauk **172**, 743 (2002) [Phys. Usp. **45**, 687 (2002)].

8. M. Nisoli, S. De Silvestri, O. Svelto, *et al.*, Opt. Lett. **22**, 522 (1997).

9. N. Zhavoronkov and G. Korn, Phys. Rev. Lett. **88**, 203901 (2002).

10. A. Rundquist, C. G. Durfee III, Z. Chang, *et al.*, Science **280**, 1412 (1998).

11. E. Constant, D. Garzella, P. Breger, *et al.*, Phys. Rev. Lett. **82**, 1668 (1999).

12. A. Paul, R. A. Bartels, R. Tobey, *et al.*, Nature **421**, 51 (2003).

13. R. B. Miles, G. Laufer, and G. C. Bjorklund, Appl. Phys. Lett. **30**, 417 (1977).

14. A. B. Fedotov, F. Giammanco, A. N. Naumov, *et al.*, Appl. Phys. B **72**, 575 (2001).

15. A. N. Naumov, F. Giammanco, D. A. Sidorov-Biryukov, *et al.*, Pis'ma Zh. Éksp. Teor. Fiz. **73**, 301 (2001) [JETP Lett. **73**, 263 (2001)].

16. R. F. Cregan, B. J. Mangan, J. C. Knight, *et al.*, Science **285**, 1537 (1999).

17. P. St. J. Russell, Science **299**, 358 (2003).

18. S. O. Konorov, A. B. Fedotov, O. A. Kolevatova, *et al.*, Pis'ma Zh. Éksp. Teor. Fiz. **76**, 401 (2002) [JETP Lett. **76**, 341 (2002)].

19. F. Benabid, J. C. Knight, G. Antonopoulos, and P. St. J. Russell, Science **298**, 399 (2002).

20. S. O. Konorov, A. B. Fedotov, and A. M. Zheltikov, Opt. Lett. **28**, 1448 (2003).

21. S. O. Konorov, D. A. Sidorov-Biryukov, I. Bugar, *et al.*, Appl. Phys. B **78** (2004) (in press); DOI: 10.1007/s00340-004-1417-6.

22. D. G. Ouzounov, F. R. Ahmad, D. Müller, *et al.*, Science **301**, 1702 (2003).

23. S. O. Konorov, A. B. Fedotov, O. A. Kolevatova, *et al.*, J. Phys. D: Appl. Phys. **36**, 1375 (2003).

24. E. E. Serebryannikov and A. M. Zheltikov, Laser Phys. **13**, 1339 (2003).

Translated by A. Zheltikov

Measurements of X-Ray Absorption Spectra by the Prism Spectroscopy Method

A. G. Tur'yanskii*, I. V. Pirshin, and D. V. Belyanskii

Lebedev Physical Institute, Russian Academy of Sciences, Leninskiĭ pr. 53, Moscow, 119991 Russia
*e-mail: tour@mail1.lebedev.ru
Received April 1, 2004

X-ray absorption spectra of a number of samples were measured in the range 5–30 keV by the prism spectro-photometry method. The spectral decomposition was performed using an optically polished diamond prism with an opening angle of 90°. The absorption spectra of liquid bromonaphthalene are presented as an example. An energy resolution of 100–130 eV was achieved in the energy range of ~10 keV, providing the unambiguous identification of elements by jumps in the K photoabsorption. © *2004 MAIK "Nauka/Interperiodica"*.

PACS numbers: 07.85.Nc; 41.50.+h

The possibility of the spectral decomposition of X radiation using a diamond prism has been substantiated in recent works [1–3] and experimentally tested through recording intense X-ray tube emission spectra. It is evident, however, that only the possibility of determining the sample composition from the absorption spectra is a criterion for the practical importance of the suggested method.

In this work, an improved spectrometer scheme is described that provides a manyfold increase in the sensitivity and accuracy. It was used to record the X-ray absorption spectra of a number of samples by the prism spectroscopy method.

It is known that the width of the K-absorption jump is $\Delta E_K \sim \Gamma_K$ [4], where Γ_K is the width of an atomic level in the K shell ($1s$ state). According to [5], Γ_K varies within 0.5–50 eV for the majority of chemical elements. The energy shift ΔE_C caused by the chemical bonding of atoms ordinarily does not exceed 1–4 eV [6, 7]. At the same time, the difference $\Delta E_B = E_K(Z + 1) - E_K(Z)$ in the K-electron binding energies of atoms of the neighboring elements in the periodic table is equal to 0.5–2.5 keV for $Z > 20$. That is, $\Delta E_B \gg \Delta E_K$ and $\Delta E_B \gg \Delta E_C$. Thus, measurements of the positions of K-absorption jumps with a resolution no worse than $\Delta E_B/2$ allow the practically unambiguous identification of elements entering the sample composition. With minor reservations, this statement can be extended to the L-absorption jumps for the elements with $Z > 50$.

The X-ray optical scheme of a prism spectrometer in the measurement plane is shown in Fig. 1. Sharp-focus X-ray tube *1* with a copper anode serves as a radiation source. The sizes of the focus projection onto the plane normal to the analyzed beam are 40 μm in the measurement plane and 8 mm in the perpendicular direction. Two X-ray goniometers *5* and *11* are placed in the beam path. A diamond prism with the opening angle $\alpha = 90°$ between the refracting faces is placed at the axis of the first goniometer. The prism is made from a single crystal of natural diamond. The angle of incidence φ of a primary beam on the prism entrance face was chosen to be ~1 mrad. With these values of α and φ, the radiation passes through the entrance face almost without deflection, so that the beam glancing angle relative to the exit face is $\theta = \varphi$. The advantages of this spectrometric geometry were substantiated in our work [3]. The area of the refracting face is 12 mm^2. The first goniometer is designed for the prism angular tuning against the specular reflection from the refracting face. The tuning is accomplished using detector *10*, ahead of which a monochromator *8* is placed to set off the CuK_α line (0.154 nm). The second goniometer serves for the angular displacement of main detector *13* containing a 1-mm-thick NaI(Tl) crystal and a photomultiplier. This provides a ≥90% efficiency of quantum detection in the energy range $E < 30$ keV.
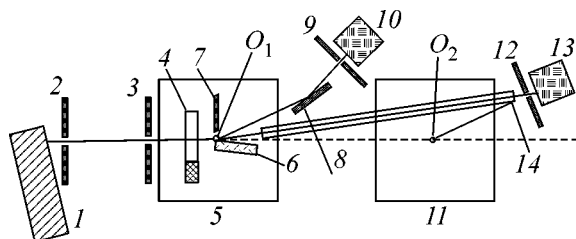

Fig. 1. Scheme of a prism spectrometer: (*1*) X-ray tube; (*2, 3*) collimator slits; (*4*) sample; (*5, 11*) goniometers; (*6*) diamond prism; (*7*) absorbing screen; (*8*) monochromator; (*9, 12*) receiving slits; (*10, 13*) radiation detectors; (*14*) pumped-out collimator.
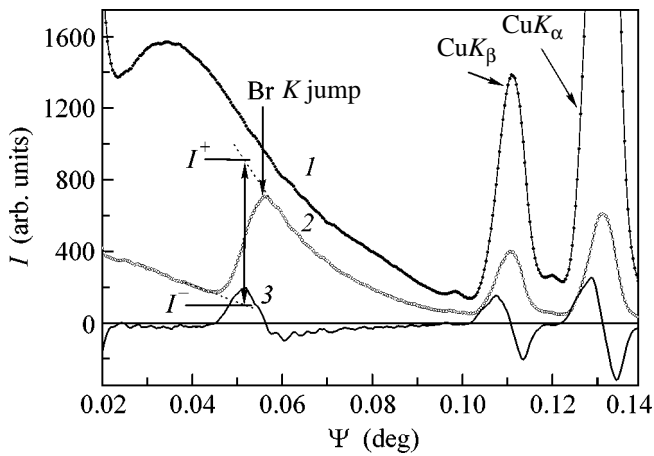
Fig. 2. Angular dependences $I(\Psi)$ of the intensity of refracted radiation: (*1*) before the introduction of a bromonaphthalene ($C_{10}H_7Br$) sample; (*2*) after the introduction; (*3*) $dI/d\Psi$ derivative of curve *2*.

The distances from the X-ray-tube focus to the principal axes O_1 and O_2 of goniometers *5* and *11* are equal to 330 and 1161 mm, respectively, and from the axes O_1 and O_2 to detector slits *9* and *12* are equal to 225 and 192 mm, respectively. Since the spectrum is decomposed on the O_1 axis, while the detector is rotated about the O_2 axis, the scheme provides a factor-of-$(L + R)/R = 5.3$ increase in the angular resolution for the indicated recording scheme. A sample *4* under study was placed between the collimator exit slit and the diamond prism. To minimize losses caused by the attenuation and scattering of X radiation in air, a vacuum collimator (*14*) 960 mm long with windows made from a 0.2-mm-thick Be foil was placed between the O_1 axis and receiving detector *13*. The collimator provided a more than one order of magnitude increase in the intensity of the detected signal in the energy range $E < 6$ kV. Measurements were made with a voltage of 35 kV on the X-ray tube. The angular step and the exposure time at the angular points were 0.0002° and 1.8 s, respectively.

The angular dependences $I(\Psi)$ of the intensity of refracted radiation on the deflection angle before and after the introduction of a bromonaphthalene sample ($C_{10}H_7Br$) are shown in Fig. 2 (curves *1* and *2*, respectively). The deflection angle Ψ is measured counterclockwise from the axis of the primary beam. Curves *1* and *2* were obtained for the glancing angle $\theta = 0.218°$ between the primary beam and the prism refracting face.

The intense lines in the spectra correspond to the copper anode characteristic emission CuK_α (8.05 keV) and CuK_β (8.90 keV). A well-defined absorption feature appears in the angular spectrum upon the passage of radiation through the bromonaphthalene sample. To

simplify its location, it is convenient to use the derivative of the angular spectrum $I(\Psi)$ (curve *3*).

By using the expression for the refractivity decrement [4] and the small-angle approximation for Snell's law, we obtain the relationship

$$E_K = E_0 \sqrt{\frac{2\delta_0}{(\Psi_K^2 + 2\theta\Psi_K)}}, \qquad (1)$$

where Ψ_K is the experimentally measured angular position of the K jump in the $I(\Psi)$ curve and E_0 and δ_0 are the energy and refractivity decrement, respectively, of the reference line. The energies of the characteristic CuK_α and CuK_β lines emitted by the tube copper anode can be taken as reference points. Let us consider a multicomponent sample containing m chemical elements. The expression for the relative change in the signal intensity before and after absorption at energies higher (E^+) and lower (E^-) than the given absorption jump edge can be written in the form of the products of exponentials

$$\frac{I(E_{K^-})}{I_0(E_{K^-})} = \exp[-\mu(E_{K^-})\rho L]\exp\left[-\sum_{j=1}^{m-1}\mu_j(E_{K^-})\rho_j L\right], \qquad (2)$$

$$\frac{I(E_{K^+})}{I_0(E_{K^+})} = \exp[-\mu(E_{K^+})\rho L]\exp\left[-\sum_{j=1}^{m-1}\mu_j(E_{K^+})\rho_j L\right], \qquad (3)$$

where $I_0(E_{K^+})$, $I_0(E_{K^-})$ and $I(E_{K^+})$, $I(E_{K^-})$ are the intensities in the spectra of the direct and absorbed beams at energies E_{K^+} and E_{K^-} measured before and after the introduction of the sample, respectively; μ and ρ are the mass attenuation coefficient and the partial density, respectively, of the element whose energy at the absorption jump edge is equal to E_K; μ_j and ρ_j are the partial mass attenuation coefficients and densities of other elements in the sample; and L is the sample size along the direct beam. It is known that, far from the absorption jump, $\mu(E)$ is a smooth and monotonically decreasing function. For this reason, the ratio of the exponential factors containing the summation sign tends to unity at $E_{K^+} \longrightarrow E_K$ and $E_{K^-} \longrightarrow E_K$. The function $\mu(E)$ changes jumpwise in the E_K region. Then, taking the logarithm of Eqs. (2) and (3) and dividing their left- and right-hand sides, one gets

$$\ln\left[\frac{I(E_{k^-})}{I(E_{k^+})}\right] \approx [\mu(E_{K^-}) - \mu(E_{K^+})]\rho L. \qquad (4)$$

If the length L is known, the partial density or the weight content of the element of interest can be determined from Eq. (4); for the known cross-sectional area of the direct beam, the partial mass of the element in the irradiated volume can be found.
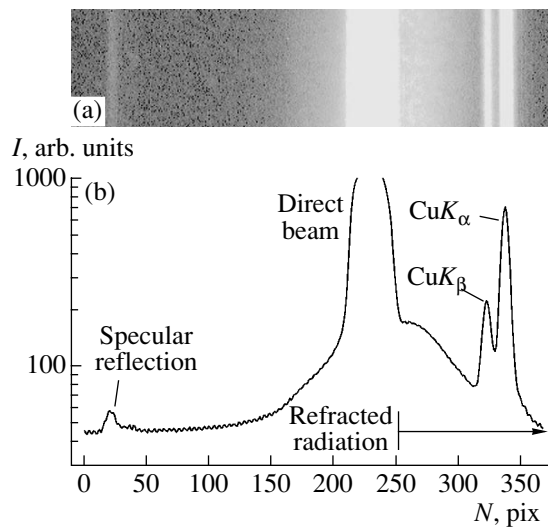
Fig. 3. (a) Two-dimensional image of the refracted X-ray beam pattern. (b) Dependence of the signal intensity on the pixel number for the image in Fig. 3a: (left) peak of specular reflection from the refracting face ($N = 23$); (center) direct beam ($N = 210–250$); and (right) bremsstrahlung spectrum ($N > 250$) and the CuK_β ($N = 320$) and CuK_α ($N = 335$) lines.

This is an important advantage of the suggested method over the emission X-ray fluorescence analysis, which when used requires the introduction of complicated corrections.

In conclusion, we present a two-dimensional image of the refraction pattern obtained for the direct beam at a distance of 255 mm from the diamond prism (Fig. 3a). An FDI X-ray camera (Photonic Science) with a two-dimensional array containing 1300×1030 pixels was used as a radiation receiver. A Gd oxysulfide layer served as a scintillator. The pixel size was 6.7 μm, and the exposure time was 1 s. Since the photons with dif-ferent energies are spatially separated after passing through the prism, the spectrum measurement time is of no importance. The radiation flux P through the spectrometer entrance aperture is the only important parameter, because it provides the acceptable signal-to-noise ratio for the image. The dependence of the signal intensity on the pixel number in the central row of the detecting array is shown in Fig. 3b. The integrated refracted-radiation flux P_0 detected at the right side of the image in Fig. 3a was equal to ~10^6 quantum/s. This signifies that, at $P \geq P_0$, the X-ray pulse spectra can be detected by a prism spectrometer without any restrictions on the pulse duration.

REFERENCES

1. A. G. Tur'yanskiĭ, I. V. Pirshin, and R. A. Khmel'nitskiĭ, Kratk. Soobshch. Fiz. **4**, 40 (2000).

2. A. G. Tur'yanskiĭ, I. V. Pirshin, R. A. Khmel'nitskiĭ, *et al.*, Fiz. Tverd. Tela (St. Petersburg) **43**, 619 (2001) [Phys. Solid State **43**, 644 (2001)].

3. A. G. Tur'yanskiĭ, I. V. Pirshin, R. A. Khmel'nitskiĭ, *et al.*, Pis'ma Zh. Éksp. Teor. Fiz. **73**, 517 (2001) [JETP Lett. **73**, 457 (2001)].

4. M. A. Blokhin, *Physics of X-rays* (GITTL, Moscow, 1957).

5. M. A. Blokhin and I. G. Shveĭtser, *X-ray Spectral Handbook* (Nauka, Moscow, 1982).

6. M. Freemantle, *Chemistry in Action* (Macmillan, London, 1987).

7. É. E. Vaĭnshteĭn, *X-ray Spectra of Atoms in Molecules of Chemical Compounds and Alloys* (Akad. Nauk SSSR, Moscow, 1950).

Translated by V. Sakun

Current-Induced Domain Formation in Magnetic Junctions

Yu. V. Gulyaev[1], P. E. Zilberman[1, *], É. M. Épshteĭn[1], and R. J. Elliott[2]

[1] *Institute of Radio Engineering and Electronics, Russian Academy of Sciences (Fryazino Branch),*
pl. Vvedenskogo 1, Fryazino, Moscow region, 141190 Russia
*e-mail: zil@ms.ire.rssi.ru
[2] *University of Oxford, Department of Physics, Theoretical Physics, Oxford OX1, UK*
Received March 12, 2004

A junction between two ferromagnetic metal layers with fixed spins in one of them and free spins in the other (spin valve) is considered. The junction is placed in an external magnetic field that orients the free layer oppositely to the fixed layer. It is shown that the spin-polarized electron flow from the fixed layer to the free layer gives rise to stable motionless magnetic domains in the free layer, provided that the magnetic field and the thickness of the free layer are large enough. © *2004 MAIK "Nauka/Interperiodica"*.

PACS numbers: 75.70.Cn; 75.70.Kw

In recent years, considerable interest has been shown in so-called magnetic junctions, i.e., layered structures composed of at least two ferromagnetic conducting layers (with fixed spins in one of them and free spins in the other) separated by an ultrathin nonmagnetic film. The junctions of this type exhibit interesting phenomena associated with the transport of spin-polarized electrons. It has been shown in recent works [1–3] that current exerts a certain effect on the magnetic state of the free layer. This effect consists in the switching of the relative magnetization orientation of the free layer. The nature of this switching is as yet little understood. Nevertheless, it is clear that the switching is induced not merely by the current magnetic field but rather by the *s–d*-exchange interaction of spin-polarized charge carriers. One of the possible reasons for switching is that current injects spins into the free ferromagnetic layer. Due to the *s–d* exchange, these spins interact with the lattice magnetization vector and change its orientation. It was shown in [4] that the original magnetization orientation becomes unstable at a rather high current density and changes jumpwise. A detailed theory of this phenomenon is given in [5]. Estimates of the switching threshold made in [4, 5] are in good agreement with the experimental estimates [1–3].

In this communication, we would like to draw attention to one more important feature of the switching effect that was described in [4, 5]. In those works, the free layer was switched uniformly, i.e., as a whole. Such a switching corresponds to the experimental conditions used in [1–3]. However, the uniform switching becomes impossible upon a certain change in the experimental conditions, so that the switching becomes nonuniform. Let the external magnetic field **H** in the absence of current magnetize the free layer oppositely to the fixed layer. Let us now switch on current in the direction such that electrons pass from the fixed to the

free layer. The density of nonequilibrium (current-injected) spins decreases with distance from the interface on the scale of free-layer spin-diffusion length *l*. In the case of the free-layer thickness $L \gg l$ and a high absolute value of field *H*, the uniform switching would be accompanied by a considerable loss in Zeeman energy. For this reason, the free layer is switched only in the region of thickness $\sim l$ that is adjacent to the fixed layer (injector), thereby minimizing the *s–d*-exchange energy. The rest of the free layer remains unswitched. As a result, magnetic domains arise in the free layer. The boundary between these domains occupies a certain stable equilibrium position determined by the current density **j** and the field **H**. For the typical parameters of metal layers, the domain boundary can execute small oscillations about its equilibrium position with a frequency lying in the range from several to tens of gigahertz. In what follows, the conditions for the formation of such domains are obtained in the form of a relationship between *L* and *H*.

1. Model and calculations. To simplify the calculation, we will use the model of magnetic junction shown in Fig. 1. All layers in this figure have infinite sizes in their developed planes perpendicular to the *x* axis. Spins in ferromagnetic layer *1* are fixed. This means not only that the magnetization vector $\mathbf{M}_1$ of the layer is fixed and can be disturbed neither by field nor by current but also that the spins of moving electrons are fixed, i.e., that they belong only to one of the spin subbands. Such a situation is ideally realized in so-called half-metals [6]. It is also relevant to the Co films, which are the only ones that are as yet used in experiments on current-induced switching.

Spins in ferromagnetic layer *2* are free. It is assumed that this layer is divided into domains with oppositely oriented magnetization vectors $(-\mathbf{M}_2)$ and $\mathbf{M}_2$ and that

$(-\mathbf{M}_2) \parallel \mathbf{M}_1$ and $\mathbf{M}_2 \parallel \mathbf{H}$. The technological interfaces between the layers coincide with the planes $x = 0$ and L, and the domain boundary coincides with the plane $x = W$. These boundaries are assumed to be thinner than the spin-diffusion length l. At room temperature, it is estimated as $l \sim 10$–100 nm. Such thin technological boundaries can be obtained in practice in structures with spin-dependent transport and spin injection. As to the thickness of domain wall, it is determined, in principle, by the processes in layer 2; this item will be discussed somewhat later in this work. Layer 3 is a nonmagnetic conductor that is necessary for closing the circuit in the system.

The calculation is based on a system of coupled continuity equations for the concentrations n_+ and n_- of spin-up and spin-down charge carriers, respectively, in layer 2. The partial current densities in these equations are

$$j_\pm = e\mu_\pm n_\pm(x)E(x) - eD_\pm \frac{dn_\pm(x)}{dx}, \qquad (1)$$

where $E(x)$ is the local electric field; $\mu_\pm$ and $D_\pm$ are the partial mobilities and diffusion coefficients, respectively; and e is the carrier charge. The total current density

$$j = j_+ + j_- = e[\mu_+ n_+(x) + \mu_- n_-(x)]E(x)$$
$$- e\left[D_+ \frac{dn_+(x)}{dx} + D_- \frac{dn_-(x)}{dx}\right] \qquad (2)$$

is independent of the coordinate x under the stationary conditions considered in this work. Moreover, due to the neutrality condition that holds for metals, the total concentration $n = n_+(x) + n_-(x)$ is also independent of x. Using Eq. (2), the field $E(x)$ can be eliminated from formulas (1) for partial currents and from the continuity equations. It should also be taken into account that, due to the neutrality conditions, only one of the two functions $n_\pm(x)$ in the continuity equations is independent. It is convenient to take the degree of polarization $P(x) \equiv (n_+(x) - n_-(x))/n$ as the only unknown function.

In what follows, we are interested only in small deviations of $P(x)$ from its equilibrium value $\bar{P}$, i.e., in "low" injection levels. By introducing the deviation $\Delta P(x) \equiv P(x) - \bar{P}$ and taking into account that $|\Delta P| \ll \bar{P}$, we arrive at the following main equation:

$$\frac{d^2(\Delta P)}{dx^2} - \frac{\tilde{v}}{\tilde{D}}\frac{d(\Delta P)}{dx} - \frac{\Delta P}{l^2} = 0, \qquad (3)$$

where

$$\tilde{D} = \frac{D_+ \mu_- \bar{n}_- + D_- \mu_+ \bar{n}_+}{\mu_+ \bar{n}_+ + \mu_- \bar{n}_-},$$

$$\tilde{v} = \frac{j}{en}\frac{e^2 n^2 \mu_+ \mu_-}{\sigma^2}, \quad l = \sqrt{\tilde{D}\tau} \qquad (4)$$
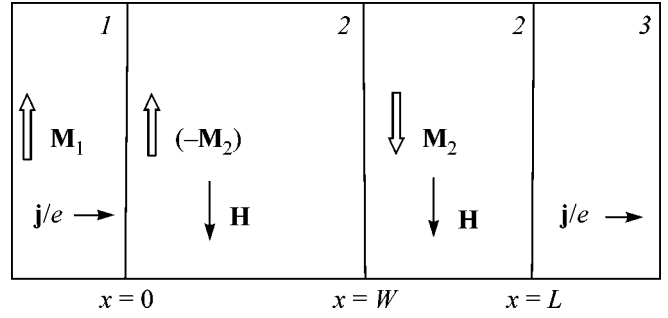
Fig. 1. Model of magnetic junction: 1, 2, 3 are the layer numbers in the junction; $x = 0$, L are the technological interfaces between the layers; and $x = W$ is the domain wall. Arrow indicates the sense of vector. Electron flow $\mathbf{j}/e$ is directed along the x axis.

are the diffusion coefficient, the drift velocity, and the spin-diffusion length, respectively; $\sigma = (\sigma_+ + \sigma_-)$ is the equilibrium conductivity; $\sigma_\pm = e\bar{n}_\pm \mu_\pm$; and τ is the spin-relaxation time.

Let us compare, by the order of magnitude, the two last terms in Eq. (3). The weak-current condition

$$j \ll j_D \equiv \frac{enl}{\tau} \geq 10^{10} \text{ A/cm}^2 \qquad (5)$$

is well fulfilled in the considered structures with metal layers. Due to this condition, the first-derivative term accounting for the spin drift in Eq. (3) can be dropped. Note, however, that this does not imply that the charge-carrier drift is fully ignored. Indeed, the diffusion length l, according to Eq. (4), depends on the mobilities $\mu_\pm$, i.e., on the drift. The carriers in the two subbands move in a common field that renders their motion correlated to ensure neutrality. This situation is analogous to ambipolar diffusion in semiconductors [7].

The desired solutions to Eq. (3) must satisfy the boundary conditions at the points $x = 0$, W, and L of layer 2. Following, e.g., works [8, 5], we take one such boundary condition in the form of a requirement that the spin flux be continuous at each of the indicated points,

$$J_s(x) \equiv (\hbar/2e)\left(Qj - en\tilde{D}\frac{d\Delta P}{dx}\right), \qquad (6)$$

where $Q = (\sigma_+ - \sigma_-)/\sigma$. As the second boundary condition at the points $x = W$ and L, we require that the difference in the chemical potentials of spin subbands be continuous,

$$\zeta_+ - \zeta_- = N\Delta P, \qquad (7)$$

where $N = (n/2)[g_+^{-1}(\bar{\zeta}) + g_-^{-1}(\bar{\zeta})]$; $g_\pm(\bar{\zeta})$ are the carrier densities of state in each of the subbands; and $\bar{\zeta}$ is the equilibrium chemical potential, identical for all subbands and layers.

The solutions to linear Eq. (3) with boundary conditions (6) and (7) can be found by the standard method. The resulting formulas for the injected-spin distribution $\Delta P(x)$ are rather cumbersome, and we do not present them here. We only note that, at a large distance from the injector, namely, at $x > l$, the function $\Delta P(x)$ tends to zero, following a law close to exponential. This function will be used below to calculate the s–d-exchange energy

$$U_{s-d} = -\alpha\mu_B n \int_0^L M_2(x)\Delta P(x)dx, \qquad (8)$$

where $\alpha \sim Aa^3/\mu_B^2$ is the dimensionless exchange-interaction parameter; A is the exchange energy (typically, $A \sim 0.1$–10 eV); the parameter a is on the order of the lattice constant, so that one can take $a^3 \sim 10^{-23}$ cm^{-3} for estimates; and μ_B is the Bohr magneton. This gives $\alpha \sim 1.8(10^4$–$10^6) \gg 1$.

Apart from contribution (8), the total magnetic energy U_{tot} includes the Zeeman energy U_H in the external field H

$$U_H = -\int_0^L \tilde{M}_2(x)H dx, \qquad (9)$$

where $\tilde{M}_2 = M_2 + \mu_B n\bar{P}$ is the magnetization in layer 2 with allowance for the charge-carrier contribution. The anisotropy axis is assumed to be parallel with the field **H** and magnetization **M**$_2$, so that the anisotropy energy can make a contribution only to the domain-boundary energy γ. Therefore, the total energy has the structure $U_{tot} = U_{s-d} + U_H + \gamma$. Then, the direct calculation brings about the following expression for the total energy:

$$U(w, J) = -J\{(Q_1 - Q_2)[1 - 2\exp(-w)]$$
$$- 2Q_2\exp(-2w) + Q_2(1 + \nu)^{-1}\} + h\left(w - \frac{\lambda}{2}\right) + \Gamma, \qquad (10)$$

where we use the dimensionless quantities

$$U = U_{tot}/8\pi M_2^2 l; \quad \Gamma = \gamma/8\pi M_2^2 l;$$
$$h = H/4\pi M_2; \quad J = (\alpha\mu_B n/8\pi M_2)j/j_D; \qquad (11)$$
$$\lambda = L/l; \quad w = W/l; \quad \nu = (j_{D3}/j_D)(N_2/N_3).$$

For all quantities, the lower numerical indices indicate their belonging to layers 1, 2, or 3. Equation (10) is obtained on the assumption that the thickness of layer 2 is large enough so that $\lambda \gg 1$. The parameter ν accounts for the connection to external conductors and, in particular, for the injection efficiency from layer 2 into layer 3. The value of this parameter is immaterial to us. One can set, e.g., $\nu \gg 1$. Then, no distortions of spin equilibrium will occur near the boundary $x = L$ of layer 2.

2. Domains inside the free layer. According to Eq. (10), the energy $U(w, J)$ has a minimum at

$$w = w_0(h/J)$$
$$\equiv \ln\left[\frac{4Q_2}{Q_1 - Q_2}\left(\sqrt{1 + \frac{4Q_2 h}{(Q_1 - Q_2)^2 J}} - 1\right)^{-1}\right]. \qquad (12)$$

It follows from this expression that, if the conditions

$$2(Q_1 + Q_2) > h/J > 2\exp(-\lambda)(Q_1 - Q_2) \qquad (13)$$

are met, the energy minimum will occur inside layer 2. Let us take the parameters for layer 2 corresponding to the parameters of a Co film [1–3], and let the thickness of this layer be large enough so that $Q_1 = 0.35$, $Q_2 = 0.15$, and $\lambda = 5$ ($L \sim 50$–500 nm). For the typical experimental current densities $J = 1$ ($j \sim 10^7$/cm^2) [1–3], the minimum occurs inside layer 2 at magnetic fields 12 kOe $> H > 28$ Oe, quite attainable in the experiments.

Thus, we have demonstrated that stable motionless domains separated by a domain boundary perpendicular to the current can exist inside layer 2. This possibility has a clear physical meaning. The domain boundary inside layer 2 is subjected to two magnetic fields: the exchange field $H_{s-d} \equiv \delta U_{s-d}/\delta M_2(x) = -\alpha\mu_B n\Delta P(x)$ and the external field H. The exchange field tends to minimize the energy U_{s-d} (8). It exerts pressure on the domain boundary, which can be called "spin wind." This pressure tends to move the domain boundary away from the injector, i.e., in the direction of increasing coordinate x. However, as x increases, the spin wind weakens because of a decrease in $\Delta P(x)$, i.e., decrease in the spin injection. At the same time, the external field is oriented so that it tends to maintain the antiparallel orientation of magnetization and, hence, move the boundary in the opposite direction. These two actions balance each other at the point $w = w_0$ (13).

One can thus draw an important conclusion about the structure of our domain boundary: due to the mutual compensation, the fields H_{s-d} and H have only little effect on this boundary. More precisely, one can ignore the influence of these fields if the compensation condition

$$|H_{s-d}(x) + H| \sim |dH_{s-d}/dx||x - W_0|$$
$$\sim H(\delta/l) \ll H_a, \qquad (14)$$

(H_a is the anisotropy field) is met inside the domain wall of thickness δ. Under condition (14), the thickness δ was estimated for ferromagnetic Ni in [9] to show that $\delta \sim 10$ nm. Since we have, typically, $H_a \sim 10^3$ Oe in our structures, condition (14) can easily be fulfilled. The above estimate suggests that the condition for a "sharp" ($\delta < l$) domain boundary can also be fulfilled in our case.

3. Domain-wall oscillations. If the domain wall shifts from its equilibrium (energy-minimum) position

$w = w_0$, the energy increases, i.e., a restoring force arises, and, hence, the domain wall can execute free oscillations. To estimate the frequency of these oscillations, we use the Döring model [10]. According to this model, the domain-wall motion in a crystal without pinning centers obeys the equation

$$m\frac{d^2w}{dt^2} + \beta\frac{dw}{dt} = -\frac{8\pi\tilde{M}_2^2}{l_2}\frac{dU(w)}{dw}, \qquad (15)$$

where m is the domain-wall mass per unit area and β is the friction coefficient.

By linearizing the right-hand side of Eq. (15) in the vicinity of equilibrium, we arrive at the equation of linear oscillator with eigenfrequency

$$w = \frac{4\tilde{M}_2}{\sqrt{ml_2}} \qquad (16)$$
$$\times \left\{ \pi J \left[\frac{h}{J} - \frac{(Q_1 - Q_2)^2}{4Q_2} \left(\sqrt{1 + \frac{4Q_2h}{(Q_1 - Q_2)^2 J}} - 1 \right) \right] \right\}^{1/2}.$$

For not too strong fields $h \ll J$, Eq. (16) is simplified and reduced to $\omega = \sqrt{8\pi h}$. The dependence on current J is weak. Taking the typical values $M_2 \sim 10^3$ G, $m \sim 10^{-10}$ g/cm^2, and $l_2 \sim 10^{-6}$ cm, one has the estimate $\omega \sim 10^{11}$ s^{-1}; i.e., the frequency lies in the range from several to tens of gigahertz.

The Q factor of ferromagnetic oscillations in the metal films under study can strongly vary, as evidenced by the experimental data for the FMR line widths: $\Delta H \sim 20-1000$ Oe. The oscillation decay time can be estimated as $\tau_m \equiv \beta/m \sim (\gamma\Delta H)^{-1}$. Inserting the value of gyromagnetic ratio $\gamma \sim 3 \times 10^6$ Hz/Oe into this expression, one finds $\tau_m \sim (2 \times 10^{-7}-3 \times 10^{-10})$ s. Hence, the Q factor is $\omega\tau_m \sim (2 \times 10^4-3 \times 10) \gg 1$; i.e., the oscillations decay rather slowly.

We note additionally that the estimate $\tau \geq 3 \times 10^{-13}$ s obtained earlier for the room-temperature spin-relaxation time corresponds to the diffusion length $l_2 \geq 10$ nm. The estimate made in this work for the frequency indicates that the condition $\omega\tau \ll 1$ for the applicability of static diffusion Eq. (3) can also be fulfilled.

4. Conditions for domain formation and discussion. Let us now discuss the conditions for spontaneous nucleation of a domain boundary inside layer *2*. It was shown in [4, 5] that the original uniform state of layer *2* with the antiparallel orientation of its magnetization becomes unstable at a sufficiently high current density, namely, at $J > J_{th} \sim (h + h_a)\lambda/2Q_1 \sim 1$, where the dimensionless anisotropy field $h_a = H_a/4\pi M_2 \ll 1$. The development of this instability results in the uniform switching of layer *2*, so that the state with parallel orientation is the only possible state for $\lambda \leq 1$ [4]. However, two final states are possible for an arbitrary λ: (1) a uni-
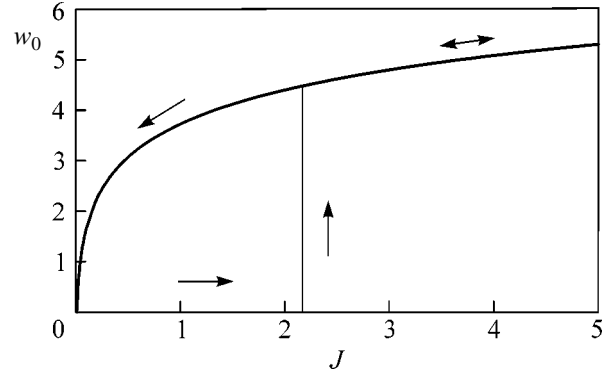

Fig. 2. The thickness w_0 of the switched region inside layer *2* vs. the injected current J for $h = 10^{-2}$, $Q_1 = 0.35$, $Q_2 = 0.15$, and $\lambda = 3$ (in the dimensionless variables).

formly switched state with energy $[U(\lambda, J) - \Gamma]$ and (2) a nonuniformly switched state with energy $U(w_0, J)$. For this reason, the condition for the nonuniform switching with the domain formation inside layer *2* can be written as

$$U(w_0, J_{th}) < [U(\lambda, J_{th}) - \Gamma]. \qquad (17)$$

For the domain-boundary energy $\gamma \sim 10^{-7}$ J/cm^2 [10], the parameters are $h \sim 10^{-2}$, $J \sim 1$, and $\lambda \approx 5$. Then, condition (17) reduces to $\lambda \geq \Gamma/h$. For $l \sim 30$ nm, one finds that domains can form even in fields $H \sim 120$ Oe, at current densities $j \sim 10^7$ A/cm^2 (which is quite realistic; see [1–3]), and in layer *2* of thickness satisfying the condition $L \geq 50-100$ nm.

The current dependence of the domain-boundary position or, what is equivalent, of the thickness w_0 of the switched region is shown in Fig. 2. The domain boundary nucleates at the point where the current reaches its threshold value, whereupon it increases with current. However, with decreasing current, the domain boundary does not disappear at the nucleation threshold but persists down to very small currents and eventually reaches the injector. Thus, switching with the domain-boundary formation has a hysteretic character. The very existence of domains in layer *2* is, basically, unrelated to the instability of the uniform antiparallel state of this layer.

The latter conclusion seems to be highly important, because it demonstrates the possibility of initiating static domains by weak currents. In this connection, we would like to draw attention to the experiments on the initiation of traveling domains in ferrite films (see review [11]) and to work [12], where it is proposed that the domain boundary should be initiated through the introduction of structural inhomogeneity into the film. It is conceivable that closely related approaches will allow the initiation of static domains in magnetic junctions.

REFERENCES

1. J. A. Katine, F. J. Albert, R. A. Buhrman, *et al.*, Phys. Rev. Lett. **84**, 3149 (2000).

2. J. Grolier, V. Cros, A. Hamzic, *et al.*, Appl. Phys. Lett. **78**, 3663 (2001).

3. J.-E. Wegrowe, A. Fabian, Ph. Guittiene, *et al.*, Appl. Phys. Lett. **80**, 3775 (2002).

4. Yu. V. Gulyaev, P. E. Zil'berman, É. M. Épshteǐn, and R. J. Elliott, Pis'ma Zh. Éksp. Teor. Fiz. **76**, 189 (2002) [JETP Lett. **76**, 155 (2002)].

5. R. J. Elliott, E. M. Epshtein, Yu. V. Gulyaev, and P. E. Zilberman, J. Magn. Magn. Mater. **271**, 88 (2004).

6. R. A. de Groot, F. M. Mueller, P. G. van Engen, and K. H. J. Buschow, Phys. Rev. Lett. **50**, 2024 (1983).

7. V. L. Bonch-Bruevich and S. G. Kalashnikov, *Physics of Semiconductors* (Nauka, Moscow, 1977).

8. T. Valet and A. Fert, Phys. Rev. B **48**, 7099 (1993).

9. L. D. Landau and E. M. Lifshitz, Phys. Z. Sowjetunion **8**, 153 (1935); L. D. Landau, in *Collection of Scientific Works* (Nauka, Moscow, 1969), Vol. 1, p. 128.

10. S. Chikasumi, *The Physics of Ferromagnetism. Magnetic Characteristics and Engineering Applications* (Syokabo, Tokyo, 1984; Mir, Moscow, 1987).

11. V. G. Bar'yakhtar, B. A. Ivanov, and M. V. Chetkin, Usp. Fiz. Nauk **146**, 417 (1985) [Sov. Phys. Usp. **28**, 563 (1985)].

12. N. Garcia, V. V. Osipov, and E. V. Ponizovskaya, Phys. Rev. B **64**, 184412 (2001).

Translated by V. Sakun

Dielectric Constant of Polymer Matrices Containing Isolated Inclusions: Giant Dielectric Enhancement instead of Collective Resonance

A. V. Turik[1], *, G. S. Radchenko[1], A. I. Chernobabov[2], and S. A. Turik[1]

[1] *Rostov State University, ul. Zorge 5, Rostov-on-Don, 344090 Russia*
[2] *Pyatigorsk State Technological University, Pyatigorsk, 357500 Russia*
*e-mail: turik@phys.rsu.ru
Received December 5, 2003; in final form, February 24, 2004

A giant increase in the static dielectric constant and a giant dielectric relaxation are predicted for a heterogeneous medium consisting of matrix-isolated spheroids and described by the Maxwell-Garnett formula. The possibility of observing collective dielectric resonance in such a medium is also discussed. © *2004 MAIK "Nauka/Interperiodica".*

PACS numbers: 78.20.Ci; 77.22.Gm

1. Dielectric constant of 0–3 composites. Composites with the connectivity of 0–3 type (according to the classification [1]) in the form of a polymer matrix containing isolated inclusions with volume concentration η and dielectric constant (DC) ε_{inc} far exceeding the matrix DC ε_m (e.g., inclusions of ferroelectric ceramics) are widely used in modern technology. Nevertheless, some problems associated with both the theoretical description and practical use of such composites still remain to be understood. The possibility of obtaining and using very high (giant) DCs ε is among such problems. One such possibility associated with dispersing inclusions with a high DC in a conducting matrix is considered in this work.

2. Maxwell-Garnett formula. The use of the Maxwell-Garnett (MG) formula [2, 3] for a matrix containing spheroidal inclusions with the aspect ratio $\xi = c/a$ ($a = b \neq c$ are the spheroid semiaxes) strongly different from unity is at the basis of our theoretical approach. The MG formula is widely used for matrix systems and yields the most reliable results in the limiting cases of very small ($\eta \longrightarrow 0$) and very high ($\eta \longrightarrow 1$) inclusion concentrations. In the case of spheroids with identically oriented principal axes and an electric field directed along one of their axes (c), this formula can be derived in various ways. The simplest of them consists in the replacement of the sphere depolarization factor 1/3 in the MG formula for spherical inclusions [2] by the spheroid depolarization factor $0 < A_c(\xi) < 1$, which depends on the aspect ratio ξ and corresponds to the electric-field orientation along the spheroid c axis. For the DC in the c direction, the MG formula for the composite is [3]

$$\varepsilon = \varepsilon_m \left[1 + \frac{\eta}{(1 - \eta)A_c + \varepsilon_m/(\varepsilon_{inc} - \varepsilon_m)} \right]. \qquad (1)$$

In agreement with the numerous experimental data [4] and theoretical results [3, 5], the DC calculated by Eq. (1) increases monotonically with η in the absence of or for small dielectric loss.

3. Giant increase in dielectric constant. Since the conductivities γ_{inc} and γ_m of the components are always nonzero, the inclusion DC $\varepsilon_{inc} = \varepsilon'_{inc} + i\gamma_{inc}/\omega$ and the matrix DC $\varepsilon_m = \varepsilon'_m + i\gamma_m/\omega$ (ω is the circular frequency of a harmonic electric field) become complex and frequency-dependent. After the substitution of the complex values of ε_{inc} and ε_m into Eq. (1) and analysis of the concentration dependence of the complex DC $\varepsilon = \varepsilon' + i\varepsilon''$ of the composite, one finds that the $\varepsilon'(\eta)$ dependence becomes nonmonotonic (Fig. 1). At $\eta \longrightarrow 0$ (or, depending on the γ_{inc}/γ_m, at $\eta \longrightarrow 1$), the static DC ε_0 of the composite with oblate ($\xi \ll 1$) spheroids drastically (by more than an order of magnitude) increases. The physical mechanism of a giant dielectric enhancement is the same as for the 2–2 composites with layers arranged in series [6, 7]; for instance, at $\eta \longrightarrow 0$, a free electric charge is efficiently accumulated at the boundaries of a strongly conducting matrix with thin weakly conducting oblate inclusions.

A giant increase in the composite DC is observed only at low frequencies. As the frequency ω increases, a giant dielectric relaxation occurs in the system, anal-
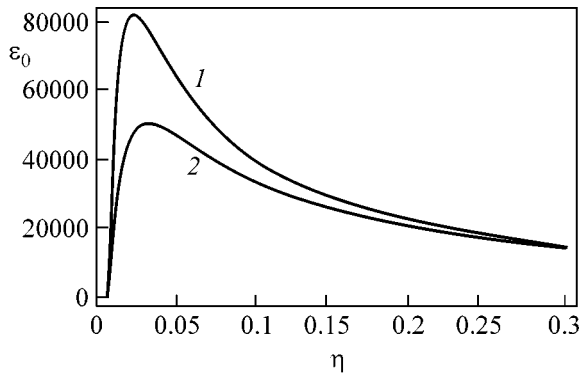
Fig. 1. Dependence of the static dielectric constant ε_0 of a 0–3 composite on the concentration of oblate spheroids for $c/a = 0.01$, $A_c = 0.9845$, $\varepsilon'_m = 500$, and $\varepsilon'_{inc} = 5000$: (*1*) $\gamma_m = 10^{-6}$ Ω^{-1} m^{-1} and $\gamma_{inc} = 10^{-12}$ Ω^{-1} m^{-1}, and (*2*) $\gamma_m = 10^{-10}$ Ω^{-1} m^{-1} and $\gamma_{inc} = 10^{-12}$ Ω^{-1} m^{-1}.
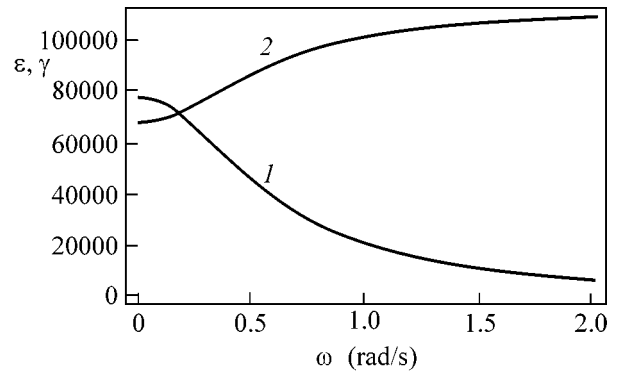

Fig. 2. Frequency dependences of the dielectric constant ε and conductivity $\gamma = \omega\varepsilon''$ of a 0–3 composite for $\eta = 0.01$, $c/a = 0.01$, $A_c = 0.9845$, $\varepsilon'_m = 500$, $\varepsilon'_{inc} = 5000$, $\gamma_m = 10^{-6}$ Ω^{-1} m^{-1} and $\gamma_{inc} = 10^{-12}$ Ω^{-1} m^{-1}: (*1*) ε' and (*2*) γ (10^{-12} Ω^{-1} m^{-1}).

ogous to the Maxwell–Wagner relaxation in layered 2–2 composites [6]. The dielectric spectrum has the Debye character, and the relaxation time

$$\tau = \frac{(1-\eta)A_c(\varepsilon_{inc} - \varepsilon_m) + \varepsilon_m}{(1-\eta)A_c(\gamma_{inc} - \gamma_m) + \gamma_m} \qquad (2)$$

depends on η, $A_c(\xi)$, and the ratios between the DCs and conductivities of the inclusions and matrix, while the low-frequency (static, $\omega\tau \ll 1$) and high-frequency ($\omega\tau \gg 1$) real parts ε' of DC are strongly different. The fragments of the frequency-dependent DC $\varepsilon = \varepsilon'$ and conductivity $\gamma = \omega\varepsilon''$ of the composite near the relaxation frequency ($\omega\tau \approx 1$) are shown in Fig. 2. A DC plateau at $\omega\tau \ll 1$, a sharp decrease in ε', and increase in γ near $\omega\tau \approx 1$ are seen in the figure. Upon further increase in frequency, $\varepsilon \longrightarrow \varepsilon_\infty$, and the ratio of static to high-frequency DC of the composite $\varepsilon_0/\varepsilon_\infty \longrightarrow 160$; i.e., a giant dielectric relaxation takes place. Therefore, the accumulation of a volume charge at the matrix and inclusion boundaries can be used in the fabrication of materials with a very high DC and giant dielectric relaxation.

4. Collective dielectric resonance. An alternative possibility of a giant increase in the DC of a 0–3 composite, called collective dielectric resonance, has recently been described by Oraevskiĭ in [8]. In the case of the collective resonance in a heterogeneous material composed of matrix-isolated ellipsoids, the concentration dependence $\varepsilon'(\eta)$ has the resonance character even for real ε_{inc} and ε_m: $\varepsilon \longrightarrow \pm\infty$ at a certain critical inclusion concentration η_c dependent on the inclusion shape and DCs ε_{inc} and ε_m. Such a behavior is well known for solid solutions of ferroelectrics; it describes a morphotropic phase transition from the paraelectric to the ferroelectric phase [9], which is observed neither in conventional insulators nor in their composites. As in this work, Oraevskiĭ [8] used the MG formula. For this rea-

son, the anomalous behavior of $\varepsilon'(\eta)$, as well as the conclusion [8] that the imaginary part of the composite DC becomes negative ($\varepsilon'' < 0$) upon exceeding a certain value of η in an absorbing matrix, i.e., that the composite transforms into an amplifying medium, can be ascribed to the drawbacks of the MG formula.

In our opinion, the discrepancy between our results and the results obtained in [8] is caused by the fact that the MG formula used by Oraevskiĭ, which, as can easily be shown, has the form

$$\varepsilon = \varepsilon_m\left[1 + \frac{\eta}{(A_c - \eta/3) + \varepsilon_m/(\varepsilon_{inc} - \varepsilon_m)}\right], \qquad (3)$$

is incorrect. Contrary to Eq. (1), the denominator in Eq. (3) contains the term $\eta/3$ instead of ηA_c; i.e., along with the spheroid depolarization factor A_c, the sphere depolarization factor $1/3$ is used in Eq. (3), thereby misrepresenting the spheroid dipolar interaction and rendering the use of Eq. (3) unjustified for the spheroidal inclusions (we use the standard values for A_c [10] that are half as large as those used in [8]). Equation (3) coincides with Eq. (1) only for the spherical inclusions ($A_c = 1/3$) and at $\eta \longrightarrow 0$. In both Eqs. (1) and (3), the DC can be complex. According to Eq. (1), the denominator turns to zero for none of the inclusion concentrations $0 < \eta < 1$ if the real part of DC is positive and $0 < A_c < 1$. For this reason, a collective dielectric resonance, as well as negative values $\varepsilon'' < 0$ of the composite, should not occur.

Figure 3 shows the concentration dependences of the real and imaginary parts of the composite DC $\varepsilon = \varepsilon' + i\varepsilon''$, to demonstrate that the collective resonance is impossible for the numerical values of ε_{inc}, ε'_m, and ε''_m used in [8]. One can see in Fig. 3 that the composite DC ε calculated for the prolate spheroids ($\xi \approx 5.4$, $A_c = 0.05$) using MG formula (1) increases monotonically
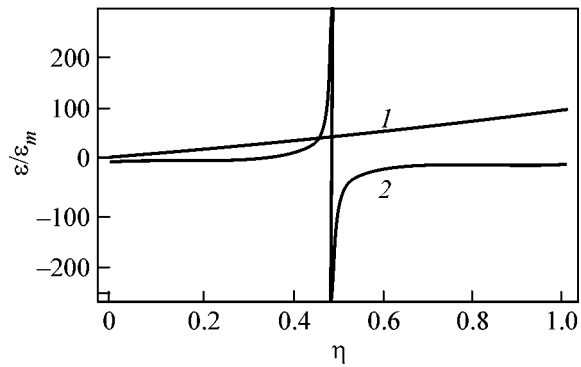
Fig. 3. Dependence of the effective dielectric constant of a 0–3 composite on the concentration of prolate spheroids for $\varepsilon''_{inc} = \varepsilon'_m = 0$: ($1$) $\varepsilon'/\varepsilon'_m \times 10$ calculated by formula (1) and (2) $\varepsilon'/\varepsilon'_m$ calculated by formula (3); $c/a \approx 5.4$, $A_c = 0.05$, and $\varepsilon'_{inc}/\varepsilon'_m = 10$.

from ε_m at $\eta = 0$ to ε_{inc} at $\eta = 1$ if $\varepsilon''_{inc} = \varepsilon''_m = 0$. A sharp resonance $\varepsilon/\varepsilon_m \longrightarrow \pm\infty$ predicted by Eq. (3) at $\eta_c = 0.483$ and the negative values of composite DC at large inclusion concentrations $\eta > \eta_c = 0.483$ do not occur in the MG approximation.

REFERENCES

1. R. E. Newnham, D. P. Skinner, and L. E. Cross, Mater. Res. Bull. **13**, 525 (1978).
2. J. C. Maxwell-Garnett, Philos. Trans. R. Soc. London, Ser. A **203**, 385 (1904).
3. G. Banhegyi, Colloid Polym. Sci. **264**, 1030 (1986).
4. T. Furukawa, K. Ishida, and E. Fukada, J. Appl. Phys. **50**, 4904 (1979).
5. C.-W. Nan, Phys. Rev. B **63**, 176201 (2001).
6. A. V. Turik and G. S. Radchenko, J. Phys. D: Appl. Phys. **35**, 1188 (2002).
7. G. S. Radchenko and A. V. Turik, Fiz. Tverd. Tela (St. Petersburg) **45**, 1676 (2003) [Phys. Solid State **45**, 1759 (2003)].
8. A. N. Oraevskiĭ, Pis'ma Zh. Éksp. Teor. Fiz. **78**, 8 (2003) [JETP Lett. **78**, 5 (2003)].
9. G. A. Smolenskiĭ, V. A. Bokov, V. A. Isupov, N. N. Kraĭnik, R. E. Pasynkov, A. I. Sokolov, and N. K. Yushin, *The Physics of Ferroelectric Phenomena* (Nauka, Leningrad, 1985).
10. A. P. Vinogradov, *Electrodynamics of Composite Materials* (Editorial, Moscow, 2001).

Translated by V. Sakun

Condensate Formation and Vortex Generation in Bose Gas upon Cooling

E. A. Brener[1], S. V. Iordanskiĭ[2], and R. B. Saptsov[2]

[1] *Institut für Festkörperforschung, Forschungzentrum Jülich, 52425 Jülich, Germany*
[2] *Landau Institute for Theoretical Physics, Russian Academy of Sciences,*
Chernogolovka, Moscow region, 142432 Russia
Received March 25, 2003; in final form, April 8, 2004

The mechanism of transition of a Bose gas to the superfluid state via thermal fluctuations under the condition of external cooling at a temperature above the transition point is considered. The probability of formation of such critical fluctuations (instantons) is calculated; it is found that this probability increases as the system approaches the transition temperature. It is shown that the evolution of an individual instanton is impossible without the formation of vortices in its superfluid part. © *2004 MAIK "Nauka/Interperiodica"*.

PACS numbers: 03.75.Nt; 67.40.Vs

The ideas of the kinetics of phase transitions have been thoroughly developed for first-order phase transitions and envisage the existence of the metastable phase itself and an equilibrium critical nucleus. The corresponding theory was worked out in [1, 2] and described in detail in [3]. However, theoretical concepts concerning the kinetics of second-order phase transitions, where these two facts do not exist, have been developed insufficiently. Lifshits [4] proposed a certain special model for the formation of an ordered phase after the fast phase-transition stage in the "short-range" order in the presence of only two types of ordering.

The interest in the problem of a phase transition upon a fast change in external parameters (e.g., temperature) has been aroused in connection with the cosmological ideas of the Big Bang, where the rapidly expanding Universe must be cooled and pass through a series of phase transformations accompanied by a change in the symmetry of physical fields [5]. It was proposed that the kinetics of these transformations can be modeled in condensed matter [6].

Zurek [7] proposed a theory of the second-order phase transition upon a rapid change in temperature in liquid He_4. The main assumption in the proposed mechanism is about the "critical retardation" of all processes in the vicinity of the transition temperature and "fast" formation of the nuclei of a new phase upon the subsequent cooling. This gives rise to a large number of defects on the order of the number of fluctuations far above the transition point.

However, no retardation in the formation of a new phase has been detected experimentally; the critical retardation is associated with the duration of the equilibration process at macroscopic distances, which is insignificant for the nonuniform process of formation of a new phase.

In this work, we consider the transition to a new phase via the evolution of fluctuations on scales much smaller than the correlation length, which can occur quite rapidly even in the vicinity of the critical temperature. The transition kinetics in this case are found to be directly related to the cooling process itself. We will consider the formation of a condensate in the model of a weakly nonideal Bose gas with external cooling and demonstrate a certain analogy with the first-order phase transitions.

The standard theory of a weakly nonideal Bose gas involves a Hamiltonian of the form

$$\hat{H} = \sum_p \frac{\hat{p}^2}{2m} \hat{a}_p \hat{a}_p^+ + \frac{2\pi\hbar^2 a_0}{m} \sum_p a^+_{p_4} a^+_{p_3} a_{p_2} a_{p_1}, \quad (1)$$

where a_0 is the scattering amplitude having the atomic scale and m is the atomic mass. The properties of such gas for a small density n (the smallness is determined by the gas parameter $\eta = na_0^3 \ll 1$) are close to the properties of an ideal Bose gas with the transition temperature [8]

$$T_c = \frac{3.31}{\sqrt{2}} \frac{\hbar^2 n^{2/3}}{m}. \quad (2)$$

At temperatures below the transition point, the ideal Bose gas has a pressure depending only on the temperature,

$$p_{id} = 0.0851 \frac{m^{3/2} T^{5/2}}{\hbar^3}, \quad (3)$$

which corresponds to zero isothermal sound velocity.

Considering that the scattering amplitude differs from zero, we can write the qualitative equation of state below the transition point:

$$P = P_{id}(T) + \frac{\hbar^2 a_0 n^2}{m}. \tag{4}$$

We omitted the insignificant constant factor in the second term.

The entire kinetics is essentially determined by the Bose-gas cooling mechanism. We will consider a simple model where the Bose gas is in a certain solid matrix with which it only slightly interacts. Such a situation may take place, for example, for the exciton gas in a crystal. The crystal can be rapidly cooled to a low temperature; in this case, the Bose-gas cooling proceeds via phonon emission. Assuming that the heat capacity of the crystal is large compared to the Bose gas, we can disregard the presence of thermal phonons in the crystal and their effect on the Bose gas. As a result, we obtain a uniform energy-loss mechanism, which is described by a phenomenological quantity T/τ_{ph}. The other models of cooling necessitate the analysis of heat transfer at the sample boundaries, which is a much more complicated problem. The loss rate $1/\tau_{ph}$ is determined by the collisions of particles with each other and by the interaction with phonons, which will be regarded as weak,

$$1/\tau_{ph} \ll 1/\tau_{tr}.$$

Since $1/\tau_{ph} \sim n v_T \sigma_{ph}$ and $1/\tau_{tr} \sim n v_T a_0^2$ (v_T is the thermal velocity), this means that

$$\sigma_{ph} \ll a_0^2,$$

where σ_{ph} is the cross section for scattering with phonon emission, which corresponds to the weak interaction of Bose gas with the crystal.

In view of the smallness of quantity $1/\tau_{ph}$, the evolution of the Bose system is slow; in particular, we assume that the acoustic wavelength $c\tau_{ph} \sim v_T \tau_{ph}$ is large compared to the characteristic length $\sim \sqrt{\chi \tau_{ph}}$, where χ is the thermal diffusivity,

$$\frac{\sqrt{\chi \tau_{ph}}}{v_T \tau_{ph}} \sim \sqrt{\frac{l^2}{v_T^2 \tau_{tr} \tau_{ph}}} \sim \sqrt{\frac{\tau_{tr}}{\tau_{ph}}} \ll 1$$

(l stands for the mean free path). This makes it possible to assume that the fluctuation evolution occurs at a constant pressure that coincides with the thermodynamically equilibrium pressure.

It follows from Eq. (4) that the density variation δn in the fluctuation region is related to a change in temperature by

$$\frac{\delta n}{n} = -\frac{\delta T}{T} \frac{1}{\eta^{1/3}}. \tag{5}$$

The relative density fluctuation is large compared to the relative temperature fluctuation in the temperature range $T < T_c$. This leads to a rapid increase in the reciprocal phonon time

$$\delta \frac{1}{\tau_{ph}} \sim -\frac{\delta T}{T} \frac{1}{\eta^{1/3}} \frac{1}{\tau_{ph}^0} \tag{6}$$

(where $1/\tau_{ph}^0 = n v_T \sigma_{ph}$) with decreasing temperature and enhancement of cooling in the fluctuation region. For this reason, we will disregard the phonon emission in the region far from the developed fluctuations, assuming that

$$\frac{1}{\tau_{ph}} \sim -\frac{\delta T}{T_c} \frac{1}{\eta^{1/3}} \frac{1}{\tau_{ph}^0} U(T_c - T), \tag{7}$$

where $U(T_c - T) = 1$ for $\delta T = T - T_c < 0$ and $U(T_c - T) = 0$ for $T - T_c > 0$.

This allows us to consider the problem of fluctuation kinetics within the framework of the theory of hydrodynamic fluctuations by supplementing the hydrodynamic equations with the energy flux carried away as a result of phonon emission:

$$\frac{T}{\tau_{ph}^0} \frac{\delta n}{n} = -\frac{T_c - T}{\tau_{ph}} U(T_c - T), \tag{8}$$

where $1/\tau_{ph} = (1/\tau_{ph}^0)(1/\eta^{1/3})$. In view of the constancy of pressure, we can describe the evolution of temperature fluctuations by the heat conduction equation

$$n c_p \left(\frac{\partial T}{\partial t} + \mathbf{v} \nabla T \right) = \nabla(\kappa \nabla T) + \frac{T - T_c}{\tau_{ph}} n c_p U(T_c - T), \tag{9}$$

where the energy flux carried away by phonons is added, κ is the heat conductivity, and c_p is the specific heat per particle under a constant pressure. This equation contains the drift term with mass velocity $\mathbf{v}(\mathbf{r})$, which appears due to the high density in the fluctuation core. In the following analysis, this term will be omitted as a higher-order term in fluctuation. We are interested in the temperature-field fluctuations and their time evolution. To analyze these fluctuations, we must introduce random heat fluxes $\mathbf{q}$ [3, 9], i.e., the Langevin term $\nabla \mathbf{q}$. These fluxes are delta-correlated (i.e., correlated at distances and time intervals smaller than the hydrodynamic scales). In the case considered, this is ensured by the fact that the time $\sqrt{\chi \tau_{ph}}$ and distance $\sqrt{\chi \tau_{ph}}$ (χ is thermal diffusivity) are larger than the microscopic characteristics. It is well known that the probability $W_t(T(r))$ of realizing the given configuration $T(r)$ of

fluctuation field at time t obeys the Fokker–Planck equation in variational derivatives [10]:

$$\frac{\partial}{\partial t} W = -\int \frac{\delta}{\delta T(r)} \left[\frac{\chi T_\infty^2}{n c_p} \nabla^2 \frac{\delta}{\delta T(r)} W \right.$$
$$\left. + \left[\chi \nabla^2 T + U(T_c - T) \frac{T - T_c}{\tau_{\text{ph}}} \right] W \right] d^3 r. \tag{10}$$

In the absence of the interaction with phonons, the stationary solution to this equation coincides with the result obtained in the thermodynamic theory of fluctuations. The quantity

$$\chi \nabla^2 T + U(T_c - T) \frac{T - T_c}{\tau_{\text{ph}}} = \frac{\partial T}{\partial t} \tag{11}$$

is the temperature-variation rate upon the deviation from the mean value $T = T_\infty$.

We assume that fluctuations occur at a fixed temperature $T_\infty > T_c$. Fluctuations with $\Delta T = T - T_\infty \ll T_\infty$ occur quite frequently and are characterized by a certain (in fact, stationary) spatial distribution that determines the value of $W_t(T)$. In view of the normalization, the latter quantity gives the number of small fluctuations in a unit volume. However, rare large-amplitude fluctuations with $\Delta T \sim T_c - T_\infty$ ($T < T_c$) also sometimes occur, initiating the effective cooling by phonons, so that the fluctuation becomes irreversible and the nucleus of a new phase appears. Our goal is to calculate the probability of such fluctuations in a unit volume per unit time. Since they are infrequent and the distribution at small $T_\infty - T$ is stationary, one can use the method of characteristics to determine the exponentially low probability of formation of such a nucleus (instanton for the Fokker–Planck equation). An important difference from the theory of nucleation in the first-order phase transition is that the probability of instanton formation in this case is determined by the cooling process.

To clarify the situation, let us consider the instanton solution in the case of one degree of freedom, for which the Fokker–Planck equation has the form

$$\frac{\partial W}{\partial t} = \frac{\partial}{\partial x} \left(D \frac{\partial W}{\partial x} - v W \right), \tag{12}$$

where D is the constant diffusion coefficient and $v(x)$ is the macroscopic variation rate of the quantity x with allowance for its relaxation upon the deviation from equilibrium and for an external effect (analogue of phonon emission). Setting $W = e^S$ and assuming that the moduli of S and its first derivative are large, we obtain, to leading terms, the equation

$$\frac{\partial S}{\partial t} = D \left(\frac{\partial S}{\partial x} \right)^2 - v \frac{\partial S}{\partial x} - \frac{\partial v}{\partial x}. \tag{13}$$

This is the Hamilton–Jacobi equation with the Hamiltonian ($\partial S / \partial x = p$)

$$H \left(\frac{\partial S}{\partial x}, x \right) = -D p^2 + p v + \frac{\partial v}{\partial x}.$$

The Hamilton equations are the characteristics of this equation in partial derivatives,

$$\frac{dx}{dt} = -2 D p + v,$$

$$\frac{dp}{dt} = -\frac{dv}{dx} p - \frac{d^2 v}{d^2 x}.$$

The contribution of the velocity divergence to the Hamiltonian is significant only in the vicinity of the point at which $v = 0$. We are interested in the special solution that passes through the equilibrium point $p = 0$, $v = 0$. In the 1D Fokker–Planck equation, one can eliminate the term with a first derivative by substitution; in this case, we have an analogy with quantum mechanics and can use the well-known results. Nevertheless, we will use direct estimates in the vicinity of $v = 0$.

In the Hamilton equation, the energy is conserved. In view of the smallness of the divergence term, this gives $H = -D p^2 + p v = 0$, whence $p = v/D$ and

$$S = -\int \frac{v^2}{D} dt = \int_0^{x^*} \frac{v}{D} dx.$$

We assume that the velocity $v(x)$ is a convex-down function with two zeros (stable at zero and unstable at x^*). Such a shape of the function $v(x)$ is ensured by the entire cooling process, including phonon emission. For $x > x^*$, the solution tends to larger values of x, while the action is gathered from zero to x^*, where $v < 0$. In the vicinity of x^*, we must take into account the quantity dv/dx. For large values of x, p^2 can be ignored, yielding $p \approx -\frac{dv}{dx}/v$; consequently,

$$S \sim S_0 - \ln(v/v_0),$$

where v_0 is the effective velocity in the region where the solutions for $x < x^*$ and $x > x^*$ match. The solution itself has the form $e^S \approx (v_0/v) e^{S_0}$, and current $j \approx v_0 e^{S_0}$. One can estimate the value of v_0, assuming that all terms in the Hamiltonian H are of the same order of magnitude:

$$D p^2 \sim v p \sim \frac{dv}{dx} \sim \frac{v_{\text{max}}}{x^*},$$

which gives

$$v_0 \sim \sqrt{\frac{D |v_{\text{max}}|}{x^*}} \sim \frac{|v_{\text{max}}|}{\sqrt{|S_0|}}. \tag{14}$$

In the many-dimensional case, the situation is the same,

$$\frac{dx^i}{dt} = -2D^{ij}p_j + v^i,$$

$$\frac{dp_i}{dt} = -\frac{\partial v^k}{\partial x^i}p_k - \frac{\partial(\text{div}\,\mathbf{v})}{\partial x^i},$$

where $p = 0$ at the beginning and $p \longrightarrow 0$ at the end of the trajectory. Consequently, $|p|$ reaches its maximal value somewhere on the trajectory. At this point, the matrix $\partial v_i/\partial x_k$ has one zero eigenvalue and $\mathbf{p}$ is tangent to the corresponding eigenvector; subsequently, the trajectory passes to the neighborhood of the point corresponding to zero velocity $\mathbf{v}$. This leads to the definition of the critical fluctuation (instanton) as a solution passing through the point $\mathbf{x} = \mathbf{p} = 0$, whereupon $\mathbf{p} \longrightarrow 0$ for $|x| \longrightarrow \infty$ as $1/v$, retaining the probability flux at a constant level.

An analogous procedure can be carried out for the field as well. In this case, the Hamiltonian has the form, in accordance with (10),

$$H = \int p(\mathbf{r})\left[\frac{\chi T_\infty^2}{nc_p}\nabla^2 p(\mathbf{r})\right.$$

$$\left. + \chi\nabla^2 T + U(T_c - T)\frac{T - T_c}{\tau_{\text{ph}}}\right]d^3 r \tag{15}$$

with the Hamilton equations

$$\frac{\partial T}{\partial t} = \frac{2\chi T_\infty^2}{nc_p}\nabla^2 p(\mathbf{r}) + \chi\nabla^2 T + U(T_c - T)\frac{T - T_c}{\tau_{\text{ph}}}, \tag{16}$$

$$\frac{\partial p}{\partial t} = -\chi\nabla^2 p - \frac{p}{\tau_{\text{ph}}}U(T_c - T). \tag{17}$$

Here, $p = \delta S/\delta T(\mathbf{r})$. Equations (16) and (17) define the critical fluctuation and can be reduced to dimensionless variables by the substitutions $\xi = r/\sqrt{\chi\tau_{\text{ph}}}$, $\tau = t/\tau_{\text{ph}}$,

$$\Theta = \frac{T - T_c}{T_\infty - T_c}, \quad p = \frac{nc_p(T_\infty - T_c)\Pi}{T_\infty^2},$$

where Θ and Π are the new dimensionless fields. In this case, the dimensionless equations have the form

$$\frac{\partial\Theta}{\partial\tau} = \nabla^2\Theta + \Theta U(-\Theta) + 2\nabla^2\Pi, \tag{18}$$

$$\frac{\partial\Pi}{\partial\tau} = -\nabla^2\Pi - \Pi U(-\Theta). \tag{19}$$

The solution should be found from the conditions $\Pi_{\xi\to\infty} \longrightarrow 0$, $\Pi_{\tau\to-\infty} \longrightarrow 0$, $\Theta_{\tau\to-\infty} \longrightarrow 1$, and $\Theta_{\xi\to\infty} \longrightarrow 1$ and pass through the neighborhood of $\partial\Theta/\partial\tau \approx 0$ and $\Pi \approx 0$ at $\tau \longrightarrow \tau^*$, after which $\partial\Theta/\partial\tau \approx \nabla^2\Theta + \Theta U(-\Theta)$ and the fluctuation is developed

through cooling, while the random fluxes can be neglected. Since $H = 0$, the action is given by

$$S = \int p\frac{\partial T}{\partial t}d^3 r dt$$

$$\approx \int_{-\infty}^{\tau^*}\frac{nc_p(T_\infty - T_c)^2\Pi}{T_\infty^2}\frac{\partial\Theta}{\partial\tau}(\sqrt{\chi\tau_{\text{ph}}})^3 d\tau d^3\xi \tag{20}$$

$$= s_0\frac{nc_p(T_\infty - T_c)^2}{T_\infty^2}(\sqrt{\chi\tau_{\text{ph}}})^3.$$

The negative constant s_0 can be determined from the numerical solution to Eqs. (18) and (19). It is a universal number corresponding to the largest action S_0 and is independent of the values of physical constants and the difference $T_\infty - T_c$.

To estimate the temperature-variation rate, one can take

$$|v_{\text{max}}| = \frac{T_\infty - T_c}{\tau_{\text{ph}}}(\sqrt{\chi\tau_{\text{ph}}})^3 n.$$

In this case, in accordance with Eq. (14), one can write for the probability flux in the transition region

$$j \sim \frac{T_\infty(n(\sqrt{\chi\tau_{\text{ph}}})^3)^{1/2}}{\tau_{\text{ph}}c_p}e^{S_0}v.$$

The constant v cannot be estimated from the theory of hydrodynamic fluctuations [11]. This quantity gives the number of small equilibrium fluctuations with $\delta T \ll T$ on the atomic scale in a unit volume. As an estimate, we can use the relation $v = n/T_\infty$. Thus, the number of critical fluctuations arising per unit time in a unit volume is

$$\frac{dN}{dt} \sim \frac{n(n(\sqrt{\chi\tau_{\text{ph}}})^3)^{1/2}}{\tau_{\text{ph}}c_p}\exp\left(s_0\frac{nc_p(T_\infty - T_c)^2}{T_\infty^2}(\sqrt{\chi\tau_{\text{ph}}})^3\right).$$

Thus, the nuclei of a new phase are intensely formed as T_∞ approaches T_c and then grow rapidly. We have considered the initial phase of critical-fluctuation growth and restricted our analysis only to the heat transfer via heat conduction, disregarding the superfluidity effects at this stage. This approximation can be justified by the fact that the largest contribution to the action comes from the region lying far from the region of low velocities v, where $p(\mathbf{r}) = \delta S/\delta T(\mathbf{r})$ becomes small and the fluctuation contribution can be neglected because $W \sim v^{-1}e^{S_0}$.

Analysis of the subsequent growth of the instanton requires the solution of hydrodynamic equations for a superfluid liquid, because a superfluid core appears in the developing fluctuation. We will qualitatively consider the phenomena that arise in this case. Proceeding from the assumption that the value of τ_{ph} is high, we assume that the motion in this region is quasi-stationary

and tuned to the slow cooling by phonons. We will use the hydrodynamic equations for a superfluid liquid in the vicinity of the transition point in the form proposed by Khalatnikov [12]:

$$\frac{\partial \mathbf{v}_s}{\partial t} = -\nabla\left(\frac{v_s^2}{2} + \mu + \mu_s\right),$$

$$\frac{\partial \rho}{\partial t} + \mathrm{div}(\rho_s v_s + \rho_n v_n) = 0,$$

$$\frac{\partial}{\partial t}(\rho_s v_s^i + \rho_n v_n^i) + \frac{\partial}{\partial x^k}(\rho_n v_n^i v_n^k + \rho_s v_s^i v_s^k + p\delta^{ik}) = 0,$$

$$T\frac{\partial n\sigma}{\partial t} + T\mathrm{div}\,n\sigma \mathbf{v}_n$$

$$= \frac{2\Lambda m}{\hbar}\left[\mu_s + \frac{(\mathbf{v}_n - \mathbf{v}_s)^2}{2}\right]^2 \rho_s - \frac{\rho_s c_p T}{m\tau_{\mathrm{ph}}},$$

$$\frac{\partial \rho_s}{\partial t} + \mathrm{div}\rho_s \mathbf{v}_s = -\frac{2\Lambda_m}{\hbar}\left[\mu_s + \frac{(\mathbf{v}_n - \mathbf{v}_s)^2}{2}\right]\rho_s.$$

Here, σ is the entropy per particle, n is the number of particles per unit volume, and ρ is the density. The subscripts n and s correspond to the normal and superfluid components, respectively; the constant Λ is the relaxation parameter; and we introduced the term that accounts for the phonon-induced energy removal in the equation for entropy. Here, the specific chemical potential μ_s for the superfluid density should ensure the condensate equilibrium density that is obtained by equating to zero the relaxation right-hand side of the equation for ρ_s. In our model of a weakly nonideal Bose gas, we can define phenomenologically

$$\mu_s = -\frac{\hbar^2 a_0}{m^2}[(n - n(T))] + \frac{\hbar^2 a_0}{m^3}\rho_s,$$

so that $\rho_s = m(n - n(T) = m\delta n$ in the equilibrium. Here, $n(T)$ is the number of particles outside the condensate. We assume that the quantity $\Lambda m/\hbar$ is large and $T_c - T$ is large enough for the approximate equality $\mu_s + v_s^2/2 \approx 0$ to be satisfied (we disregard quantity v_n, which is small compared to v_s); this gives

$$\frac{\rho_s}{m} = \delta n - \frac{v_s^2 m^2}{2\hbar^2 a_0} = \delta n\left(1 - \frac{v_s^2 m^2}{2\hbar^2 a_0 \delta n}\right). \quad (21)$$

In this case, it follows from the hydrodynamic equations that $\mu \approx \mu(P, T) = \mathrm{const}$,

$$T\frac{\partial n\sigma}{\partial t} + T\mathrm{div}\,n\sigma\mathbf{v}_n = -\frac{c_p T\rho_s}{m\tau_{\mathrm{ph}}},$$

and the momentum conservation law gives

$$\frac{\partial}{\partial t}(\rho_s v_s^i + \rho_n v_n^i) + \frac{\partial}{\partial x^k}(\rho_n v_n^i v_n^k + \rho_s v_s^i v_s^k + P\delta^{ik}) = 0.$$

In view of the smallness of v_s compared to the sound velocity and the smallness of ρ_s, we will neglect these corrections to pressure $P \approx P_0$. In this case, only the equation for entropy is significant. Assuming that the derivative $\partial n\sigma/\partial t$ is small, according to the assumption that the process is quasi-stationary (low temperature-variation rate $\frac{\partial T}{\partial t} \sim \frac{T}{\tau_{\mathrm{ph}}}\frac{1}{\sqrt{n_0(\chi\tau_{\mathrm{ph}})^{3/2}}}$), we find that the stationary regime $\mathrm{div}\,n\sigma\mathbf{v}_n = -c_p\rho_s/m\tau_{\mathrm{ph}}$ should approximately take place and that the mass flux should be zero ($\rho_s\mathbf{v}_s + \rho_n\mathbf{v}_n = 0$). Considering that $\rho_n \approx \rho$, we obtain the equation

$$-\sigma\mathrm{div}\rho_s v_s = -\frac{c_p\rho_s}{\tau_{\mathrm{ph}}},$$

where σ is the entropy per particle. This equation determines the heat transfer in the fluctuation superfluid core. Using Eq. (21), we obtain

$$\sigma\frac{1}{r^2}\frac{\partial}{\partial r}r^2\left(1 - \frac{v_s^2}{u^2}\right)v_s - \left(1 - \frac{v_s^2}{u^2}\right)\frac{c_p}{\tau_{\mathrm{ph}}} = 0, \quad u^2 = \frac{2\hbar^2 a_0\delta n}{m^2}.$$

By introducing the dimensional distance $\xi = c_p r/\sigma u\tau_{\mathrm{ph}}$, we arrive at the equation

$$\frac{\partial v}{\partial \xi} = \frac{(1 - v^2)\left(1 - \frac{2}{\xi}v\right)}{1 - 3v^2}. \quad (22)$$

The singular points of this differential equation are

$$\xi = 0, \quad v = 0 \text{ and } \xi = \frac{2}{\sqrt{3}}, \quad v = \frac{1}{\sqrt{3}},$$

the latter point being a focus with the eigenvalues $\lambda = 1 \pm i\sqrt{5}$. Since the velocity v must vanish at $\xi = 0$, $v \approx \frac{1}{3}\xi$ for small ξ and increases faster than by the linear law, with the derivative $d\xi/dv$ vanishing at $v = 1/\sqrt{3}$ and at a certain $\xi = \xi^*$, whereupon the derivatives assume negative values upon the further increase in v. Thus, a regular superfluid flow cannot be continued after the point ξ^* (the constant is on the order of unity and can be determined numerically). The physical length

$$r^* \sim \frac{\sigma u\tau_{\mathrm{ph}}}{c_p} = \frac{\sigma}{c_p}\sqrt{2\frac{\delta n}{n}}\eta^{1/3}\frac{\tau_{\mathrm{ph}}}{\tau_{\mathrm{tr}}}\sqrt{\chi\tau_{\mathrm{ph}}}$$

can be smaller than $\sqrt{\chi\tau_{\mathrm{ph}}}$; it should also be noted that $1 - v^2 > 0$ (i.e., a singularity appears in the superfluid

core). This singularity indicates that the quasi-stationarity conditions are violated at $\xi \gtrsim \xi^*$, and a complex nonstationary superfluid flow with the intense vortex formation in an instanton should appear upon the transition to the normal liquid at $T > T_c$. Similar effects are observed in a superfluid liquid in the gravitational field, where T_c is a function of one (vertical) coordinate and a fixed heat flux from the superfluid to the normal liquid takes place [13]. We are dealing with a similar situation arising due to the nonuniform cooling as the critical temperature in the superfluid nucleus is approached. The results of numerical calculation [14] and experimental data [15, 16] indicate the formation of a "vortex" superfluid phase with a higher but finite thermal conductivity without a superfluid transport. The mechanism of vortex formation and the vortex phase of this kind have been poorly studied both theoretically and experimentally.

Thus, we have shown that, in contrast to [7], a transition to the superfluid phase can occur through an independent growth of critical fluctuations (instantons) at temperatures above the critical point ($T > T_c$) immediately in the course of external cooling. These fluctuations subsequently transform into macroscopic formations. The growth of the nucleus of the superfluid state is accompanied by vortex generation in its external part. Consequently, vortex defects appear both due to the independent nucleation with an arbitrary phase upon cooling (the Zeldovich–Kibble hypothesis) and directly during the growth of each superfluid nucleus. This vortex-generation mechanism during the growth of an instanton significantly differs from the mechanism determined in [17], where the existence of a superfluid flow interacting with the heated normal regions was presumed. In [17], an attempt was made to explain the results of experiments [18], in which ^{3}He was bombarded by neutrons. As a result, regions heated to temperatures above T_c appeared. These regions were cooled by the surrounding superfluid ^{3}He, and the formation of vortices was detected. Thus, nonuniform cooling took place that differs considerably from the model used in our study. In the critical fluctuation considered here, heating takes place due to its nonsuperfluid surroundings. Consequently, it is advantageous for the fluctuation to preserve its spherical symmetry to reduce this heating. In the case of cooling of a heated region with superfluid surroundings [18], the interface must obviously be unstable against its shape distortions, because this leads to a faster cooling. However, the stability, as well as the phase-transition mechanism itself, under such conditions (which, in contrast to [17], are not associated with the existence of an external superfluid flow) calls for detailed investigations.

REFERENCES

1. R. Becker and W. Doering, Ann. Phys. (Leipzig) **24**, 719 (1935).
2. Ya. B. Zel'dovich, Zh. Éksp. Teor. Fiz. **112**, 525 (1942).
3. J. S. Langer, Ann. Phys. (N.Y.) **54**, 258 (1962).
4. I. M. Lifshits, Zh. Éksp. Teor. Fiz. **42**, 1354 (1962) [Sov. Phys. JETP **15**, 939 (1962)].
5. Ya. B. Zel'dovich, I. Yu. Kobzarev, and L. B. Okun', Zh. Éksp. Teor. Fiz. **67**, 3 (1974) [Sov. Phys. JETP **40**, 1 (1975)].
6. T. W. Kibble, J. Phys. A **9**, 1387 (1976).
7. W. H. Zurek, Phys. Rep. **276**, 177 (1996).
8. L. D. Landau and E. M. Lifshitz, *Course of Theoretical Physics*, Vol. 5: *Statistical Physics*, 5th ed. (Fizmatlit, Moscow, 2002; Pergamon Press, Oxford, 1980).
9. E. M. Lifshitz and L. P. Pitaevskiĭ, *Course of Theoretical Physics*, Vol. 9: *Statistical Physics*, 2nd ed. (Fizmatlit, Moscow, 2002; Pergamon, New York, 1980), Part 2, Chap. 9.
10. V. I. Klyatskin, *Stochastic Equations by the Eyes of a Physicist* (Fizmatlit, Moscow, 2001).
11. E. M. Lifshitz and L. P. Pitaevskiĭ, *Physical Kinetics* (Nauka, Moscow, 1979; Pergamon Press, Oxford, 1981).
12. I. M. Khalatnikov, *The Theory of Superfluidity* (Nauka, Moscow, 1971), Chap. 9.
13. Akira Onuki, J. Low Temp. Phys. **50**, 433 (1983).
14. P. B. Weichman and J. Miller, J. Low Temp. Phys. **119**, 155 (2000).
15. Feng Chuan Lui and Guenter Ahlers, Phys. Rev. Lett. **76**, 1300 (1996).
16. H. Baddar, G. Ahlers, K. Kuehn, and H. Fu, J. Low Temp. Phys. **119**, 1 (2000).
17. I. S. Aranson, N. B. Kopnin, and V. M. Vinokur, Phys. Rev. Lett. **83**, 2600 (1999).
18. V. H. M. Ruutu, V. B. Eltsov, A. J. Gill, *et al.*, Nature **382**, 334 (1996).

Translated by N. Wadhwa

Power-Law Statistics of Intermittent Photoluminescence in Single Semiconductor Nanocrystals

I. S. Osad'ko

Lebedev Physical Institute, Russian Academy of Sciences, Moscow, 117924 Russia
e-mail: osadko@sci.lebedev.ru
Received March 25, 2004

A physical model is proposed for a single CdSe nanocrystal coated with a ZnS shell which can explain the power-law statistics of its experimentally observed intermittent photoluminescence. If the localized electron–hole pairs (excitons) form in the nanocrystal, this suggestion alone will suffice to explain why the on-time distribution follows the law close to $t^{-1.5}$ found experimentally. © *2004 MAIK "Nauka/Interperiodica".*

PACS numbers: 78.55.Et; 78.67.Bf

1. The question of why the fluorescence of a single CdSe quantum dot (QD) with a ZnS shell is intermittent was raised seven years ago [1]. At the same time, the problem of a blinking QD was theoretically explained in [1, 2] based on a model of the Auger ionization of the QD followed by its neutralization. Though the model proposed in [2] allowed the intermittent fluorescence of a polyatomic object, such as a QD, to be explained, it predicted an exponential distribution of the duration of on- and off-time periods. It is this distribution of the on- and off-time periods that is commonly observed in the luminescence of single molecules [3–5].

However, it was already noted in the first studies of the intermittent fluorescence of QDs and nanocrystals [1, 6] that the on/off-time distribution is evidently non-exponential. Therefore, the off-time distribution measured three years ago in [7] for the fluorescence of CdSe nanocrystals, which exhibited a power-law behavior $1/t^{1+m}$ with $m = 0.5$–0.6 when the time varied within five orders of magnitude, was a clear challenge to the theory. Further investigations showed that the power-law behavior of the off-time distribution is inherent not only in CdSe nanocrystals [6–9] but in CdTe [8] and CdS [10] nanocrystals as well.

The most surprising was that the on-time distribution in a CdSe nanocrystal measured in [8], as well as the off-time distribution, was also described by the law close to $t^{-1.5}$. The authors of [7] suggested that there exists a certain universal reason for the appearance of the power-law dependence with such an exponent in the on- and off-time distributions. Below, a physical model is proposed that can describe the power-law statistics of both off- and on-time periods in the photoluminescence of semiconductor nanocrystals.

2. The number of electron–hole (e–h) pairs in a QD excited by a CW laser is determined by the equation $N = N_a L T_1$, where N_a is the number of atoms in the QD,

L designates the creation rate of an e–h pair, and $1/T_1$ is its radiative recombination rate. Even for moderate pumping obeying the condition $LT_1 \ll 1$, the number of e–h pairs existing in a QD under continuous pumping can be significantly greater than one.

Consider a QD that contain several localized e–h pairs (excitons) numbered by the subscript j and several traps in the system QD + shell numbered by the subscript k. In the case of Auger ionization, the recombination of one e–h pair is accompanied by the ejection of an electron of another pair from the QD. Then, taking for definiteness the Auger ionization as the ionization mechanism [1, 2], one can write the following system of equations describing the ionization and neutralization dynamics of a single QD:

$$\dot{\rho}_j = -(1/T_1 + \Gamma_j)\rho_j + L\rho_0,$$

$$\dot{\rho}_0 = \rho_j/T_1 - L\rho_0 + \sum_k \gamma_k \rho_{jk}, \qquad (1)$$

$$\dot{\rho}_{jk} = \Gamma_{jk}\rho_j - \gamma_k \rho_{jk},$$

where

$$\Gamma_j = \sum_k \Gamma_{jk}. \qquad (2)$$

Here, ρ_0 is the probability of finding N e–h pairs in the QD; ρ_j is the probability of finding the jth pair (whose electron is subsequently captured by a trap) in addition to the N e–h pairs; ρ_{jk} is the probability of finding an electron of the jth pair in the kth trap and the QD with $N–1$ e–h pairs. It is evident that Γ_{jk} is the probability of the jth e–h pair decay with the capture of its electron by the kth trap, and γ_k is the probability of the kth trap neutralization. It is evident that ρ_0 and ρ_j describe the fluorescent states of a neutral QD, that is, the probability

that the QD resides in the on-state; ρ_{jk} describe the states of the ionized QD, for which fluorescence is absent, that is, the probability that the QD is in the off state. It follows from Eqs. (1) and (2) that the probabilities are connected by the following relationship: $\rho_0 + \rho_j + \sum_k \rho_{jk} = 1$. The system of Eqs. (1) describes the dynamics of the QD ionization and neutralization process and allows the fluorescence autocorrelation function $g^{(2)}(t)$ to be calculated by the recipe described in [11]. However, of my interest is to calculate the on/off-time distribution functions. A recipe for finding equations for calculating the on/off-time distribution functions was also proposed in [11].

On states. To find equations for the on-time distribution functions, it is necessary to neglect the term in Eq. (1) that describes the transition to the on state from the off state, that is, the following term: $\sum_k \gamma_k \rho_{jk}$. Then, the two first equations containing the populations of fluorescent states are separated from the others and the on-time distribution function can be found from these two equations

$$\dot{\rho}_j = -(1/T_1 + \Gamma_j)\rho_j + L\rho_0,$$
$$\dot{\rho}_0 = \rho_j/T_1 - L\rho_0. \tag{3}$$

In a QD containing N_a atoms, the same number of e–h pairs can be generated. The subscript j numbers any of the possible e–h pairs. It is evident that $\rho_j^{on} = \rho_0 + \rho_j$ is the probability of residing in the on state with the possibility of this state decaying via the jth channel. Considering that $LT_1 \ll 1$ and being interested in the slow dynamics, one can set $\dot{\rho}_j = 0$. In this approximation, the first equation of the system of Eqs. (3) gives

$$\rho_j = \frac{LT_1}{1 + \Gamma_j T_1}\rho_0. \tag{4}$$

By adding the equations of system (3), one obtains the following equation:

$$\dot{\rho}_j^{on} = -L_j\rho_j^{on}, \tag{5}$$

where

$$L_j = L\frac{\Gamma_j T_1}{1 + \Gamma_j T_1 + LT_1} \tag{6}$$

is the decay rate of the on state via the jth channel. The summation over all decay channels of the fluorescent QD state leads to the following expression for the on-time distribution function:

$$w_{on}(t) = \frac{1}{N_a}\sum_{j=1}^{N_a} L_j e^{-L_j t}. \tag{7}$$

The experimental data [8] indicate that e–h pairs with various ionization times differing by three orders of magnitude can exist in a CdSe QD.

Off states. To find equations for the off-time distribution functions, it is necessary to neglect the term in Eq. (1) that describes the transition to the off state from the on state, that is, the term $\Gamma_{jk}\rho_j$. Then, the third equation of the system of Eqs. (1) is independent of the first two equations and the off-time distribution function can be found from the following equations:

$$\dot{\rho}_{jk} = -\gamma_k\rho_{jk}. \tag{8}$$

By solving these equations, one finds the following expression for the probability $\rho_k^{off} = \sum_{j=1}^{N_a} \rho_{jk}$ of finding the system in the ionized state after the electron capture by the kth trap:

$$w_k^{off} = \gamma_k e^{-\gamma_k t}. \tag{9}$$

The off-time distribution function under the condition that an electron is captured by any trap takes the following form:

$$w_{off}(t) = \frac{1}{N_t}\sum_{k=1}^{N_t} \gamma_k e^{-\gamma_k t}, \tag{10}$$

where N_t is the number of traps that can be achieved upon the QD ionization. The experimental data [8] indicate that traps with various ionization times differing by three orders of magnitude and more can exist in a CdSe QD.

3. Physical model of the on/off states. The band gaps of the CdSe and ZnS crystals, which served as the nanocrystal and the shell in [1, 8], are 1.85 and 3.84 eV, respectively. The photons of an Ar$^+$ laser with an energy of 2.54 eV create free electrons and holes. If the QD is considered as a perfect nanocrystal, the excitons with a wave function encompassing the entire QD will be the lowest energy states of the e–h pairs. However, a real QD can involve substantial disorder. The authors of [9] speak about "colloidal CdSe QD." Electrons (holes) in a disordered system will have wave functions that are localized on several atoms or, maybe, even on one atom. The ionization rate constant L_j describes the transition from the jth atom or a group of atoms to any trap located in the shell. The resulting Coulomb field quenches the luminescence of the remaining e–h pairs.

By passing in Eq. (7) from summation to integration, one obtains the following expression:

$$w_{on}(t) = \int_{j_1}^{j_2} L(j)\exp[-L(j)t]N_{on}(j)dj. \tag{11}$$

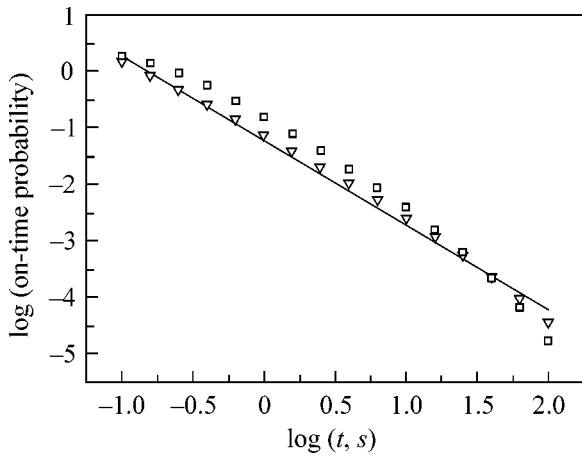Here, N_{on} describes the distribution of the excited localized e–h pairs in the QD. Because the distribution of

Fig. 1. On-time distribution calculated by Eq. (14) for (triangles) $L_{max} = 10^2$ s^{-1} and $L_{min} = 10^{-3}$ s^{-1} and (squares) $L_{max} = 10^1$ s^{-1} and $L_{min} = 10^{-2}$ s^{-1}. The solid line corresponds to the $t^{-1.5}$ function.

Fig. 2. On-time distribution in a CdSe QD coated with a ZnS shell under various physical conditions [8]. Solid lines correspond to calculation by Eq. (14) with $L_{min} = 10^{-2}$ s^{-1}, $L_{max} = 10^3$ s^{-1}, and various $N_{on}(x)$ functions depicted in Fig. 3.

rates L_j covers several orders of magnitude, it is reasonable to take it in the following form:

$$L(j) = L_0 \times 10^{-j}. \tag{12}$$

To clarify the physical meaning of variable j, the following change of the integration variable should be made:

$$j = j_1 + a(r_0 - r), \quad j_2 = j_1 + ar_0, \quad L_0 = L_{max} \times 10^{j_1}. \tag{13}$$

After this change, the integral in Eq. (11) takes the following form:

$$w_{on}(t) = \int_0^{r_0} L(r)\exp[-L(r)t]N_{on}(r)dr$$
$$= \int_0^1 L(x)\exp[-L(x)t]N_{on}(x)dx, \tag{14}$$

where $x = r/r_0$ and

$$L(x) = L_{min}(L_{max}/L_{min})^x. \tag{15}$$

Here, $L_{min} = L_0 \times 10^{-j_2}$ and $L_{max} = L_0 \times 10^{-j_1}$.

Let us consider the QD as a sphere of radius r_0 and the variable r as the radial variable of an atom in the QD. Then, Eq. (15) shows that the e–h pairs located at the QD periphery have the highest ionization rate. It is evident that the function N_{on} taken in the form $N_{on}(x) = 3x^2$ determines the number of atoms in the case of their uniform distribution over the QD. The results calculated by Eq. (14) with the function $N_{on}(x) = 3x^2$ are presented in Fig. 1. If the time period between the shortest ionization time $1/L_{max}$ and the longest time $1/L_{min}$ is larger than the time period studied experimentally,
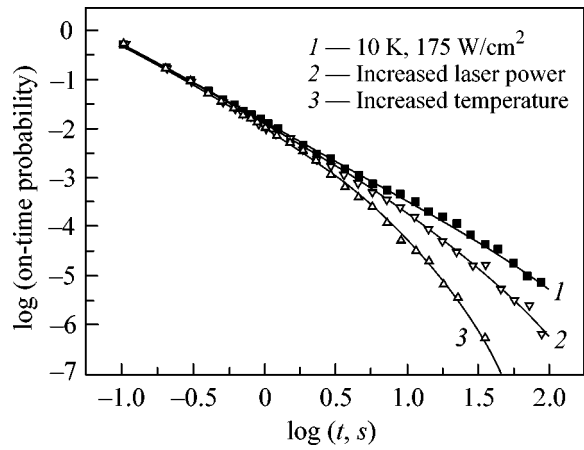
then, as triangles show, Eq. (14) gives a result close to the power-law behavior $t^{-1.5}$. If this condition is not fulfilled, then, as squares show, a deviation from the power law appears.

The experimental data for the on-time distribution of the fluorescence of a CdSe nanocrystal coated with a ZnS shell [8] are presented in Fig. 2. The probability distribution displayed in Fig. 3 was used in the calculation. It follows from the data presented in Fig. 2 that, even though the on-time distribution is close to the power law $t^{-1.5}$, it substantially depends on the excitation intensity and temperature. From the data in Figs. 2 and 3, it also follows that satisfactory agreement with the experiment can be achieved under the suggestion that the density of the e–h pairs generated by light and
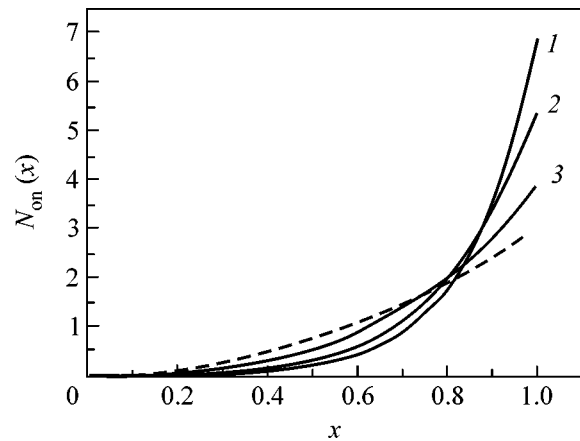

Fig. 3. Distribution of the light-excited atoms in the QD used in the calculation of curves *1*, *2*, and *3* in Fig. 2. The dashed line is the $3x^2$ distribution function corresponding to a uniform density.

participating in the ionization process is higher at the QD periphery. This is demonstrated by a comparison of curves *1*, *2*, and *3* with the dashed curve in Fig. 3.

The temperature dependence of the on-time distribution most likely indicates that the Auger ionization mechanism is not the only one. Considerations in favor of the thermal ionization were presented in [6]. It is conceivable that both mechanisms are efficient in a real nanocrystal. Analysis of the kinetic equations for a nanocrystal with the thermal-ionization mechanism shows that this mechanism also leads to Eqs. (7) and (10). However, the ionization rate constant L_j will then depend on temperature.

It is evident that Eq. (10) for the off-time distribution function can be transformed to the following form:

$$w_{\text{off}}(t) = \int_{k_1}^{k_2} \gamma(k) e^{-\gamma(k)t} n(k) dk. \tag{16}$$

Here, $n(k)$ is the density-of-states function normalized to unity. Now, let us find the form of the $\gamma(k)$ and $n(k)$ functions that provides the power-law distribution. It is assumed that the traps are located in the shell material. Because $\gamma(k)$ is the neutralization rate of the kth trap and, according to the experimental data, can vary by several orders of magnitude, it will be taken in the form $\gamma(k) = \gamma_0 e^{-\lambda} = \gamma_0 \times 10^{-k}$; that is, a tunneling character of the QD neutralization will be assumed. The smaller λ, the higher the transparency of the potential barrier separating the trap and the QD. It is evident that $\gamma_{\text{max}} = \gamma_0 \times 10^{-k_1}$ and $\gamma_{\text{min}} = \gamma_0 \times 10^{-k_2}$. The numerical calculation shows that the integration in Eq. (16) with the probability distribution $n(k) = A_m \gamma^m(k)$, where A_m is a normalization constant, will give a power-law distribution

$$w_{\text{off}}(t) \propto t^{-(1+m)} \tag{17}$$

under the condition that the $(1/\gamma_{\text{max}}, 1/\gamma_{\text{min}})$ interval exceeds the time period for which the off-time distribution functions are investigated. Therefore, the power law $t^{-1.5}$ measured in [7, 8] can be found using the following probability distribution: $n(k) = A_{0.5}\gamma^{0.5}(k) \propto$

$10^{-k/2} = e^{-\lambda/2}$. This means that the majority of the traps have a high neutralization rate; that is, they are located near the QD surface. Our model for traps resembles the model considered in [10]. The exponent m in our model is independent of temperature, in agreement with the experiment.

4. Thus, the assumption about the formation of localized e–h pairs in the nanocrystal explains the closeness of the on-time distribution to a power law in the photoluminescence of a CdSe nanocrystal coated with a ZnS shell. The best agreement with the experiment is achieved if one suggests that the light-generated e–h pairs are mainly concentrated at the nanocrystal periphery, whereas the traps are located in the shell material and the majority of the traps are located near the nanocrystal surface.

REFERENCES

1. M. Nirmal, B. O. Dabbousi, M. G. Bawendi, *et al.*, Nature **383**, 802 (1996).
2. Al. L. Efros and M. Rosen, Phys. Rev. Lett. **78**, 1110 (1997).
3. D. van der Bout, Wai-Tak Yip, D. Hu, *et al.*, Science **277**, 1074 (1997).
4. T. Ha, Th. Enderle, D. S. Chemla, *et al.*, Chem. Phys. Lett. **271**, 1 (1997).
5. H. Lu, L. Xun, and X. Xie, Science **282**, 1877 (1998).
6. U. Banin, M. Bruchez, A. P. Alivisatos, *et al.*, J. Chem. Phys. **110**, 1195 (1999).
7. M. Kuno, D. P. Fromm, H. F. Hamann, *et al.*, J. Chem. Phys. **112**, 3117 (2000).
8. K. T. Shimizu, R. G. Neuhauser, C. A. Leatherdale, *et al.*, Phys. Rev. B **63**, 205316 (2001).
9. M. Kuno, D. P. Fromm, H. F. Hamann, *et al.*, J. Chem. Phys. **115**, 1028 (2001).
10. R. Verbek, A. M. van Oijen, and M. Orrit, Phys. Rev. B **66**, 233202 (2002).
11. I. S. Osad'ko, *Selective Spectroscopy of Single Molecules* (Fizmatlit, Moscow, 2000; Springer, Berlin, 2003).

Translated by A. Bagatur'yants

Gyroscopic Quasi-Relativistic Dynamics of Antiferromagnetic Vortex in Domain Boundary of Yttrium Orthoferrite

M. V. Chetkin*, Yu. N. Kurbatova, T. B. Shapaeva, and O. A. Borshchegovskiĭ

Faculty of Physics, Moscow State University, Vorob'evy gory, Moscow, 119899 Russia
*e-mail: chetkin@magn145.phys.msu.su
Received November 19, 2003; in final form, March 25, 2004

It is demonstrated that the quasi-relativistic dynamics of antiferromagnetic vortices in a quasi-relativistic domain boundary of yttrium orthoferrite are caused by the unusually strong gyroscopic force. © *2004 MAIK "Nauka/Interperiodica".*

PACS numbers: 75.60.Ch

The study of the properties of spin vortices in magnetically ordered substances is of obvious interest for understanding the mechanisms of nonlinear dynamics, magnetization, and magnetization reversal.

In our previous works [1–3], we have observed and studied antiferromagnetic vortices (AFVs) moving in a dynamic domain boundary (DB) of yttrium orthoferrite. These vortices were observed by the agency of attendant solitary flexural waves that were detected using the Faraday effect in plates cut perpendicular to their optical axis. The AFV dynamics were studied by the method of real-time two-snap digital ultrahigh-speed photography.

The theory of spin-vortex gyroscopic dynamics in the DBs of ferrimagnets was developed by Sonin *et al.* in [4, 5]. The authors of those works predicted the existence of flexural waves near the vertical Bloch lines in the DBs. The dynamics, results of pair collisions, and soliton-like behavior of spin vortices in the DBs of epitaxial ferrite garnet films were studied experimentally in [6, 7] using the solitary flexural waves accompanying these vortices. The theoretical interpretation of these experimental results was performed in [8, 9] on the basis of numerical solutions to the Slonczewski and Landau–Lifshitz equations. The oscillations of subdomain boundaries in the wide DBs of a ferrite garnet plate with cubic anisotropy were studied experimentally in [10, 11]. The authors of those works assumed that the subdomain boundaries are the Bloch lines in a DB of a width on the order of several microns between two neighboring domains.

The possible existence of antiferromagnetic vortices in the DBs of orthoferrites was theoretically predicted in [12, 13]. However, they were not observed experimentally before our works. We have shown that the dynamics of antiferromagnetic vortices in the DBs of yttrium orthoferrite are quasi-relativistic, with a limiting velocity equal to the velocity of spin waves (20 km/s) at the linear portion of their dispersion curve,

as also are the DB dynamics in an external magnetic field. Therefore, the antiferromagnetic vortex is quasi-relativistic in the quasi-relativistic DB of yttrium orthoferrite. This work reports the experimental results on determining the amplitudes of the attendant solitary flexural waves as functions of their velocity along the DB. The amplitudes of solitary flexural waves accompanying antiferromagnetic vortices proved to be proportional to their velocity along the DB. This result is known for ferrite garnet films, where, however, the spin-vortex velocities do not exceed several tens of meters per second. The result obtained in this work for yttrium orthoferrite confirms the gyroscopic nature of AFV dynamics in the DBs of weak ferromagnets with the Dzyaloshinski interaction.

A two-snap high-speed photograph of a moving DB together with solitary flexural waves moving along it is presented in Fig. 1. The DB moves from top to bottom. Its first position is shown by the transition from light to dark, and the second position is shown by the transition from dark to light. The delay time between two light pulses of a duration of 250 ps is equal to 6 ns.

Two-snap high-speed digital photographs of solitary flexural waves similar to those shown in Fig. 1 make it possible to determine the DB velocity v, the AFV velocity u along the DB, and the total vortex velocity w. The experimental $u(v)$ curve is shown in Fig. 2. It is highly nonlinear and reaches a maximal value $u = 16$ km/s at $v = 12$ km/s, after which the AFV velocity along the DB decreases and asymptotically tends to zero above $v = 20$ km/s. At the maximum and after it, the relationship $u^2 + v^2 = c^2$ is valid for the dependence $u(v)$.

The experimental dependence $w(v)$ of the total AFV velocity on the DB velocity is presented in Fig. 3; it is also highly nonlinear. The total vortex velocity increases nonlinearly with v and is saturated at $v = 12$ km/s on a level of 20 km/s, which is equal to the
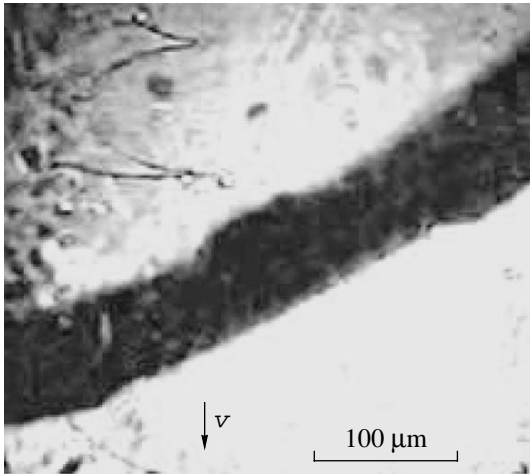
Fig. 1. Two-snap high-speed digital photograph of a dynamic domain boundary with the antiferromagnetic vortices and attendant solitary flexural waves moving along the domain boundary in an yttrium orthoferrite plate cut perpendicular to its optical axis.
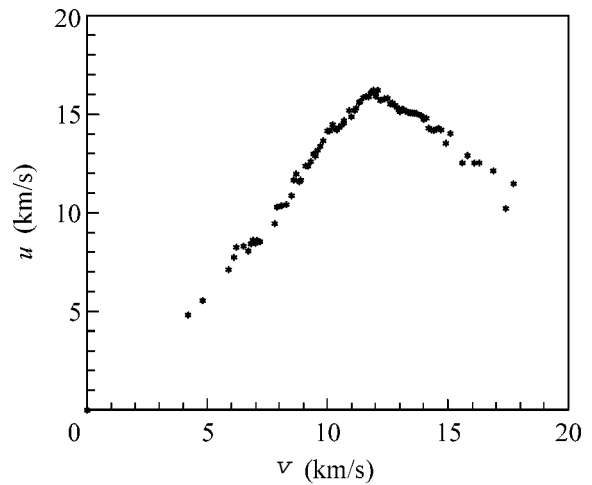

Fig. 2. Dependence of the AFV velocity u along the domain boundary on the DB velocity v in a 40-μm-thick yttrium orthoferrite plate cut perpendicular to its optical axis.
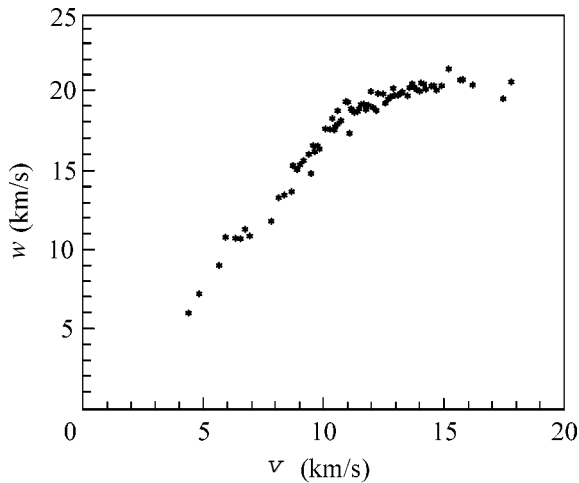

Fig. 3. Dependence of the total AFV velocity w on the DB velocity v.
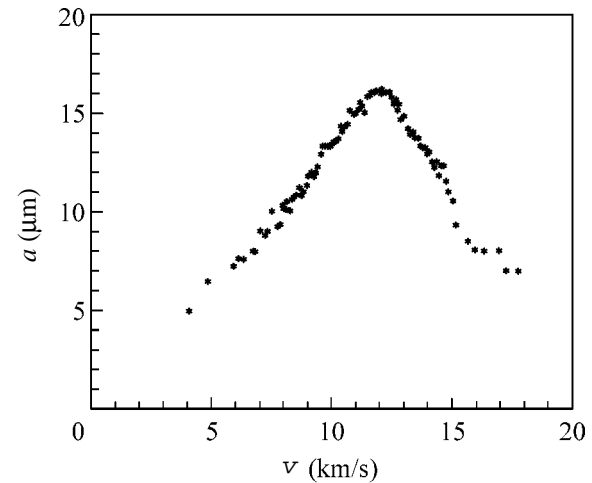
Fig. 4. Dependence of the amplitudes a of solitary flexural waves accompanying antiferromagnetic vortices in a domain boundary of yttrium orthoferrite on the DB velocity v.

velocity of spin waves at the linear portion of their dispersion curve. In the ascending portion of the $u(v)$ curve, the equality $w^2 = u^2 + v^2$ is valid. Thus, the AFV dynamics in the DBs of yttrium orthoferrite are quasi-relativistic with a limiting velocity of 20 km/s equal to the velocity of spin waves at the linear portion of their dispersion curve. Thus, the studied antiferromagnetic vortices are quasi-relativistic in the quasi-relativistic DB.

The dependence of the amplitude a of the attendant solitary flexural wave on the DB velocity is shown in Fig. 4. Like the $u(v)$ dependence in Fig. 2, it is highly nonlinear. The $a(v)$ and $u(v)$ curves are almost the same in the region where u increases to its maximum. Hence, the relation between a and u, as seen in Fig. 5,

is linear and extrapolated almost exactly to zero. After the maximum in the $u(v)$ curve, the situation is qualitatively analogous to the situation described above. The only difference is that the accuracy of determining the amplitudes of solitary flexural waves accompanying antiferromagnetic vortices is slightly lower than in the ascending portion of the $u(v)$ curve. In our opinion, these experimental results confirm the gyroscopic nature of AFV dynamics in a moving DB of yttrium orthoferrite.

The theory of quasi-relativistic DB dynamics in an external magnetic field was developed in [14, 15]. The theory of nonlinear quasi-relativistic AFV dynamics has not been developed as yet. An experiment confirming the gyroscopic nature of AFV dynamics in a mov-
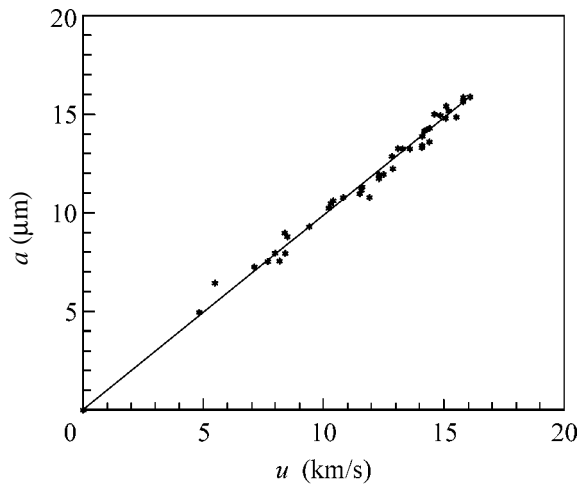
Fig. 5. Dependence of the amplitude a of a solitary flexural wave accompanying antiferromagnetic vortex in a domain boundary of yttrium orthoferrite on the velocity u of the latter along the domain boundary.

ing DB of yttrium orthoferrite is required for constructing such theory.

The existing theory of gyroscopic force is linear with respect to the DB velocity v and is based on the results of works [16–18]. This force is zero in the Lorentz-invariant systems. In a magnetic field H_b directed along the orthoferrite axis b, it is proportional to the magnetic moment m_b along this axis. Under the conditions of our experiment, this force is very small and cannot explain the results of experiment [19]. In addition to the fact that the vector **l** is offset from the ac plane under the action of field H_b, the vectors **l** and **m** in the DB are offset from the ac plane to even a much greater extent. This result was obtained by Bar'yakhtar and Ivanov [20] and Papanicolaou [21]. In the order of magnitude, m_b in this case is comparable with the value of a weak ferromagnetic moment induced by the Dzyaloshinski–Moriya interaction. For a moving DB, the value of m_b was also confirmed by N.A. Usov through the numerical solution to the Landau–Lifshitz equation. However, a contribution of this dynamical sublattice canting to the gyroscopic force has not yet been theoretically calculated.

Our experimental results on the nonlinear gyroscopic quasi-relativistic AFV dynamics in yttrium orthoferrite differ markedly from what is known about the gyroscopic dynamics of Bloch lines in garnets, where the velocity of these lines is proportional to the DB velocity.

In summary, quasi-relativistic AFV dynamics in a quasi-relativistic DB of yttrium orthoferrite are due to the action of a gyroscopic force that has not found any theoretical explanation as yet.

REFERENCES

1. M. V. Chetkin, Yu. N. Kurbatova, and T. B. Shapaeva, Pis'ma Zh. Éksp. Teor. Fiz. **73**, 334 (2001) [JETP Lett. **73**, 294 (2001)].

2. M. V. Chetkin and Yu. N. Kurbatova, Phys. Lett. A **260**, 108 (1999).

3. M. V. Chetkin, Yu. N. Kurbatova, and T. B. Shapaeva, J. Magn. Magn. Mater. **258–259**, 15 (2003).

4. A. V. Nikiforov and E. B. Sonin, Pis'ma Zh. Éksp. Teor. Fiz. **40**, 325 (1984) [JETP Lett. **40**, 1119 (1984)].

5. A. V. Nikiforov and E. B. Sonin, Zh. Éksp. Teor. Fiz. **85**, 642 (1983) [Sov. Phys. JETP **58**, 373 (1983)].

6. M. V. Chetkin, I. V. Parygina, and V. B. Smirnov, Pis'ma Zh. Éksp. Teor. Fiz. **49**, 174 (1989) [JETP Lett. **49**, 204 (1989)].

7. A. V. Balatskii, Pis'ma Zh. Éksp. Teor. Fiz. **49**, 204 (1989) [JETP Lett. **49**, 236 (1989)].

8. M. V. Chetkin, I. V. Parygina, V. G. Roman, and L. L. Savchenko, Zh. Éksp. Teor. Fiz. **105**, 176 (1994) [JETP **78**, 93 (1994)].

9. M. V. Chetkin, L. L. Savchenko, and V. B. Bondarenko, J. Magn. Magn. Mater. **183**, 313 (1998).

10. V. I. Nikitenko, L. M. Dedukh, V. S. Gornakov, and Yu. I. Kabanov, Pis'ma Zh. Éksp. Teor. Fiz. **32**, 152 (1980) [JETP Lett. **32**, 140 (1980)].

11. V. S. Gornakov, L. M. Dedukh, and V. I. Nikitenko, Zh. Éksp. Teor. Fiz. **94** (3), 245 (1988) [Sov. Phys. JETP **67**, 570 (1988)].

12. M. M. Farztdinov, M. A. Shamsutdinov, and A. A. Khalfina, Fiz. Tverd. Tela (Leningrad) **21**, 1522 (1979) [Sov. Phys. Solid State **21**, 878 (1979)].

13. A. P. Malozemoff and J. C. Slonczewski, *Magnetic Domain Walls in Bubble Materials* (Academic, New York, 1979; Mir, Moscow, 1982).

14. A. K. Zvezdin, Pis'ma Zh. Éksp. Teor. Fiz. **29**, 605 (1979) [JETP Lett. **29**, 553 (1979)].

15. V. G. Bar'yakhtar, B. A. Ivanov, and M. V. Chetkin, Usp. Fiz. Nauk **146**, 417 (1985) [Sov. Phys. Usp. **28**, 563 (1985)].

16. A. F. Andreev and V. I. Marchenko, Usp. Fiz. Nauk **130**, 39 (1980) [Sov. Phys. Usp. **23**, 21 (1980)].

17. Yu. V. Melekhov and O. A. Perekhod, Fiz. Tverd. Tela (Leningrad) **26**, 924 (1984) [Sov. Phys. Solid State **26**, 564 (1984)].

18. A. K. Zvezdin, Kratk. Soobshch. Fiz., No. 6, 28 (1999).

19. M. V. Chetkin and Yu. N. Kurbatova, Fiz. Tverd. Tela (St. Petersburg) **43**, 1503 (2001) [Phys. Solid State **43**, 1563 (2001)].

20. V. G. Bar'jakhtar, M. V. Chetkin, B. A. Ivanov, and S. N. Gadetskiy, *Dynamics of Topological Magnetic Solitons, Experiment and Theory* (Springer, Berlin, 1994), Springer Tracts Mod. Phys. **129**.

21. N. Papanicolaou, Phys. Rev. B **55**, 12290 (1997).

Translated by V. Sakun

Cascade of Phase Transitions in GdFe$_3$(BO$_3$)$_4$[¶]

R. Z. Levitin[†, 1], E. A. Popova[1], R. M. Chtsherbov[1], A. N. Vasiliev[1], M. N. Popova[2, *],
E. P. Chukalina[2], S. A. Klimin[2, 3], P. H. M. van Loosdrecht[3],
D. Fausti[3], and L. N. Bezmaternykh[4]

[1] *Faculty of Physics, Moscow State University, Moscow, 119992 Russia*
[2] *Institute of Spectroscopy, Russian Academy of Sciences, Troitsk, Moscow region, 142190 Russia*
* e-mail: popova@isan.troitsk.ru
[3] *Material Science Center, University of Groningen, 9747 AG Groningen, The Netherlands*
[4] *Kirensky Institute of Physics, Siberian Division, Russian Academy of Sciences, Krasnoyarsk, 660036 Russia*
Received March 29, 2004

Cascade of phase transitions in GdFe$_3$(BO$_3$)$_4$ at 156, 37, and 9 K has been detected by specific heat measurements and further studied by Raman scattering and Nd^{3+} spectroscopic probe method. A weakly first-order structural phase transition at 156 K is followed by a second-order antiferromagnetic ordering phase transition at 37 K and a first-order spin-reorientational phase transition at 9 K. © 2004 MAIK "Nauka/Interperiodica".

PACS numbers: 65.40.Ba; 71.70.Gm; 75.30.Et; 75.40.Cx; 78.30.Hv; 75.30.Kz

Borates with general formula RM$_3$(BO$_3$)$_4$, where R stands for a rare earth or yttrium and M = Al, Ga, Fe, or Sc, have attracted considerable attention because of their good luminescent and nonlinear optical properties combined with excellent physical and chemical characteristics. Crystals of YAl$_3$(BO$_3$)$_4$ and GdAl$_3$(BO$_3$)$_4$ doped with neodymium are used for self-frequency doubling and self-frequency summing lasers [1–3]. Concentrated NdAl$_3$(BO$_3$)$_4$ crystals are efficient media for minilasers [3].

Rare earth ferroborates are the least studied compounds of the RM$_3$(BO$_3$)$_4$ family. At room temperature, GdFe$_3$(BO$_3$)$_4$ crystals have the trigonal structure with the space group D_3^7 (R32 [4]). FeO$_6$ octahedra linked together by their edges form spiral chains running along the c axis. Gd^{3+} ions reside in D_3 symmetry positions situated between three such chains and link the chains together. GdO$_6$ prisms are isolated from each other, having no oxygen atoms in common. Each oxygen atom at a vertex of the GdO$_6$ prism belongs also to a BO$_3$ triangle. An indication of a structural phase transition at 174 K has been found recently by specific heat measurements on a powder sample [5].

Measurements of the magnetic properties of GdFe$_3$(BO$_3$)$_4$ were performed in [5, 6], and an anomalous behavior of magnetization was detected at about 40 and 10 K. In the present communication, we report on the temperature-dependent specific heat, Raman, and optical absorption measurements on GdFe$_3$(BO$_3$)$_4$

single crystals, pure or doped with 1 at. % of Nd introduced as a spectroscopic probe.

Crystals of GdFe$_3$(BO$_3$)$_4$ and Nd$_{0.01}$Gd$_{0.99}$Fe$_3$(BO$_3$)$_4$ were grown using a K$_2$Mo$_3$O$_{10}$-based flux, as described in [6]. Big transparent single crystals of ferroborates were green in color and had a good optical quality. Thin plates 5–10 mm in size with different thickness (between 2.2 mm and 150 µm) were prepared for optical measurements. Specific heat in the range 5–300 K was measured by a "Termis" relaxation-type microcalorimeter. Raman measurements were made on a Jobin-Yvon T64000 spectrometer with nitrogen-cooled CCD camera in backscattering geometry. The scattering was excited by the second harmonic of a Nd:YAG laser at 532 nm, with a typical power of 10 mW. The sample was attached by silver paste to a cold finger of an Oxford Instruments helium flow cryostat "Microstat." Optical absorption spectra in the spectral region 4000–20000 cm^{-1} at a resolution of 0.2 cm^{-1} were registered by a Fourier-transform spectrometer BOMEM DA3.002 with InSb liquid nitrogen cooled detector and Si detector at sample temperatures between 4.2 and 300 K.

The temperature dependence of the specific heat of GdFe$_3$(BO$_3$)$_4$ is shown in Fig. 1. Three distinct peaks are seen in this dependence. Two of them, namely, at 9 and 156 K, are very narrow and almost symmetric, while that at 37 K is much broader and asymmetric.

The (zx) polarized Raman spectra of GdFe$_3$(BO$_3$)$_4$ are shown in Fig. 2. At about T_c = 156 K, several new vibrational modes appear, abruptly manifesting a structural phase transition into a less symmetric phase. The

---

[†] Deceased.
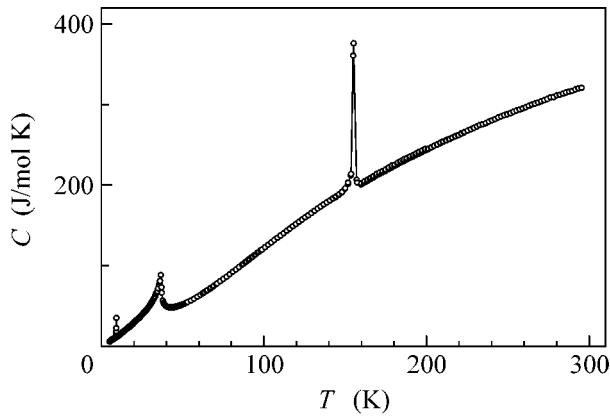[¶] This article was submitted by the authors in English.
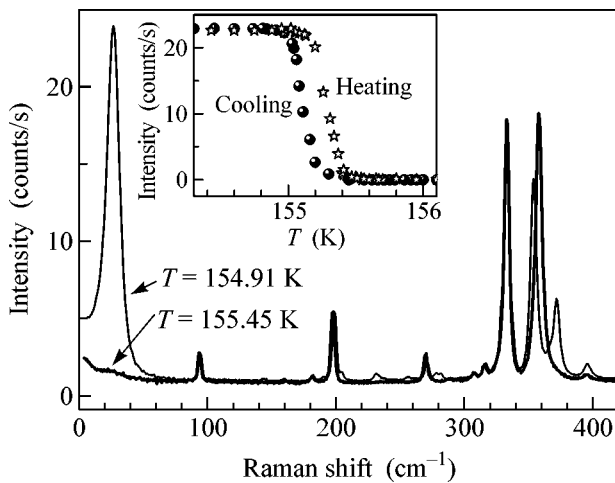
Fig. 1. Specific heat of $GdFe_3(BO_3)_4$ vs. temperature.

Fig. 2. Raman spectra of $GdFe_3(BO_3)_4$ above and below the temperature of a structural phase transition $T_c = 156$ K. Inset shows the temperature dependence of the intensity of the lowest-frequency new mode when cooling (balls) and heating (stars).
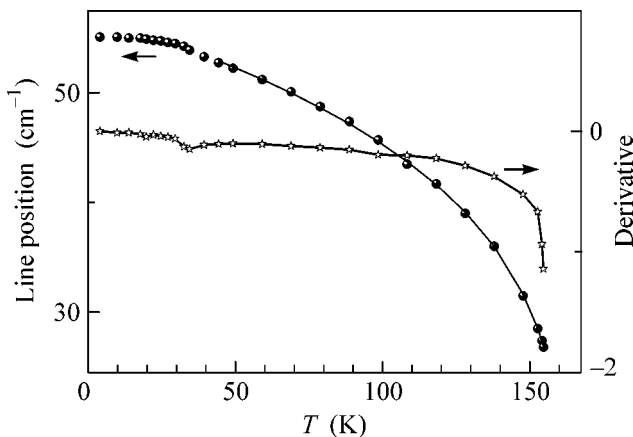

Fig. 3. Temperature dependence of the frequency of the lowest new Raman mode that appears in $GdFe_3(BO_3)_4$ below $T_c = 156$ K.

small difference in T_c determined from specific heat and Raman measurements is due to a heating of the sample by light that excites Raman scattering. The inset to Fig. 2 illustrates the hysteretic temperature dependence of the intensity of the lowest-frequency new mode. All the modes shift with decreasing temperature, typically 1–2 cm^{-1} in the range of temperatures between T_c and 2.5 K. The lowest-frequency new mode demonstrates an unusually big shift. Its frequency changes from 26 cm^{-1} at T_c to 55 cm^{-1} at 2.5 K and has a peculiarity at 37 K (see Fig. 3).

To further study the observed phase transitions, we used the Nd^{3+} ion introduced as a spectroscopic probe. An energy level of the Nd^{3+} ion with the total momentum J is split into $(J + 1/2)$ Kramers doublets by a crystal field of any symmetry lower than a cubic one. Nd^{3+} substitutes for Gd^{3+} in the lattice of $GdFe_3(BO_3)_4$. The number of lines in the spectra of $GdFe_3(BO_3)_4{:}Nd(1\%)$ corresponds to only one position for a rare earth, both above and below the temperature 156 K of the structural phase transition. For example, for T > 40 K, there are two spectral lines due to the optical transitions from the ground state to the crystal-field sublevels of the $^4F_{3/2}$ level. Figure 4 shows the lowest frequency of these two lines at different temperatures. The growing splitting of the line below 37 K is due to the splitting of Nd^{3+} Kramers doublets caused by an internal magnetic field that appears at the sites of the Nd^{3+} ions in a magnetically ordered state of $GdFe_3(BO_3)_4$. Maximum four lines should appear at an optical transition between two split Kramers doublets, and these are clearly seen at low temperatures. Two low-frequency ones freeze out with a further decrease in temperature due to an emptying of the upper component of the split ground Kramers doublet of Nd^{3+}. Figure 5 displays the temperature dependence of the line splitting and of the relative intensities of two high-frequency components of the split spectral line. Sharp changes of these two quantities are observed between 9.5 and 8 K.

Each of the three phase transitions observed in $GdFe_3(BO_3)_4$ is of a different nature. A very strong narrow peak in the temperature dependence of specific heat and an abrupt appearance of new Raman modes exhibiting hysteretic behavior with a narrow hysteresis loop and a strong hardening of one mode with a further decrease in the temperature evidence a weak first-order structural phase transition at about 156 K.

Specific heat in $GdFe_3(BO_3)_4$ and Nd^{3+} spectral probe data in $Nd_{0.01}Gd_{0.99}Fe_3(BO_3)_4$ suggest a second-order magnetic ordering phase transition at about 37 K. Through the magnetoelastic interaction, the magnetic ordering also affects Raman modes and manifests itself as an aforementioned peculiarity in the shifts of these modes. Judging from the temperature dependences of magnetization given in [6], one can state that the antiferromagnetic ordering takes place at 37 K. It seems, however, that this ordering does not affect the rare earth

subsystem much, which remains paramagnetic down to lowest temperatures. In particular, this follows from the fact that the hyperbolic increase of magnetic susceptibility survives below the Neél temperature [6]. The value of magnetic entropy released at this transition, $S_{magn}^{expt} = 37$ J/(mol K), is close to that estimated for Fe^{3+} ($s = 5/2$) subsystem ordering only ($S_{magn}^{theor} = 44$ J/(mol K)). Taking into account that the Fe^{3+} subsystem in $GdFe_3(BO_3)_4$ is of a reduced dimensionality, it is possible to assume that some part of magnetic entropy is released above the Neél temperature.

When a magnetic ordering occurs within a d-metal subsystem, the f-metal subsystem gets polarized due to the f–d exchange. For a rare earth ion, the exchange splittings and, hence, the spectral line splittings are mainly due to the exchange interactions with d ions, while the line width depends on the dipole–dipole interactions with neighboring f ions [7, 8]. In the case of Nd^{3+} probe in $Nd_{0.01}Gd_{0.99}Fe_3(BO_3)_4$, the splitting and narrowing of Nd^{3+} spectral lines manifest a magnetic ordering of the Fe subsystem and polarization of the Gd subsystem below 37 K.

At 9 K, a sharp peak in specific heat characteristic of first-order phase transition is seen. The Nd^{3+} probe spectrum changes at this temperature, showing the superposition of high-temperature and low-temperature spectra in a narrow range in the vicinity of 9 K. Such changes are typical for a first-order spin-reorientational phase transition when two different magnetic phases coexist in a narrow range of temperatures [8]. The magnetic susceptibility data [6] evidence a sharp increase of the signal at $T < 9$ K in a magnetic field oriented perpendicular to the c axis. At the same time, spin-flop transitions observed below 9 K in a magnetic field parallel to the c axis indicate that the antiferromagnetic sublattices in $GdFe_3(BO_3)_4$ are oriented along the c axis. Therefore, the whole of the experimental data suggest that a spin-reorientational phase transition takes place at 9 K. Above this temperature, the iron magnetic moments are oriented perpendicular to the c axis, while below this temperature, the iron moments are oriented along the c axis. In accordance with this inference, the magnetic susceptibility at $T > 9$ K is almost isotropic, which is typical for an easy-plane antiferromagnet.

In summary, we have registered by specific heat measurements three phase transitions (at 156, 37, and 9 K) in $GdFe_3(BO_3)_4$. We further studied these transitions by Raman and optical absorption measurements. The absorption spectra of the Nd^{3+} ion introduced as a probe into the $GdFe_3(BO_3)_4$ matrix were registered. The transition at 37 K was found to be a second-order magnetic-ordering phase transition. All the remaining transitions are first-order ones. At 156 K, the appearance of new Raman modes manifests a change of the crystal structure to a less symmetric one. The spectra of Nd^{3+} probe evidence a spin-reorientation at 9 K.
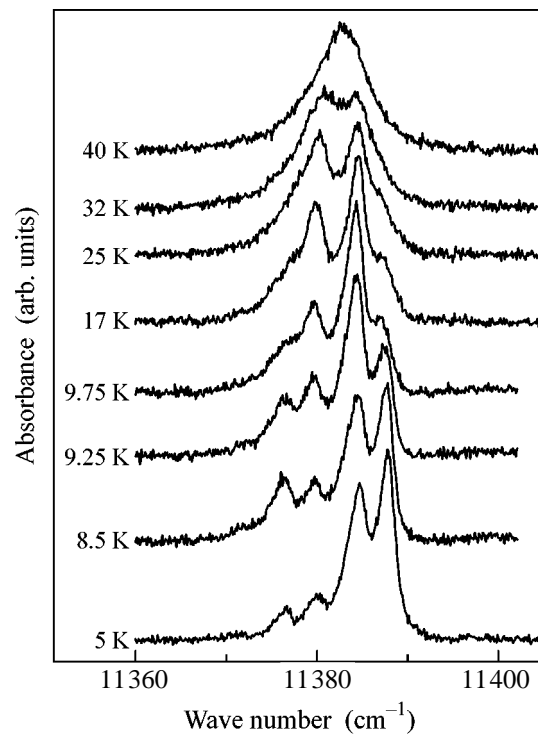

Fig. 4. Spectral line of the Nd^{3+} probe in $GdFe_3(BO_3)_4$ at different temperatures.

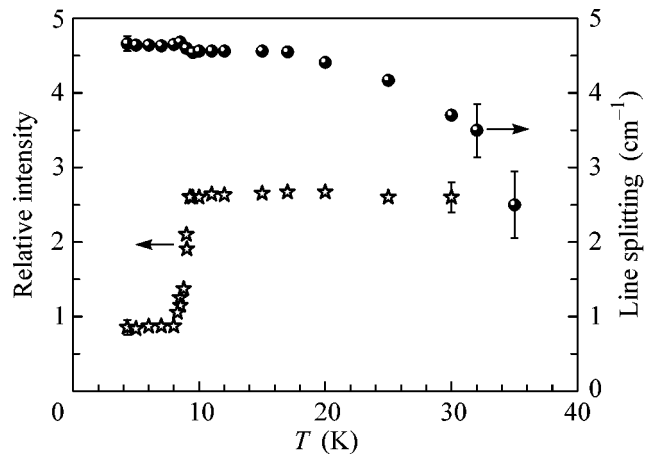**Fig. 5.** Temperature dependences of the line splitting (balls) and relative intensities of the highest-frequency components (stars) for the Nd^{3+} probe in $GdFe_3(BO_3)_4$.

REFERENCES

1. D. Jaque, J. Alloys Compd. **323–324**, 204 (2001).
2. M. Huang, Y. Chen, X. Chen, *et al.*, Opt. Commun. **208**, 163 (2002).
3. X. Chen, Z. Luo, D. Jaque, *et al.*, J. Phys.: Condens. Matter **13**, 1171 (2001).
4. J. A. Campa, C. Cascales, E. Gutierrez-Puebla, *et al.*, Chem. Mater. **9**, 237 (1997).
5. Y. Hinatsu, Y. Doi, K. Ito, *et al.*, J. Solid State Chem. **172**, 438 (2003).
6. D. Balaev, L. N. Bezmaternyh, I. A. Gudim, *et al.*, J. Magn. Magn. Mater. **258–259**, 532 (2003).
7. M. Baran, H. Szymczak, S. A. Klimin, *et al.*, Zh. Éksp. Teor. Fiz. **111**, 318 (1997) [JETP **84**, 175 (1997)].
8. M. N. Popova, J. Alloys Compd. **275–277**, 142 (1998).

Pressure-Induced Tricritical Point and Critical Behavior near the Points of Phase-Diagram Wings in a CoS₂ Ferromagnet

É. Z. Valiev and F. S. Shemet'ev

Institute of Metal Physics, Ural Division, Russian Academy of Sciences,
ul. S. Kovalevskoi 18, Yekaterinburg, 620219 Russia
Received February 5, 2004; in final form, April 1, 2004

A pressure-induced change in the order of magnetic phase transition observed for CoS_2 in [1] is explained using the exchange-striction ferromagnet model allowing for the first- and second-order magnetoelastic interactions. It is shown that this model offers a satisfactory quantitative explanation of the majority of experimental facts observed in CoS_2. The magnetic phase diagram of CoS_2 is calculated in the vicinity of a tricritical point in the temperature (T), pressure (P), and magnetic-field (H) variables. The critical behavior of the thermodynamic quantities near the tricritical points of phase-diagram wings is discussed. © 2004 MAIK "Nauka/Interperiodica".

PACS numbers: 75.30.Kz; 75.40.Cx

Goto *et al.* [1] have recently found that the Curie temperature (T_c) of CoS_2 decreases with a buildup of pressure and that the order of magnetic phase transition changes from second to first at $P \geq 0.4$ GPa. The magnetization curves at $P \sim 1$ GPa demonstrate the metamagnetic behavior in a narrow temperature region above T_c. The experimental data obtained in [1] were analyzed using the theory of metamagnetism of collectivized electrons [2, 3]. However, it was pointed out in [4] that some of the experimental data obtained for CoS_2 are inconsistent with this theory. Meanwhile, it is known [5] that the magnetoelastic interaction (MEI) or the strong dependence of exchange integral on distance can be responsible for a change in the order of magnetic phase transition under pressure.

In this work, one of the variants of the exchange-striction ferromagnet model [6] is used for calculating the magnetic phase diagram of CoS_2 under pressure in the presence of an external magnetic field. In [6], the equations of state were obtained for the magnetic and elastic subsystems of a ferromagnet in the mean-field approximation of the Heisenberg model. Contrary to the majority of exchange-striction models, an MEI of the second order in deformation was taken into account. It will be seen in what follows that this interaction is responsible for the magnetic properties of CoS_2 under pressure. The critical behavior of the thermodynamic quantities in the (T, H) plane near the (T_{cr}, H_{cr}) point, where the first-order magnetic phase transition (FOMPT) curve terminates, will also be analyzed.

When calculating the magnetic properties, we will use the equation of state derived in [6] for the magnetic and elastic subsystems of a ferromagnet. These equations have the form

$$m = B_S(x); \quad x = (2\mu sH + 2s^2 Jm)(kT)^{-1}, \quad (1)$$

$$\omega = (ns^2 m^2 \gamma - P)B_m^{-1}; \quad B_m = (B_0 - \varepsilon s^2 m^2 n/3). \quad (2)$$

Here, $B_S(x)$ is the Brillouin function for spin s; m is the reduced magnetization; μ is the Bohr magneton; $\omega = \Delta V/V$ is the relative change in volume V; k is the Boltzmann constant; n is the number of magnetic atoms in unit volume; γ and ε are the first- and second-order MEI constants, respectively; B_0 and B_m are the bulk moduli without regard for the MEI and the constant magnetization, respectively; H is the external magnetic field; and P is the hydrostatic pressure.

Equations (1) and (2) differ from the conventional molecularfield equations for a ferromagnet in that the exchange integral in Eq. (1) depends on the volume strains,

$$J = J_0 + \gamma\omega + \varepsilon\omega^2/6, \quad (3)$$

while Eq. (2) contains the term $\omega(P = 0)$ determining the spontaneous volume magnetostriction. To take account of the influence of MEI on the magnetic properties, one should substitute the expression for volume strains in Eq. (2) into Eq. (3) and the exchange integral in Eq. (3) into equation of magnetic state (1). To construct the magnetic phase diagram, it suffices to retain in Eq. (1) the terms no higher than fifth order in m. By using the high-temperature expansion of the Brillouin function and expanding all magnetization-dependent
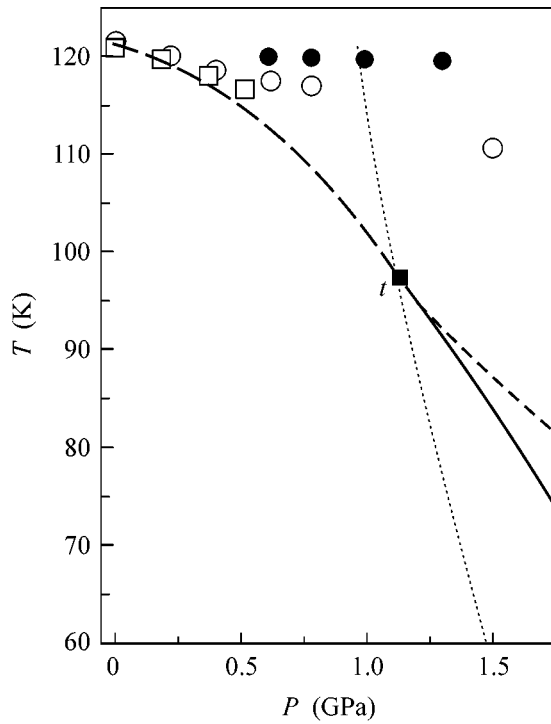
Fig. 1. The magnetic phase diagram of a CoS_2 ferromagnet in the P–T plane. The solid and dashed lines are calculated by the formulas given in the text; the dotted line is calculated for $B = 0$ by formula (5); ($\circ$) and ($\square$) are the experimental data for T_c taken from [1, 4] and [7], respectively. ($\bullet$) Experimental data for the temperature at which the metamagnetic transition disappears [1, 4].

quantities in power series in m, one arrives at the following equation of state:

$$Am + Bm^3 + Cm^5 = h, \qquad (4)$$

where

$$A = (T - T_c(P))/T;$$

$$T_c(p) = T_c^0 - (2kB_0)^{-1}\gamma P + (12kB_0^2)^{-1}\varepsilon P^2; \qquad (5)$$

$$T_c^0 = J_0/2k; \quad h = \mu H/kT,$$

$$B = 1/3(T_c(P)/T)^3 - (8kTB_0)^{-1}n(\gamma^*)^2; \qquad (6)$$

$$\gamma^* = \gamma - \varepsilon P/3B_0,$$

$$C\frac{1}{8}\frac{n}{kTB_0}\left(\frac{T_c(P)}{T}\right)^2\gamma^{*2} - \frac{1}{64}\frac{n^2\varepsilon}{kTB_0^2}\gamma^{*2} - \frac{2}{15}\left(\frac{T_c(P)}{T}\right)^5. \qquad (7)$$

The value $s = 1/2$ in these equations corresponds to the cobalt magnetic moment $\mu_{Co} \approx 1\,\mu$. It is also known that $T_c^0 = 121$ K, $B_0 = 1.5 \times 10^{12}$ erg/cm^3, and $n = 2.4 \times 10^{22}$ cm^{-3} for CoS_2 [1, 4]. One can see from Eqs. (5)–(7) that, to calculate the magnetic phase diagram, the knowledge of the numerical values of the constants γ

and ε is required. The constant γ can be estimated from Eqs. (2) and (5) using the experimentally determined [4] value $\omega(P = 0) \approx (3-6) \times 10^{-4}$ or from the value $\partial T_c/\partial P = -(2kB_0)^{-1}\gamma \approx (5-9)$ K/GPa measured in [4, 7]. Both these estimates are consistent with the value $\gamma = 2 \times 10^{-13}$ erg used in our numerical calculations. It is known [8] that the phase-transition order changes from second to first when the coefficient B in Eq. (3) becomes negative. The estimates by Eq. (6) indicate that $B > 0$ at $\gamma = 2 \times 10^{-13}$ erg, so that the second-order phase transition (SOPT) should occur, as is observed for CoS_2 at the normal pressure. The coefficient B turns to zero at $P \approx 20$ GPa if $\varepsilon = 0$. For this reason, to explain the experimental data for CoS_2, one should assume that $\varepsilon \neq 0$. This is also evidenced by a strongly nonlinear pressure dependence of T_c in CoS_2, which, as is seen from Eq. (5), is due to the term with $\varepsilon \neq 0$. In what follows, we take $\gamma = 2 \times 10^{-13}$ erg and $\varepsilon = -5 \times 10^{-10}$ erg. The value $\varepsilon = -5 \times 10^{-10}$ erg is chosen to obtain a value of about 1 GPa for the pressure at the tricritical point ($A = 0$, $B = 0$), as occurs in the experiment with CoS_2. Interestingly, the same signs and a similar relation between the absolute values of γ and ε were determined in [6] from the experimental data for iron–nickel and iron–platinum invars.

Equations (4)–(7) allow one to quantitatively calculate the magnetic phase diagram in the T, P, H variables and compare it with the experiment. A fragment of this diagram is shown in Fig. 1 for $H = 0$. The second-order phase-transition curve (dashes) is determined from the expression $A = 0$ ($B > 0$). The tricritical point t at $P_t = 1.16$ GPa and $T_t = 97$ K is determined from the equations $A = 0$ and $B = 0$ (dotted curve in Fig. 1), and the solid line corresponding to the FOMPT is found from the equation $A = 3(B^2/C)/16$ ($B < 0$). The short dashes in Fig. 1 correspond to the equation $A = 9(B^2/C)/20$. As will be seen below, this curve is the projection of the line of critical points onto the $H = 0$ plane. The two latter curves bound the region in the (T, P) plane where the FOMPTs (i.e., metamagnetic behavior) are possible at $H \neq 0$. The experimental data shown for CoS_2 in this figure agree satisfactorily with the calculation. The calculated P_t pressure is higher and the pressure dependence of T_c is steeper than in the experiment. In this connection, it is pertinent to note the following. In [1, 4] and review [3], the point where the MPT in CoS_2 changes its order was not considered as tricritical and the characteristic behavior of the thermodynamic quantities in its vicinity was not taken into account when determining its position. As a result, the coordinates of this point were determined in [1, 4] only approximately. Moreover, the Curie points in the FOMPT region were obtained in [1, 4] by extrapolating the $H_c(T)$ dependence of the critical magnetic field to its zero value $H_c(T_c) = 0$ (these data are shown in Fig. 1), whereas, when determining T_c from the ac susceptibility data, the $T_c(P)$ curve becomes steeper, as is demonstrated also by

our calculation. Hence, if the experimental data are revised in the light of the results of our work, then it may well be that our calculation will give a better quantitative agreement with the experiment. Note also that, in addition to the aforementioned agreement of the experimental data with the calculated volume magnetostriction and $T_c(P)$ dependence at low pressures, the agreement with the experiment is observed for the values of critical magnetic field and pressure dependence of magnetization. For instance, at a pressure of 1.3 GPa and temperature $T_c + 1$ K, the observed FOMPT-inducing magnetic field is $H_c \approx 0.2$ T [4]. The corresponding calculation by formula (1) gives the same value for the magnetic field. For the logarithmic derivative of magnetization $\partial \ln M / \partial P$ at low temperatures, one has from [4] a value of 9.3×10^{-3} GPa^{-1}, while calculation by formula (1) yields a value of 6×10^{-3} GPa^{-1} at $P = 0.5$ GPa and $T = 10$ K. Nevertheless, the experimentally measured temperature dependence of bulk modulus should play the decisive role in the verification of the feasibility of our calculations for the explanation of the CoS$_2$ properties. According to formula (2) for B_m and the adopted numerical values of ε, the bulk modulus of CoS$_2$ must markedly (by approximately a factor of 1.5) increase upon the transition from the paramagnetic to ferromagnetic state.

In [9], Griffits defined the tricritical point as a point at which three SOPT lines converge. Two SOPT lines bounding the FOPT surface at $H \neq 0$ and $B < 0$ have come to be known as critical points of phase-diagram wings. Using Eqs. (4)–(7) and the expression for the thermodynamic potential corresponding to equation of magnetic state (4), one can find (see, e.g., [10, 11]) the critical values of parameters at $A > 0$, $B < 0$, and $C > 0$

$$A_{cr} = (9/20)(B^2/C); \quad m_{cr}^2 = -(3/10)(B/C);$$
$$h_{cr} = (6/25)(B^2/C)m_{cr}, \tag{8}$$

which determine two lines of critical points bounding the first-order phase-transition surface. The equilibrium phase diagram in the vicinity of the tricritical point t of a ferromagnet is shown in Fig. 2 in the variables T, P, H. It was calculated using Eqs. (4)–(8). Three SOPT lines (dashes) converge at the point t. The heavy solid lines are the FOPT lines for $P = $ const (lines of the DF type) and $H = 0$ (tD curve). These curves were obtained on the condition that the thermodynamic potentials of the ferromagnetic and paramagnetic phases are equal to each other. The projections of the FOPT surface onto the coordinate planes are shown. The shapes of the phase-diagram wings can be judged from the last equation of Eqs. (8). According to this equation, $h_{cr} \sim B^{5/2}$, while the calculations show that the coefficient B (Fig. 1) can be approximated by a straight line near the tricritical point in the (P, T) plane. For this reason, the wing projection onto the $P = $ const plane is a parabola $h_{cr} \sim (T - T_t)^{5/2}$.
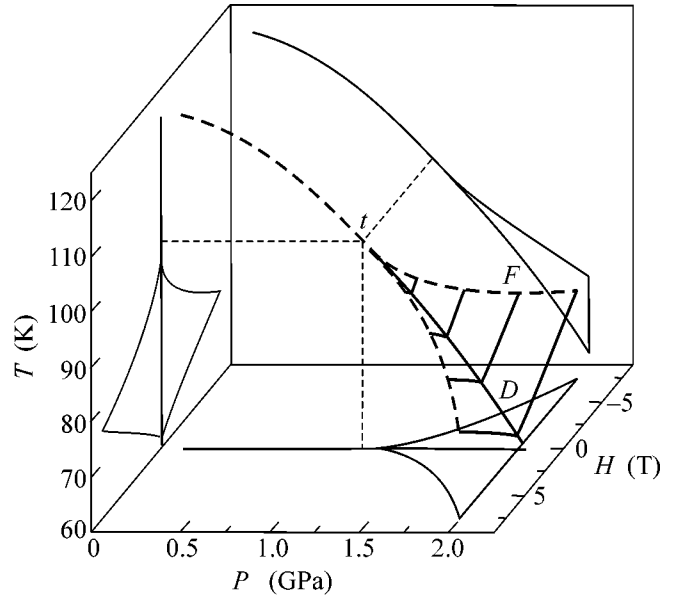

Fig. 2. The equilibrium magnetic phase diagram of a CoS$_2$ ferromagnet in the P, T, H coordinates. Dashes are the SOPT curves. The solid lines denote the FOMPT surface; the lines of the FD type are calculated for $P = $ const and the tD line is calculated for $H = 0$. The fine lines in the coordinate planes are the projections of the FOMPT surface and the SOPT curve.

Let us consider the behavior of thermodynamic quantities in the vicinity of the (T_{cr}, h_{cr}) point. In the variables $\tilde{m} = m/m_{cr}$, $\tilde{A} = A/A_{cr}$, and $\tilde{h} = h/h_{cr}$, equation of state (3) can be written as

$$15\tilde{A}\tilde{m} - 10\tilde{m}^3 + 3\tilde{m}^5 = 8\tilde{h}. \tag{9}$$

To analyze the equation of state in the vicinity of the critical point, we introduce the notation $\eta = (m - m_{cr})/m_{cr}$, $h^* = (h - h_{cr})/h_{cr}$, and $t = (T - T_{cr})/T_{cr}$, with which Eq. (9) takes the following form after omitting the higher powers of t and η:

$$15\alpha t + 15\alpha t\eta + 20\eta^3 = 8h^*; \quad \alpha = (T_{cr} - T_c)/T_{cr}. \tag{10}$$

This equation coincides with the equation of state for a liquid–gas system near the critical point after replacing m by the particle number density and h by the pressure (see [8], Section 152, p. 551). Thus, the FOMPT curve in a magnetic field terminates at the (T_{cr}, h_{cr}) point ($P = $ const). All conclusions about the behavior of paramagnetic and ferromagnetic phases near this critical point can be found in [8]. The critical point of a ferroelectric in an electric field is the electrical analogue of the liquid–gas critical point [11, 12].

Equation (10) does not contain any unknown coefficients and can be used for the quantitative estimates. For example, it follows from Eqs. (10) and (8) that, for $P = 1.4$ GPa, one has $T_c = 87.7$ K, $T_{cr} = 89.4$ K, $H_{cr} = 0.34$ T, and $m_{cr} = 0.26$ and that the latent heat of phase

transition $q = T(\partial H/\partial T)(M_1 - M_2)$, where $M_{1,2} = 2\mu snm_{1,2}$ are, respectively, the magnetizations of the ferromagnetic and paramagnetic phases on the phase-equilibrium curve, turns to zero at T_{cr} following the law $q = 2.4 \times 10^8(-t)^{1/2}$ erg/cm^3 = $5.8(-t)^{1/2}$ cal/cm^3.

To our knowledge, the critical phenomena in the vicinity of the critical points of phase-diagram wings have not been experimentally studied for ferromagnets so far. Experiments of this kind are possible for ferromagnets with the FOMPT at zero pressure. The critical points in a magnetic field can be observed for ferrimagnetic compounds undergoing FOMPTs [13].

REFERENCES

1. T. Goto, Y. Shindo, and H. Takahashi, Phys. Rev. B **56**, 14019 (1997).

2. H. Yamada, Phys. Rev. B **47**, 11211 (1993).

3. H. Yamada, K. Fukamichi, and T. Goto, Physica B (Amsterdam) **237**, 148 (2003).

4. N. V. Mushnikov, T. Goto, A. V. Andreev, *et al.*, Philos. Mag. B **80**, 81 (2000).

5. É. A. Zavadskiĭ and V. I. Val'kov, *Magnetic Phase Transitions* (Naukova Dumka, Kiev, 1980).

6. E. Z. Valiev and A. Z. Menshikov, J. Magn. Magn. Mater. **46**, 199 (1984).

7. K. Sato, K. Adachi, T. Duamoto, *et al.*, J. Phys. Soc. Jpn. **26**, 639 (1969).

8. L. D. Landau and E. M. Lifshitz, *Course of Theoretical Physics*, Vol. 5: *Statistical Physics*, 3rd ed. (Nauka, Moscow, 1976; Pergamon Press, Oxford, 1980), Part 1.

9. R. Griffits, Phys. Rev. B **7**, 545 (1973).

10. Yu. A. Izyumov and V. N. Syromyatnikov, *Phase Transitions and Crystal Symmetry* (Nauka, Moscow, 1984).

11. A. B. Western, A. G. Baker, C. R. Bacon, *et al.*, Phys. Rev. B **17**, 4461 (1978).

12. B. A. Strukov and A. P. Levanyuk, *Physical Principles of Ferroelectric Phenomena in Crystals* (Nauka, Moscow, 1983).

13. É. Z. Valiev, Fiz. Met. Metalloved. **96**, 5 (2003).

Translated by V. Sakun

Transient Response of Photoexcited Electrons
with a Partially Inverted Distribution

F. T. Vasko

Institute of Semiconductor Physics, National Academy of Sciences of Ukraine, Kiev, 03028 Ukraine
e-mail: ftvasko@yahoo.com
Received February 12, 2004; in final form, April 5, 2004

A nonstationary electron magnetotransport is studied for electrons with a partially inverted distribution formed in the passive region after an ultrashort interband photoexcitation and the emission of a cascade of optical phonons. In the case of a peaked distribution in the passive region, the conductivity is positive because of the greater contribution from the decreasing part of the distribution, while the inverted part of the distribution may give rise to a negative magnetoresistance in classical fields. If the energy of photoexcited electrons in the *c* zone is a multiple of the optical phonon energy, a pair of half-peaks occurs at the boundaries of the passive region. In this case, the contribution from the inverted part of the distribution (with an energy close to the phonon energy) leads to a total negative conductance and a considerable change in the magnetotransport. © *2004 MAIK "Nauka/Interperiodica".*

PACS numbers: 72.20.My; 72.40.+w

1. The problem of total negative photoconductance had been discussed as early as in the 1960s [1, 2]. To our knowledge, this effect cannot be observed with a stationary photoexcitation, neither in bulk materials [3] nor in heterostructures. Presumably, this fact is associated with the slowness of the interband recombination, which leads to the accumulation of low-energy electrons, and with the effective Coulomb scattering of high-energy electrons by the low-energy ones [4]. The situation is different in the case of an ultrafast interband photoexcitation, where the recombination affects the transient response only at long times while the electron–electron scattering is ineffective at a low excitation level. Despite the rapid development of high-time-resolution spectroscopy in the last few decades [5], the characteristic features of the transient photoconductivity and nonequilibrium electron magnetotransport in the passive region have been poorly investigated.

The nonstationary magnetotransport of photoexcited electrons with the distribution function $f_{\varepsilon t}$ in a probe field **E** of frequency ω ($\mathbf{E}\exp(-i\omega t) \perp \boldsymbol{\omega}_c$, where $\boldsymbol{\omega}_c$ is the cyclotron frequency) is determined by the diagonal and off-diagonal components of the conductivity tensor, σ_d and $\sigma_\perp$. The latter are determined by the formula

$$\left|\begin{matrix}\sigma_d\\\sigma_\perp\end{matrix}\right| = \frac{2e^2}{lm}\int_0^\infty \frac{d\varepsilon\rho(\varepsilon)\varepsilon}{(\nu_\varepsilon - i\omega)^2 + \omega_c^2}\left|\begin{matrix}\nu_\varepsilon - i\omega\\\omega_c\end{matrix}\right|\left(-\frac{\partial f_{\varepsilon t}}{\partial\varepsilon}\right), \quad (1)$$

where $\rho(\varepsilon)$ is the density of states of electrons in the quantum well or in the bulk ($l = 2$ or 3, respectively) and the momentum relaxation frequency ν_ε takes into account the elastic scattering and the relaxation due to

the spontaneous emission of optical phonons, so that ν_ε drastically increases in the active region $\varepsilon > \hbar\omega_o$. Let us consider the response to a static field ($\omega = 0$) and integrate by parts in Eq. (1). The contribution of the active region to the conductivity is small, and $\sigma_{d,\perp}$ are determined by the elastic scattering in the passive region (the contribution from the integral over $\varepsilon < \hbar\omega_o$) and by the contribution due to the jump in ν_ε at the boundary:

$$\left|\begin{matrix}\sigma_d\\\sigma_\perp\end{matrix}\right| = \frac{2e^2}{lm}\left\{\int_0^{\hbar\omega_0} d\varepsilon\rho(\varepsilon)f_{\varepsilon t}\mathscr{A}_\varepsilon - f_{\varepsilon t}\frac{\rho(\varepsilon)\varepsilon}{\nu_\varepsilon^2 + \omega_c^2}\left|\begin{matrix}\nu_\varepsilon\\\omega_c\end{matrix}\right|_{\varepsilon = \hbar\omega_0}\right\},$$

$$\mathscr{A}_\varepsilon = \frac{l/2}{\nu_\varepsilon^2 + \omega_c^2}\left|\begin{matrix}\nu_\varepsilon\\\omega_c\end{matrix}\right| - \frac{\varepsilon(d\nu_\varepsilon/d\varepsilon)}{(\nu_\varepsilon^2 + \omega_c^2)^2}\left|\begin{matrix}\nu_\varepsilon^2 - \omega_c^2\\2\nu_\varepsilon\omega_c\end{matrix}\right|. \quad (2)$$

Thus, the negative contributions arise in Eq. (2) both because ν_ε increases with energy in the passive region owing to the factor $d\nu_\varepsilon/d\varepsilon$ and from the boundary of the passive region $\varepsilon = \hbar\omega_o$. If the peak is inside the passive region, the contribution from the boundary vanishes and ν_ε increases insufficiently fast for the negative conductivity to occur. However, the magnetic-field dependences change and, owing to the second term in $\mathscr{A}_\varepsilon$, a negative magnetoresistance is observed, its evolution being determined by the quasi-elastic relaxation time due to acoustic phonons. If the electrons are excited near the boundaries of the passive region, a negative conductivity appears owing to the high-energy electrons with an inverted distribution. In this case, the time evolution is determined by both quasi-elastic relaxation and fast emission of optical phonons by the electrons brought into the active region. The character of the
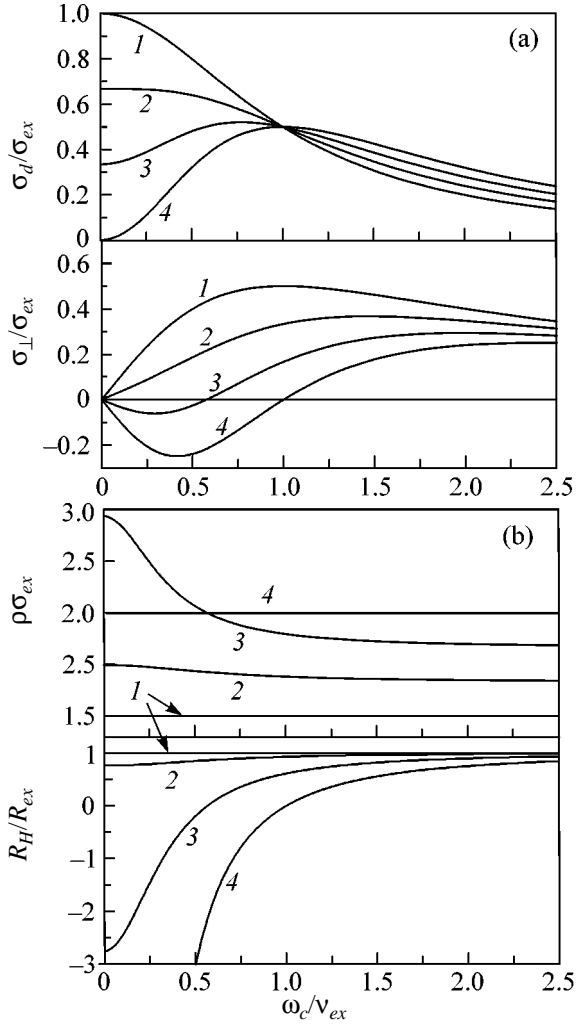
Fig. 1. (a) Modification of magnetic-field dependences of the conductivity tensor components, and (b) the negative magnetoresistance and the Hall coefficient for the parameter $\alpha =$ (*1*) 0, (*2*) 1/3, (*3*) 2/3, and (*4*) 1.

response time evolution is considered below for this case using the narrow-distribution approximation for the photoexcited 2D electrons.

2. We first consider the case of distribution evolution in the passive region, where, due to the emission of a cascade of optical phonons by excited electrons in the region $\varepsilon < \hbar\omega_o$, a peak with width $\Delta\varepsilon$ and the shape described by the function $\delta_{\Delta\varepsilon}(\varepsilon - \varepsilon_{ex})$ appears near the energy ε_{ex}. Assuming that $\Delta\varepsilon \ll \varepsilon_{ex}, \hbar\omega_o - \varepsilon_{ex}$ (narrow-distribution approximation) and using the variable $\xi = \varepsilon - \varepsilon_{ex}$, we consider the peak evolution due to the quasi-elastic scattering by acoustic phonons by using the following equations:

$$\frac{\partial f_{\xi t}}{\partial t} = D\frac{\partial^2 f_{\xi t}}{\partial \xi^2} + v\frac{\partial f_{\xi t}}{\partial \xi},$$

$$f_{\xi t = 0} = \frac{n_{ex}}{\rho_{ex}}\delta_{\Delta\varepsilon}(\xi), \quad f_{\xi \to \pm\infty t} = 0. \quad (3)$$

Here, n_{ex} is the concentration of photoexcited electrons; $\rho_{ex} \equiv \rho(\varepsilon_{ex})$; and the energy diffusion and drift coefficients, D and v, are independent of ξ. Since we limited our consideration to the times within which $f_{\xi t}$ does not reach the boundaries of the passive region, we used above the zero boundary conditions for $\xi \longrightarrow \pm\infty$.

The solution to Eq. (3) has the form

$$f_{\xi t} = e^{-v_{qe}t}\frac{n_{ex}}{\rho_{ex}}\int d\xi' e^{-v(\xi - \xi')/2D}g_t(\xi - \xi')\delta_{\Delta\varepsilon}(\xi'), \quad (4)$$

where we introduced the Green's function $g_t(\Delta\xi) = \exp[-(\Delta\xi)^2/4Dt]/\sqrt{4\pi Dt}$ and the quasi-elastic relaxation frequency $v_{qe} = v^2/4D$; in the case of the scattering by equilibrium phonons, the quantity D/v should be replaced by their temperature. If $\delta_{\Delta\varepsilon}(\xi)$ is a Gaussian function, the integral along the ξ axis can readily be taken to yield a Gaussian distribution, whose shift is determined by the argument $\xi_t = \xi + vt$ and width increases with t as $\Delta\varepsilon_t = \sqrt{\Delta\varepsilon^2 + 4Dt}$:

$$f_{\xi t} = \frac{n_{ex}}{\rho_{ex}}\delta_{\Delta\varepsilon_t}(\xi_t). \quad (5)$$

Substituting Eq. (5) into Eq. (2), we obtain a simple expression for the conductivities $\sigma_{d,\perp}$:

$$\begin{vmatrix}\sigma_d \\ \sigma_\perp\end{vmatrix} = \frac{2e^2 n_{ex}}{lm}\int d\xi\delta_{\Delta\varepsilon_t}(\xi_t)A_\xi, \quad (6)$$

where the column $A_\xi = (\varepsilon_{ex} + \xi)^{l/2}\mathscr{A}_{\varepsilon_{ex+\xi}}$ is introduced.

At zero time, we can use the approximation $\Delta\varepsilon \ll \varepsilon_{ex}$, so that the integral in Eq. (6) is replaced by $A_{\xi = 0}$, which depends on the parameter $\alpha = [(2\varepsilon/lv_\varepsilon)dv_\varepsilon/d\varepsilon]_{\varepsilon_{ex}}$. Figure 1a shows the dimensionless dependences of the conductivities $\sigma_{d,\perp}/\sigma_{ex}$ on the cyclotron frequency ω_c/v_{ex}, where $\sigma_{ex} = e^2 n_{ex}/mv_{ex}$ and $v_{ex} = v_{\varepsilon = \varepsilon_{ex}}$. As α increases, the Lorentzian magnetic-field dependence of σ_d exhibits the ascending portion at $\omega_c/v_{ex} \longrightarrow 0$, while the corresponding dependence of $\sigma_\perp$ exhibits a minimum at small values of ω_c/v_{ex}. The negative magnetoresistance and the Hall coefficient (in units of $R_{ex} = 1/|e|n_{ex}c$) with a strong magnetic-field dependence for $\omega_c/v_{ex} \leq \alpha$ are shown in Fig. 1b. Note that, for $\alpha > 1$, the negative conductivity regime could be realized; however, α is small for 2D electrons and $\alpha = 1/3$ or 2/3 in the case of the scattering of bulk electrons by uniformly distributed phonons or by zero-point oscillations [6]. The boundaries of the passive region do not affect the time evolution if the following conditions are satisfied: $vt < \varepsilon_{ex}$ and $\Delta\varepsilon_t < (\varepsilon_{ex}, \hbar\omega_o - \varepsilon_{ex})$. These conditions can be represented in the form $v_{qe}t < \{v\varepsilon_{ex}/4D, [(\hbar\omega_o - \varepsilon_{ex})/4D]^2\}$, so that the magnetic-field

dependences presented in Fig. 1 take place for times noticeably exceeding v_{qe}^{-1}.

3. Now, let us consider the evolution of a pair of half-peaks excited at the boundaries of the passive region. Such an initial distribution arises as a result of the photoexcitation of electrons with the energy multiple of the optical phonon energy; in this case, after the emission of a phonon cascade, half of the electrons rapidly fall into the low-energy region and their subsequent relaxation is insignificant. To describe the high-energy electrons, we introduce the distribution functions in the passive and active regions, $f_{\xi t}^{<}$ and $f_{\xi t}^{>}$, and take into account the spontaneous emission of optical phonons at $\xi > 0$, which is characterized by the relaxation frequency v_o. Then, for $|\xi| \ll \hbar\omega_o$, we obtain the set of equations

$$\frac{\partial f_{\xi t}^{<}}{\partial t} = D\frac{\partial^2 f_{\xi t}^{<}}{\partial \xi^2} + v\frac{\partial f_{\xi t}^{<}}{\partial \xi}, \quad \xi < 0,$$

$$\frac{\partial f_{\xi t}^{>}}{\partial t} = D\frac{\partial^2 f_{\xi t}^{>}}{\partial \xi^2} + v\frac{\partial f_{\xi t}^{>}}{\partial \xi} - v_o f_{\xi t}^{>}, \quad \xi > 0. \tag{7}$$

At $\xi = 0$, this set is complemented with the continuity conditions for the function $f_{\xi = 0t}^{>} = f_{\xi = 0t}^{<}$ and the derivative $(\partial f_{\xi t}^{<}/\partial\xi)_{\xi = 0} = (\partial f_{\xi t}^{>}/\partial\xi)_{\xi = 0}$. We also use the zero boundary conditions at $\xi \longrightarrow \pm\infty$ and the initial condition of problem (3) with $\varepsilon_{ex} = \hbar\omega_o$.

By introducing the concentrations of high-energy and low-energy electrons, $n_t^{(u)} = \rho_{2D}\int d\xi f_{\xi t}^{<}$ and $n_t^{(l)} = n_{ex} - n_t^{(u)}$, we represent $\sigma_{d,\perp}$ in the form

$$\left|\begin{matrix}\sigma_d \\ \sigma_\perp\end{matrix}\right| = \frac{e^2}{m}\left\{\sum_{j=l,u}\frac{n_t^{(j)}}{v_j}A_j - f_{\xi=0t}^{<}\frac{\rho_{2D}\hbar\omega_o}{v_u^2 + \omega_c^2}\left|\begin{matrix}v_u \\ \omega_c\end{matrix}\right|\right\}, \tag{8}$$

where A_j is given by the column $\mathcal{A}_\varepsilon$ from Eq. (2) at the energies on the order of $\Delta\varepsilon$ for $j = l$ and $\hbar\omega_o$ for $j = u$.

Thus, the response evolution is described by the quantity $f_{\xi=0t}^{<}$, which determines the structure of the transient layer formed due to the competition between the diffusion to the active region and the fast emission of optical phonons, and by the concentrations $n_t^{(l,u)}$ satisfying the condition for the particle number conservation. By integrating Eqs. (7) over the region $\xi < 0$, we obtain the equation for $n_t^{(u)}$:

$$\frac{\partial n_t^{(u)}}{\partial t} = \rho_{2D}\left(D\frac{\partial f_{\xi t}^{<}}{\partial \xi}\bigg|_{\xi=0} + v f_{\xi=0t}^{<}\right) \tag{9}$$

with the initial condition $n_{t=0}^{(u)} = n_{ex}/2$. Then, the components $\sigma_{d,\perp}$ given by Eq. (8) are expressed through $f_{\xi=0t}^{<}$ and its derivative at $\xi = 0$.

Applying the time Laplace transform to Eqs. (7), we obtain a set of equations with constant coefficients for $f_{\xi s}^{<}$ and $f_{\xi s}^{>}$. Its solutions are expressed in terms of the fundamental solutions $\exp(\pm\sqrt{s/D}\,\xi)$ and $\exp(\pm\sqrt{(v_o + s)/D}\,\xi)$ with the aforementioned boundary conditions. After the inverse Laplace transform, we obtain

$$f_{\xi=0t}^{<} = e^{-v_{qe}t}\int_0^t\frac{d\tau}{\tau}\chi_{t-\tau}\int_0^\infty d\xi\,\xi$$

$$\times g_\tau(\xi)(w_\xi e^{-v_o t} + w_{-\xi}), \tag{10}$$

and solution (9) reduces to

$$n_t^{(u)} = \frac{n_{ex}}{2} + \rho_{2D}\int_0^t\frac{d\tau}{\tau}e^{-v_{qe}\tau}\psi_{t-\tau}$$

$$\times \int_0^\infty d\xi\,\xi g_\tau(\xi)(w_\xi e^{-v_o t} - w_{-\xi}). \tag{11}$$

Here, we introduced the function $w_\xi = (n_{ex}/\sqrt{\pi}\rho_{2D}\Delta\varepsilon)\exp[-(\xi/\Delta\varepsilon)^2 + v\xi/2D]$ and used $g_t(\xi)$ from Eq. (4) and the condition $v/\sqrt{Dv_o} \ll 1$.

The functions χ_t and ψ_t in Eqs. (10) and (11) are determined as

$$\chi_t = \frac{1}{2\pi i}\int_{c-i\infty}^{c+i\infty}\frac{ds\,e^{st}}{f(s)},$$

$$\psi_t = \frac{1}{2\pi i}\int_{c-i\infty}^{c+i\infty}\frac{ds\,e^{st}\sqrt{D(v_{qe}+s)}}{sf(v_{qe}+s)}, \tag{12}$$

where $f(s) = \sqrt{D(v_o + s)} + \sqrt{Ds}$. The integrals in Eqs. (12) are expressed through the contributions from the cut along Res between $-\infty$ and $-v_{qe}$, so that Eqs. (10)–(12) yield exact solutions in the narrow-peak approximation.

For the asymptotic behavior at $v_o t \ll 1$ and $v_o t \gg 1$, we obtain the interpolation formulas for Eqs. (12):

$$\chi_t^{-1} \simeq \sqrt{4\pi Dt}(1 + v_o t),$$

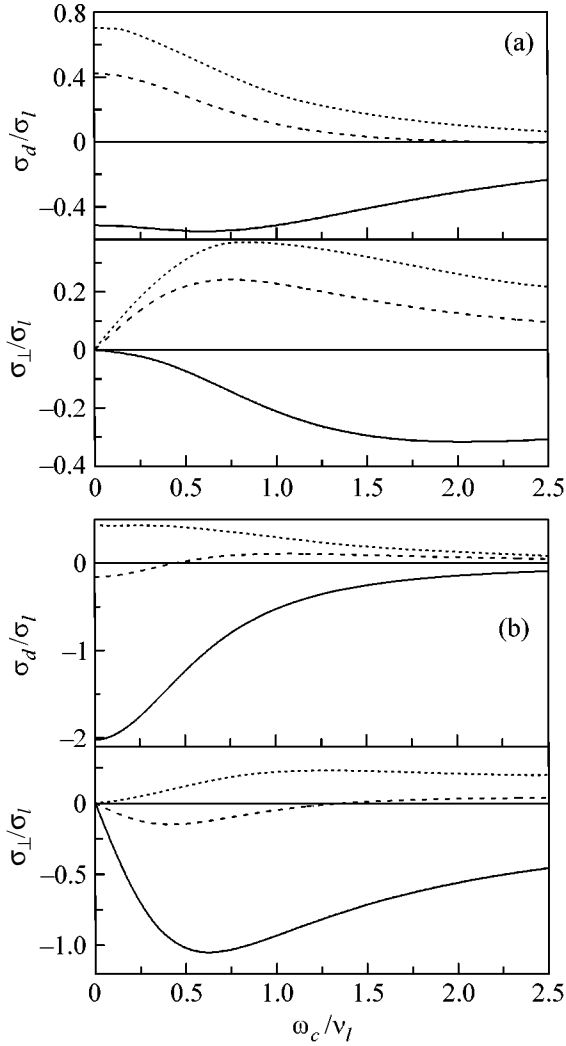$$\psi_t^{-1} \simeq 2 + \sqrt{\pi v_o t}, \tag{13}$$

Fig. 2. Magnetic-field dependences of $\sigma_{d,\perp}$ for $\nu_l/\nu_u =$ (a) 0.7 and (b) 1.4 and for times $t/\tau_u = 0.1$, 0.3, and 0.5 (the solid, dashed, and dotted lines, respectively).

where ψ_t is written for the region $t < \nu_{qe}^{-1}$. Within this time interval, the integrations with respect to ξ and τ in Eqs. (10) and (11) are separated and, on the condition that $\Delta\varepsilon \geq 4D/\nu$, we obtain simple expressions

$$f_{\xi=0t}^< \simeq \frac{w_0}{2\sqrt{\nu_o t}}[1 + (\nu_o t)^{-1}],$$

$$n_t^{(u)} \simeq \frac{n_{ex}}{2} - w_0 \rho_{2D} \sqrt{\frac{D}{\nu_o}}\left[1 - \frac{2\ln(\pi\nu_o t)}{\pi\sqrt{\pi\nu_o t}}\right]. \quad (14)$$

Thus, in the interval $\nu_o^{-1} < t < \nu_{qe}^{-1}$, $f_{\xi=0t}^<$ decreases as an inverse square root of time, while the concentration $n_t^{(u)}$ varies with time only weakly. Taking into account that the parameter α introduced in Fig. 1 is small in the case of 2D electrons and substituting Eqs. (14) into

Eq. (8), we obtain the following equation for the $\sigma_{d,\perp}$ components:

$$\frac{1}{\sigma_l}\left|\begin{matrix}\sigma_d\\\sigma_\perp\end{matrix}\right| = (1 + \Omega_l^2)^{-1}\left|\begin{matrix}1\\\Omega_l\end{matrix}\right| + \frac{\nu_l/\nu_u}{1 + \Omega_u^2}\left|\begin{matrix}1\\\Omega_u\end{matrix}\right|\left(1 - \sqrt{\frac{\tau_u}{t}}\right), \quad (15)$$

where $\Omega_j = \omega_c/\nu_j$ and the conductivity $\sigma_l = e^2 n_{ex}/m\nu_l$ is determined by the mobility of low-energy electrons. To describe the inverse-square-root time dependence of $f_{\xi=0t}^<$, we also introduced the characteristic time $\tau_u = (\hbar\omega_o/\Delta\varepsilon)^2/\pi\nu_o$.

Thus, at $\omega_c = 0$, the negative conductivity regime is realized at times shorter than $\tau_u/(1 + \nu_u/\nu_l)^2$; in this interval, the condition $\nu_{qe}t < 1$ is usually met, so that long times can be ignored. At $\nu_u = \nu_l$, time dependences (15) are described by the factor $(2 - \sqrt{\tau_u/t})$ and the magnetic-field dependences have their usual form. For the case $\nu_u \neq \nu_l$, the dependences are shown in Fig. 2; here, the negative conductivity and the magnetotransport features prove to be more pronounced for $\nu_l > \nu_u$.

4. The above consideration demonstrates that the characteristic features of the transient response of photoexcited electrons with a partially inverted distribution can be observed on the nanosecond time scale. In addition to the negative photoconductivity and magnetoresistance considered above, a negative cyclotron absorption is possible. In the resonance approximation $|\omega - \omega_c| \ll \omega_c$, the conductivity tensor components differ from those given by Eq. (2) in that ω_c is replaced by the frequency deviation $\omega - \omega_c$. In the case of the photoexcitation in the passive region, a dip appears in the middle of the cyclotron peak, while in the case of the excitation near the boundaries of the passive region, a negative absorption occurs at the cyclotron frequency. These features of the transient response were recently revealed upon the photoexcitation of bulk Si and Ge [7]; however, this phenomenon can be quantitatively described only if the characteristic features of photoexcitation and relaxation in multivalley semiconductors are taken into account.

Let us now discuss the approximations used above. Classical formula (1) is suitable for describing the transient response at times exceeding the collision time that is on the order of $\hbar/\Delta\varepsilon$ for slow electrons; i.e., this approach is valid if $\Delta\varepsilon > \hbar\nu_o$. In Eq. (2), only the contributions of the passive region and its boundary are taken into account, because $\nu_{\varepsilon<\hbar\omega_o} \ll \nu_o$ and the $f_{\xi t}$ variation scale at the boundary (exceeding $\sqrt{D/\nu_o}$; see Eq. (7)) is greater than the width (quantum spreading of the step density of states) of the interval in which the optical phonon emission is initiated. The results of Section 2 apply to electrons in both quantum well and bulk, as long as the distribution remains narrower than $\hbar\omega_o$, so that the energy dependences of D and ν are insignificant. The consideration of the time evolution of the

negative photoconductivity in Section 3 is limited to the simpler case of 2D electrons, where the relaxation frequency due to optical phonons is constant. In the bulk case, $\nu_\xi \propto \sqrt{\xi}$ for the deformation mechanism of interaction with optical phonons, so that the conditions for the realization of the transient negative photoconductivity become less stringent. To avoid the photoexcitation nonuniformity in the bulk of direct-gap semiconductors, one can use a two-photon pumping.

In closing, it should be noted that the photoexcitation of electrons in the negative conductivity regime leads to their instability. When analyzing the high-frequency transient response in the negative absorption regime, one may reveal the possibility of realizing the stimulated transient-radiation regime, the frequency interval being limited by only the condition $\omega \ll \omega_o$; i.e., emission in the terahertz spectral band is possible. The analysis of these problems requires special investigation.

REFERENCES

1. H. J. Stocker and H. Kaplan, Phys. Rev. **150**, 619 (1966); H. J. Stocker, Phys. Rev. Lett. **18**, 1197 (1967).

2. V. F. Elesin and É. A. Manykin, Pis'ma Zh. Éksp. Teor. Fiz. **3**, 26 (1966) [JETP Lett. **3**, 15 (1966)]; Zh. Éksp. Teor. Fiz. **50**, 1381 (1966) [Sov. Phys. JETP **23**, 917 (1966)].

3. P. G. Harper, J. W. Hodby, and R. A. Stradling, Rep. Prog. Phys. **36**, 1 (1973).

4. S. É. Esipov and I. B. Levinson, Zh. Éksp. Teor. Fiz. **86**, 1915 (1984) [Sov. Phys. JETP **59**, 1113 (1984)]; Zh. Éksp. Teor. Fiz. **90**, 330 (1986) [Sov. Phys. JETP **63**, 191 (1986)].

5. J. Shah, *Ultrafast Spectroscopy of Semiconductors and Semiconductor Nanostructures* (Springer, New York, 1996).

6. V. F. Gantmakher and I. B. Levinson, *Carrier Scattering in Metals and Semiconductors* (Nauka, Moscow, 1984; North-Holland, Amsterdam, 1987).

7. H. E. Porteanu, O. Loginenko, and F. Koch (in press).

Translated by E. Golyamina

Magnetic Nesting and Coexistence of Ferromagnetism and Superconductivity

V. F. Elesin[1], V. V. Kapaev[2], and Yu. V. Kopaev[2, *]

[1]*Moscow Institute of Engineering Physics (State University), Kashirskoe sh. 31, Moscow, 115409 Russia*
[2]*Lebedev Physical Institute, Russian Academy of Sciences, Leninskiĭ pr. 53, Moscow, 119991 Russia*
*e-mail: kopaev@sci.lebedev.ru

If the condition $\varepsilon_\sigma(\mathbf{p}) = \varepsilon_{-\sigma}(-\mathbf{p} + \mathbf{n}I/v_F)$ for magnetic nesting is fulfilled for the electron dispersion law with spin σ along a certain preferential direction $\mathbf{n}$, ferromagnetism and the inhomogeneous superconducting state can coexist up to a very high magnetization I. This fact was used to explain the coexistence of ferromagnetism and superconductivity for layered cuprates of the $RuSr_2GdCu_2O_8$ type, which possess a finite, though rather high, critical magnetization, because the conditions for magnetic nesting are fulfilled only approximately. © 2004 MAIK "Nauka/Interperiodica".

PACS numbers: 74.25.Ha; 74.81.-g

1. The phenomena of superconductivity and ferromagnetism are seemingly antagonistic with respect to a magnetic field: superconductor expels magnetic field (Meissner–Ochsenfeld effect), whereas ferromagnet, quite the opposite, concentrates it. The problem of the possibility of these states coexisting was studied by Ginzburg [1] in 1956 even prior to the appearance of the microscopic BCS theory [2].

According to [1], this coexistence is possible if the critical magnetic field H_c is higher than the magnetic induction I. From the microscopic point of view [2], the value of H_c in most cases is determined through the influence of a magnetic field (and induction) on the pair orbital motion. In addition, due to the pairing of oppositely directed spins, the Zeeman splitting also quenches superconductivity (paramagnetic effect), and this is precisely the factor that plays the decisive role [3].

If the superconducting transition temperature T_c is much higher than the ferromagnetic transition temperature T_m, the magnetic state in the coexistence region is inhomogeneous [4] (the current theoretical and experimental results are discussed in [5]).

When $T_c \le T_m$, a narrow magnetization (I) interval exists where the superconducting state is inhomogeneous under the coexistence conditions [6, 7].

In recent years, much work has been devoted (see, e.g., [8, 9]) to the observation of the coexistence of ferromagnetism and superconductivity in layered $RuSr_2GdCu_2O_8$ cuprates, in which T_m is appreciably higher than T_c ($T_m = 132$ K and $T_c = 46$ K). Such a ratio between T_m and T_c is intolerable for the simple spherical Fermi surface underlying the model considered in [6, 7]. In contrast to the homogeneous state, which is insensitive to the shape of the Fermi surface [2, 3], the inhomogeneous superconducting state can exist in a wider magnetization interval, provided that the nesting condition is approximately fulfilled [10, 11].

It is shown in this work that the processes of hopping to the centers of the third sphere, which were disregarded in [10, 11], though superior to the second-sphere hopping in cuprates, dramatically change the coexistence situation. It is also shown that the superconducting state with a large total pair momentum [12] can coexist with the ferromagnetic state in the presence of a sufficiently high magnetization.

For certain hopping parameters optimal from the coexistence viewpoint, the condition for magnetic nesting

$$\varepsilon_\sigma(\mathbf{p}) = \varepsilon_{-\sigma}(-\mathbf{p} + \mathbf{n}I/v_F) \qquad (1)$$

can be fulfilled.

The coexistence of ferromagnetism and superconductivity is possible up to a very high magnetization (v_F is the Fermi velocity). Therefore, the orbital mechanism considered in [1] is the main magnetization-induced superconductivity-quenching mechanism in this situation.

2. As a simple model satisfying magnetic-nesting condition (1), we choose a two-dimensional model of electron spectrum with the isoenergetic lines in the form of squares in a certain interval of energies (on the order of the cutoff energy ω of attractive interaction V). Assuming that ω ($\omega = \omega_{ph}$ for the electron–phonon interaction) is small compared to the Fermi energy ε_F, we write the equation for the order parameter Δ ($\Delta(r) =$

$|\Delta|e^{i\mathbf{qr}}$ and $\mathbf{q}$ is the pair momentum) at $T = 0$ in the BCS form

$$\frac{1}{\lambda} = \int_0^\omega \frac{d\xi}{\sqrt{\xi^2 + |\Delta|^2}}\left\{1 - \frac{1}{2}[n(\varepsilon + I + Q)\right.$$
$$\left. + n(\varepsilon + I - Q) + n(\varepsilon - I - Q) + n(\varepsilon - I + Q)]\right\}, \tag{2}$$

where $\varepsilon = \sqrt{\xi^2 + |\Delta|^2}$, $\lambda = VN$, N is the density of states at the Fermi level, $n(\varepsilon) = (e^{\varepsilon/T} + 1)^{-1}$, and $Q = qv_F/2$.

The solution with a certain preferential $\mathbf{q}$ corresponds to the appearance of a homogeneous current state [7]. Below, we formally restrict ourselves to this case, with an eye to summing over all equivalent states of momentum $\mathbf{q}$ [6], as a result of which the homogeneous current disappears.

3. Setting $Q = 0$ in Eq. (2), we obtain the equation for $|\Delta|$:

$$\frac{1}{\lambda} = \int_0^\omega \frac{d\xi}{\sqrt{\xi^2 + |\Delta|^2}}\{1 - n(\varepsilon + I) - n(\varepsilon - I)\}. \tag{3}$$

If $I < \Delta$, the quasiparticle distribution functions $n(\varepsilon + I)$ and $n(\varepsilon - I)$ are zero and the solution to Eq. (3) is $\Delta = \Delta_0$. In the opposite case of $I > \Delta$, one has

$$\Delta = \begin{cases} \Delta_0(2I - \Delta_0) & \text{for } \Delta_0/2 < I < \Delta_0, \\ 0 & \text{at } I > \Delta_0. \end{cases} \tag{4}$$

Hence, the solution to Eq. (3) has two branches. In addition, the trivial solution $\Delta = 0$ corresponding to the normal state always exists.

One can easily show that the solution increasing with I corresponds to a local free-energy maximum, i.e., to the unstable state. The energy difference between the superconducting and normal states is given by the expression

$$U_s - U_n = \frac{N}{2}(2I^2 - \Delta_0^2). \tag{5}$$

Hence, it follows that the solution $\Delta = \Delta_0$ is energetically more favorable for $I < I_c$, where

$$I_c = \Delta_0/\sqrt{2}, \tag{6}$$

after which a first-order phase transition occurs from the superconducting phase $\Delta = \Delta_0$ to the normal phase $\Delta = 0$; i.e., superconductivity is quenched. These results coincide with the results for a system with the isotropic quadratic dispersion law [3].

4. In 1964, it was shown [6, 7] that the superconducting phase in superconductors with the quadratic dispersion law can appear at $I > I_c$, but the corresponding order parameter $\Delta(r)$ is inhomogeneous. The new
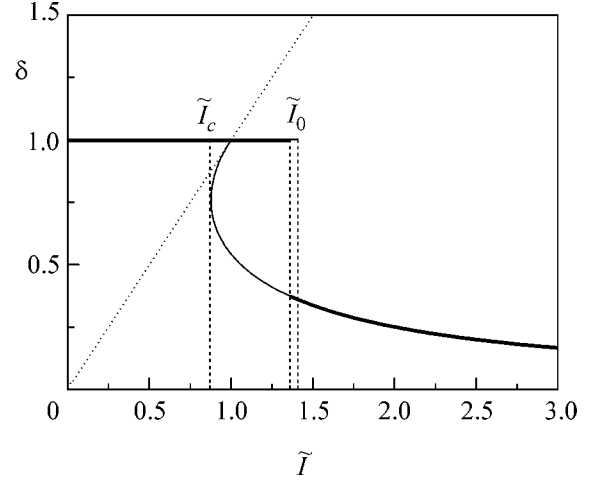

Fig. 1. Dependence of the order parameter δ on the magnetization $\tilde{I}$.

phase (FFLO phase) arises through the first-order phase transition and exists in a narrow field interval

$$0.707 < I/\Delta_0 < 0.754; \quad Q_c = 0.897\Delta_0. \tag{7}$$

Let us consider the inhomogeneous state using Eq. (2). We first analyze the most intriguing case where the I-induced spin splitting in the spectrum is compensated by the condensate momentum satisfying condition (1):

$$I = Q, \quad 2I > \Delta. \tag{8}$$

At temperature $T = 0$, only the terms $n(\varepsilon - I - Q) \equiv n(\varepsilon - 2I)$ are nonzero, and we find from Eq. (2) the equation for $\delta = \Delta/\Delta_0$,

$$\delta(\tilde{I} + \sqrt{\tilde{I}^2 - \delta^2}) = 1, \quad (\tilde{I} = 2I/\Delta_0) \tag{9}$$

or the equivalent equation

$$2\delta\tilde{I} = 1 + \delta^4. \tag{10}$$

One can easily see that Eqs. (9) and (10) have no zero solutions. The dependence of the order parameter δ on the magnetization $\tilde{I}$ is shown in Fig. 1. In the interval $\tilde{I}_c < \tilde{I} < 1$ ($\tilde{I}_c = 2 \times 3^{-3/4} \approx 0.87$, $\tilde{I} > \delta$), this dependence has a two-valued character and becomes single-valued at $\tilde{I} > 1$, where δ decreases monotonically with increasing $\tilde{I}$, though remaining finite.

The existence of the solution for $\Delta \neq 0$ at $\tilde{I} > \delta$ is due to the fact that, under condition (1), the excitation energy for a pair with $Q = I$ turns to zero at the line (instead of points in the case of isotropic dispersion law [6, 7]). A decrease in Δ with increasing I is due to the fact that the line of zeros (line for which the condition $\varepsilon_\sigma(\mathbf{p}) = \varepsilon_{-\sigma}(-\mathbf{p} + \mathbf{n}I/v_F) = 0$ is met) becomes shorter.

The energy difference between the inhomogeneous superconducting state and the normal state can be calculated by the standard method:

$$U_s - U_n = -N\frac{\Delta^3\sqrt{4I^2-\Delta^2}}{2\Delta_0^2} = -\frac{N\Delta_0^2}{2}\delta^3\sqrt{\tilde{I}^2-\delta^2}. \quad (11)$$

It follows from this expression that, at $\tilde{I} > \delta$, the inhomogeneous superconducting state is energetically more favorable than the normal state. However, at $\tilde{I} < \sqrt{2}$, the energy of the inhomogeneous state in Eq. (11) should be compared with the energy of the homogeneous state in Eq. (5). They are equated at $\tilde{I}_0$ and δ_0 values satisfying the system of Eq. (10) together with the equation

$$\delta_0^3\sqrt{\tilde{I}_0^2-\delta_0^2} = 1 - \frac{\tilde{I}_0^2}{2}. \quad (12)$$

Analysis shows that the solution to Eq. (10) at $\delta \leq \delta_0$ and $\tilde{I} > \tilde{I}_0$ can be written, to a good accuracy, as

$$\delta = \frac{1}{2\tilde{I}}, \quad \left(\Delta = \frac{\Delta_0^2}{4I}\right). \quad (13)$$

By using expressions (13) for δ_0 and $\tilde{I}_0$, we obtain from Eq. (12) the approximate equation

$$\tilde{I}_0^4 - 2\tilde{I}_0^2 + \frac{1}{4} = 0, \quad (14)$$

which yields $\tilde{I}_0 = \sqrt{1 + \sqrt{3}/2} \approx 1.36$ and $\delta_0 \approx 0.36$.

Thus, a system with magnetic nesting undergoes at $I > 0.68\Delta_0$ the first-order phase transition from the superconducting state with a homogeneous order parameter $\Delta = \Delta_0$ to the inhomogeneous state with $|\Delta| = 0.36\Delta_0$. As I increases, the order parameter decreases monotonically according to Eq. (13), and energy difference (11) at $\tilde{I} > \sqrt{2}$ is given by the expression

$$U_s - U_n \approx -N\frac{\Delta_0^2}{16\tilde{I}^2}. \quad (15)$$

Note that energy difference (15) also exceeds at $I = \Delta_0$ the corresponding maximal value for the FFLO phase by two orders of magnitude.

We now turn to the situation with $Q > I$ and $Q - I > \Delta$. It is in this interval of parameters that the FFLO phase is realized. Using Eq. (2), we obtain the following equation for Δ:

$$(Q + I + \sqrt{(Q+I)^2 - \Delta^2})$$
$$\times (Q - I + \sqrt{(Q-I)^2 - \Delta^2}) = \Delta_0^2. \quad (16)$$

One can see that, in contrast to Eq. (9), this equation has a solution with $\Delta = 0$. However, analysis of the solutions to Eq. (16) is of no interest, because they are energetically unfavorable. Indeed, the energy difference

$$U_s - U_n = \frac{N\Delta^2}{2}a_+a_-\left[1 - \sqrt{\left(1 - \frac{\Delta^2}{a_+^2}\right)\left(1 - \frac{\Delta^2}{a_-^2}\right)}\right], \quad (17)$$

$$a_\pm = Q \pm I$$

is always positive. This result is evidence that the optimal situation occurs at $Q \leq I$ and $I - Q < \Delta$, where superconductivity is highly stable against the action of the exchange ferromagnetic field up to very large magnetizations.

5. The above calculations were carried out for the idealized situation where the Fermi contour is a square and the spectrum satisfies condition (1). The spectrum of actual HTSC cuprates (including those containing ferromagnetic layers, e.g., $RuSr_2GdCu_2O_8$) can be calculated with a high accuracy using the tight-binding approximation with allowance for three coordination spheres,

$$\varepsilon(k_x, k_y) = 2 - 2t(\cos\pi k_x + \cos\pi k_y)$$
$$- 4t_1t(\cos\pi k_x\cos\pi k_y) - 2t_2t(\cos2\pi k_x + \cos2\pi k_y). \quad (18)$$

The typical literature values of hopping integrals are $t = 0.5$ eV, $t_1 = -0.3$, and the parameter t_2 varies in a rather broad range from 0 to 0.8. Such a choice of the dispersion law allows the explanation of the experimentally observed Fermi-contour shape near half-filling. Since the turn of Fermi contour (compared to the nearest-neighbor approximation) and magnetic nesting (1) are largely determined by the overlap integral t_2 with the third neighbor, the subsequent calculations will be carried out for various values of t_2. In [11], only the second neighbors were taken into account (i.e., $t_2 = 0$) and t_1 was taken to be twice as large as its commonly accepted value to ensure the turn of Fermi contour and bring it closer to a square with rounded corners. It seems to us that, to accomplish this end, such a choice is less realistic than the inclusion of t_2. In this case, the experimentally observed corrugation of the Fermi contour can also be explained. The magnetization shifts dispersion curve (18) for one of the spin directions by a value of I.

Earlier, it was pointed out that the superconducting stability effect is caused by a large length of the $\varepsilon_\sigma(k) = \varepsilon_{-\sigma}(k + q) - I$ line of energy-excitation zeros. In the simplest model considered above, $\varepsilon_\sigma(k)$ perfectly coincides with $\varepsilon_{-\sigma}(k + q) - I$ on a portion of the Fermi-contour, whereas the coincidence is only approximate in the real dispersion law. Nevertheless, the difference between these lines can be small enough on a wide energy interval. Below, we will not assess the effect of field I by solving the self-consistency equation for Δ but restrict
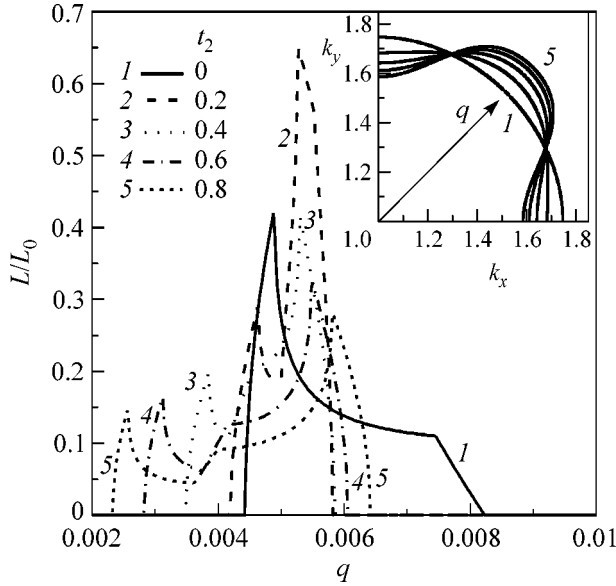
Fig. 2. Plots of the length L on which the magnetic-nesting condition is fulfilled vs. the wave vector q for $I = 0.02$ eV, $\gamma = 0.001$ eV, and various values of parameter t_2. Inset: Fermi-contour shape.
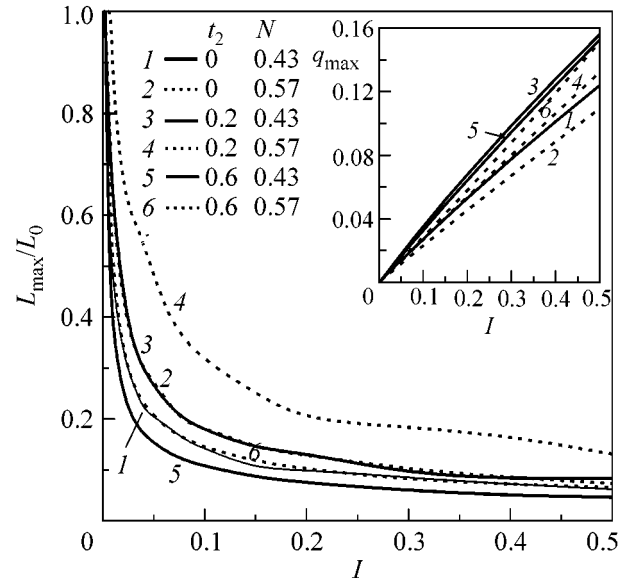

Fig. 3. Plots of length L_{max} vs. magnetic shift I for the (2, 4, 6) electron and (1, 3, 5) hole doping and various values of t_2. Inset: optimal value of the wave vector $q_{max}(I)$.

ourselves to the calculation of the Fermi-contour length L where magnetic-nesting condition (1) is approximately fulfilled with a given accuracy. The algorithm for calculating L is as follows: for a given filling factor n, Eq. (18) is used to determine the Fermi energy, the corresponding isoenergy line (Fermi contour) $k_y = F(k_x)$, and its length L_0. Thereupon the energy $\gamma = |\varepsilon_\sigma(k) - \varepsilon_{-\sigma}(k + q) - I|$ of a particle with the opposite spin is calculated on the Fermi contour with allowance for the magnetic splitting I and wave vector shift q (nonzero pair momentum). The departure from the magnetic-nesting condition will be characterized by the parameter $\gamma = |\varepsilon_\sigma(k) - \varepsilon_{-\sigma}(k + q) - I|$, while the Fermi-contour length L, for which $\gamma < \gamma_0$, where γ_0 is a certain given (small) value, will be used as a final value. Although the value of γ_0 is determined, in principle, by a set of parameters (e.g., by the cutoff parameter), we will be interested only in some general trends that are insensitive to the particular details. Roughly speaking, L/L_0 is the estimate for the expression in braces in self-consistency Eq. (2). It is close to zero in the FFLO model and finite (of order 0.5) in Eq. (2).

At first, we use the above algorithm to estimate how much the distinction between real spectrum (18) and the ideal spectrum with square isoenergy lines shows up in the possibility of superconductivity coexisting with ferromagnetism. Figure 2 illustrates the dependence of L on the wave vector q in the upper right quadrant of the momentum plane (for $\mathbf{q}$ directed along the

$$\mathbf{q} = \frac{1}{\sqrt{2}}\,(q, q)\ \text{diagonal, as in the case considered above)}$$

as calculated for $I = 0.02$ eV, $\gamma_0 = 0.001$ eV, various val-

ues of t_2, and filling factor $n = 1.14$. The corresponding isoenergy lines are shown in the inset. The presence of sharp maxima is the salient feature of these curves. For a nonzero value of t_2, two maxima appear due to the coincidence (after shifting by I and q) of the different regions on the complicated Fermi contour. Only the states corresponding to the absolute maximum of $L(q)$ can be realized. One can see from Fig. 2 that L_{max} increases with t_2 and has a maximum at $t_2 = 0.2$. This is caused by the fact that the Fermi-contour shape for this value of t_2 is closest to a square (flat segments appear in the contour; see inset in Fig. 2). The maximal value of L_{max}/L_0 is 0.65.

The $L_{max}(I)$ dependences qualitatively analogous to the $\Delta(I)$ dependence given by Eq. (11) are shown in Fig. 3 for different values of t_2 and filling factors of 1.14 (electron doping) and 0.86 (hole doping); the corresponding dependences for the wave vector q_{max} are shown in the inset. It is worth noting that L_{max} is larger for the electron filling and exceeds for $t_2 = 0.2$ a value of 0.2 up to $I \approx 0.2$. Of interest is to reveal whether the advantage of electron filling is absolute, i.e., whether it occurs for any t_2 or not. The $L_{max}(t_2)$ dependences for $I = 0.05$ and filling factors of 0.86 and 1.14 are presented in Fig. 4. It follows from this figure that the hole filling is optimal only in a rather narrow interval of t_2 values, and in the remaining region, the electron filling dominates.

Similar results are obtained for $\mathbf{q} = (0, q)$, although the absolute values of L_{max} are slightly smaller than for
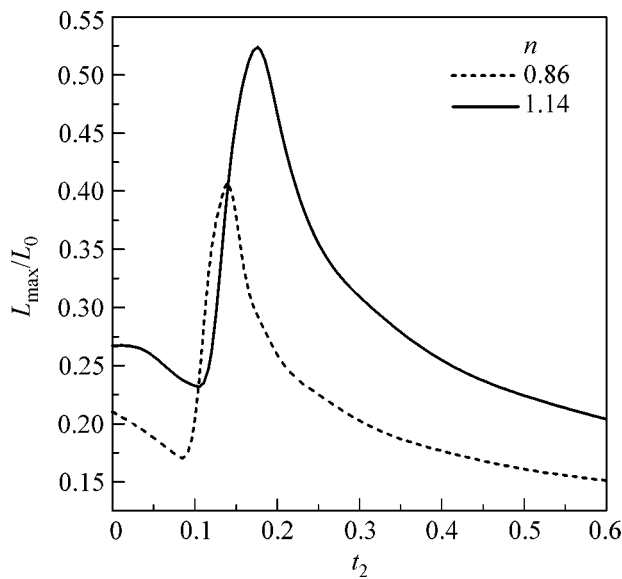
Fig. 4. The $L_{max}(t_2)$ dependences for the electron ($n = 1.14$) and hole ($n = 0.86$) doping; $I = 0.05$ eV.

the Fermi contours shifted along the $\mathbf{q} = \dfrac{1}{\sqrt{2}}\,(q, q)$ diagonal.

Of interest is to clarify whether the coexistence of superconductivity and ferromagnetism is possible in the situation where the pairing occurs with a nonzero momentum $\mathbf{K}$ even in the absence of ferromagnetism [12]. In this case, the so-called kinematic-constraint region formed by the intersection of the $\varepsilon(\mathbf{k}) < \varepsilon_F$ and $\mathbf{K}$-shifted $\varepsilon(\mathbf{k} + \mathbf{K}) < \varepsilon_F$ regions plays the decisive role. One should then consider the coincidence between the kinematic-constraint regions upon shifting by the momentum $\mathbf{q}$ and energy I. The coincidence of the $\mathbf{q}$ and $\mathbf{K}$ directions is optimal in this case. Although the meaning of the L_0 quantity is different than for the case of $K = 0$ considered above in that this length would enter the self-consistency equation in a different way, nevertheless, the L/L_0 ratio also characterizes the ferromagnetically induced superconductivity quenching. The kinematic-constraint region occupies a part of the

Fermi surface in a certain sector directed along $\mathbf{K} = (0, K)$. For this reason, when calculating L (and L_0), one should restrict oneself only to this sector. The resulting value of L_0 is smaller than the corresponding value obtained for $K = 0$, while the L/L_0 ratio proves to be larger. Therefore, the finite-$\mathbf{K}$ pairing is most favorable from the viewpoint of the coexistence of ferromagnetism and superconductivity.

REFERENCES

1. V. L. Ginzburg, Zh. Éksp. Teor. Fiz. **31**, 202 (1956) [Sov. Phys. JETP **4**, 153 (1957)].
2. J. Bardeen, L. N. Cooper, and J. R. Schrieffer, Phys. Rev. **106**, 162 (1957).
3. G. Sarma, J. Phys. Chem. Solids **24**, 1029 (1963).
4. P. W. Anderson and H. Suhl, Phys. Rev. **116**, 898 (1959).
5. A. I. Buzdin, L. N. Bulaevskiĭ, M. L. Kulič, and S. V. Panyukov, Usp. Fiz. Nauk **144**, 597 (1984) [Sov. Phys. Usp. **27**, 927 (1984)].
6. A. I. Larkin and Yu. N. Ovchinnikov, Zh. Éksp. Teor. Fiz. **47**, 1136 (1964) [Sov. Phys. JETP **20**, 762 (1964)].
7. P. Fulde and R. A. Ferrell, Phys. Rev. A **135**, 550 (1964).
8. I. Felner, U. Asaf, Y. Levi, and O. Millo, Phys. Rev. B **55**, R3374 (1997).
9. J. D. Jorgensen, O. Chmaissem, H. Shaked, *et al.*, Phys. Rev. B **63**, 054440 (2001).
10. W. E. Pickett, R. Weht, and A. Shick, Phys. Rev. Lett. **83**, 3713 (1999).
11. H. Shimahara and S. Hata, Phys. Rev. B **62**, 14541 (2000).
12. V. I. Belyavskiĭ, V. V. Kapaev, and Yu. V. Kopaev, Zh. Éksp. Teor. Fiz. **118**, 941 (2000) [JETP **91**, 817 (2000)].

Translated by V. Sakun

Quantum Bit Detector¶

M. P. Klembovsky[1, 2], M. L. Gorodetsky[1, 2, *], Th. Becker[2], and H. Walther[2]

[1] *Faculty of Physics, Moscow State University, Moscow, 119992 Russia*
[2] *Max Planck Institut für Quantenoptik, 85748 Garching, Germany*
**e-mail: gorm@hbar.phys.msu.ru*
Received March 29, 2004

We propose and analyze an experimental scheme of quantum nondemolition detection of monophotonic and vacuum states in a superconductive toroidal cavity by means of Rydberg atoms. © *2004 MAIK "Nauka/Interperiodica".*

PACS numbers: 03.65.Ta; 03.67.-a; 32.80.-t

One of the key directions of modern physics is the following challenging problem of understanding the essence of the process of quantum measurement. Of special interest in this respect are experiments with individual quantum objects. Such applications as quantum computing, quantum cryptography, and quantum teleportation, which have recently been attracting increasing attention [1], have their roots in this field. Quantum measurements and particularly experiments on the interaction of individual atoms and ions with the quantum field in a cavity are usually associated with the optical domain. With the development of the Rydberg atom technique, however, impressive results have been obtained in the microwave region [2]. This technique allows preparation and nondestructive (quantum nondemolition) repetitive measurements of Fock states with a small number of quanta in a high-Q superconductive cavity [3, 4].

In 1994, Braginsky and Khalili [5] proposed an elegant scheme employing Rydberg atoms which allowed nondestructive detection of vacuum and monophotonic states. The idea of the experiment is to use a cavity with a geometry such that the flying atom can interact twice with the field. A composite resonator comprising two sandwiched coaxial leucosapphire disks with whispering gallery modes was proposed initially with the atoms flying in between near the surfaces of the disks along their diameter. If the atom's velocity and the geometry are chosen such that the interaction time takes one half of the Rabi cycle, then the atom and the field may effectively exchange photons with a probability close to 100%. Dual interaction ensures that an atom leaves the cavity unexcited in both cases when the cavity is in vacuum and one-photon state. The only difference is the state of the atom in the central area of the cavity between the two interactions. It was suggested initially [5] that an inhomogeneous dc field be applied in this region. This electric field detects states nondestruc-

tively (state-dependent deflection). A simpler scheme for realizing nondestructive state detection was proposed later [6], and we discuss here a practical scheme for a quantum nondemolition (QND) quantum bit detector (QBD), based on the initial idea [5] with a toroidal superconductive cavity instead of sapphire disks.

The scheme of the proposed experiment is given in Fig. 1. A Rydberg atom prepared in a particular state enters the toroidal superconductive cavity. If initially the cavity is in the vacuum state of the photon field $|0\rangle$, the state of the atom does not change in the first interaction region and the central RF field (resonant with auxiliary transition) lowers the atom state to the auxiliary lowest level. If, however, the initial state of the cavity is the one-photon state $|1\rangle$, the atom absorbs the cavity photon. To provide 100% absorption of the photon, the interaction time has to be equal to one half of the
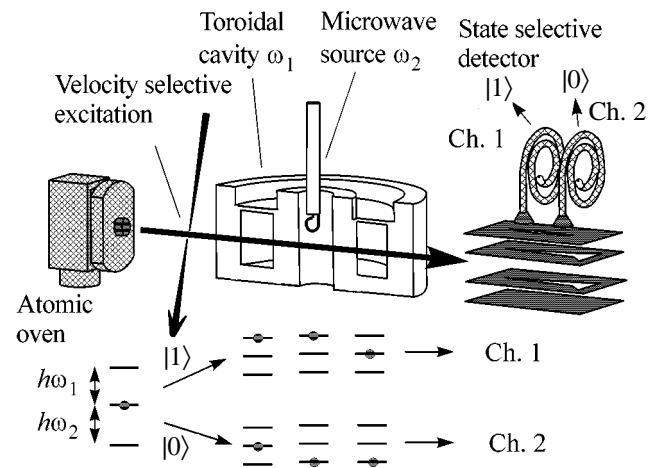

Fig. 1. Scheme of the quantum bit detector. The cavity is shown in section.

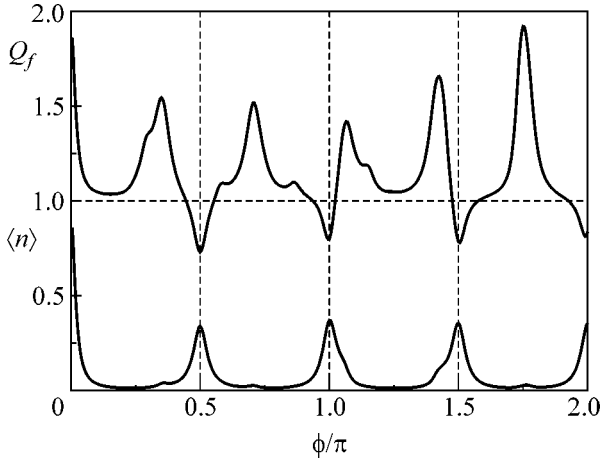¶ This article was submitted by the authors in English.

Fig. 2. Dependence of steady states of electromagnetic field in the QBD on the Rabi phase ϕ with atom rate $r = 3000$ s^{-1}, temperature $T = 1.4$ K ($\bar{n} = 0.92$), and $Q = 2 \times 10^9$. The lower curve is the mean number of photons $\langle n \rangle$, and the upper curve is the Fano factor Q_f.

Rabi cycle ($\bar{g} L/v = \pi/2$, where $\bar{g}$ is the effective Rabi frequency, L is the interaction length, and v is the velocity of the atom). When the atom is in the upper state, the central field is not resonant and the state is unchanged. During the second interaction, the atom returns the photon back to the cavity. In this way, the information about the cavity quantum state is recorded in the atomic state and the quantum state of the cavity is not destroyed. The information recorded in the atomic state can easily be read by the state-selective detector based on field ionization.

The transition between $61D_{5/2}$ and $63P_{3/2}$ levels of the ^{85}Rb Rydberg states, the cavity mode (21.456 GHz), and $61D_{5/2} \longrightarrow 59F_{7/2}$ (21.122 GHz) for the probe are planned to be used in the experiment.

The theory of the QBD based on the Jaynes–Cummings model and the standard master equation approach can be created in the same way as the theory of the micromaser field (see details in [7–9]). The basic difference is that atoms are prepared not in the excited but in the ground state and that interaction between the cavity and the atoms is more complicated.

The complete initial state P of the system atom in the ground state plus the cavity field can be written in the form

$$P = \sum_{n, m} |g, n\rangle \rho_{nm} \langle g, m|. \tag{1}$$

Three sequential interactions (the first with quantum field in the cavity in the first interaction region; the second with intermediate classical field transforming $|g\rangle$

into the auxiliary state $|f\rangle$, which is off-resonant; and, finally, the third with quantum field) will transform to

$$|g, n\rangle \longrightarrow |f, n\rangle \cos(\phi \sqrt{n})$$
$$- \frac{1}{2} i |e, n - 1\rangle \sin(2\phi \sqrt{n}) - |g, n\rangle \sin^2(\phi \sqrt{n}). \tag{2}$$

This transformation is considered ideal here, though finite efficiency can also easily be accounted for. If, as in micromaser theory, we are interested only in the evolution of the state in the cavity, ignoring the states of the atoms, we can trace over the atom states $\rho(n) \longrightarrow tr_{\text{atom}} P_{\text{after}}$, obtaining after some transformations

$$\rho \longrightarrow \cos^2(\phi \sqrt{n}) \rho(n)$$
$$+ \sin^4(\phi \sqrt{n}) \rho(n) + \frac{1}{4} \sin^2(2\phi \sqrt{n+1}) \rho(n+1). \tag{3}$$

The first term here states that the atom left the first interaction unexcited and was transformed to the auxiliary state; the second one, that the atom absorbs the photon and returns it back to the cavity; and the third is the probability of the atom leaving the cavity in excited state.

Taking into account the interaction of the cavity field with the heat bath between atom flights [7, 8], we obtain the following master equation:

$$\frac{\partial \rho}{\partial t} = -\frac{r}{4} \sin^2(2\phi \sqrt{n}) \rho(n) + \gamma \bar{n} n \rho(n-1)$$
$$- \gamma(\bar{n} + 1) n \rho(n) + \frac{r}{4} \sin^2(\phi \sqrt{n+1}) \rho(n+1) \tag{4}$$
$$- \gamma \bar{n}(n + 1) \rho(n) + \gamma(\bar{n} + 1)(n + 1) \rho(n+1).$$

Here, $\gamma = \omega/2\pi Q$ is the decay constant of the cavity and $\bar{n} = [\exp(\hbar\omega/kT) - 1]^{-1}$ is the mean number of photons in the cavity for the thermal state at temperature T. Each of the six terms in the master equation corresponds to the probability of transition to or from the level n caused by the atom or heat bath. The first three terms can be transformed to the last three terms with the replacement $n \longrightarrow n + 1$ and a change of sign. Taking into account that these first three terms also become zero for $n = 0$, one can easily obtain a steady-state solution for the QBD when $\partial\rho/\partial t = 0$:

$$\rho_{SS}(n) = \rho_{SS}(0) \prod_{m=1}^{n} \frac{4\gamma \bar{n} m}{r \sin^2(2\phi \sqrt{m}) + 4\gamma(\bar{n} + 1)m}. \tag{5}$$

The results of numerical calculations of the mean photon number $\langle n \rangle$ and relative variance (Fano factor) $Q_f = (\langle n^2 \rangle - \langle n \rangle^2)/\langle n \rangle$ according to (5) for the set of parameters achievable in the experiment are presented in Fig. 2. As is clearly seen, the QBD works as an effective cooler for the cavity field. For most of the Rabi

phase values, the state in the cavity is close to the vacuum state, except peaks corresponding to multiples of $\pi/2$. For these values of the phase, sub-Poissonian statistic of the field ($Q_f < 1$) is observed with minima of the Fano factor. This is the regime of the QND state selector. Large maxima of the Fano factor correspond to Rabi phase resonance for two-photon states, and small maxima, to three-photon states (correspondingly, $\phi = k\pi/(2\sqrt{2})$ and $\phi = k\pi/(2\sqrt{3})$).

If we now start monitoring the state of the atoms leaving the cavity with the velocity chosen to satisfy condition $\phi = \pi/2$, we can distinguish in a quantum-nondemolition way two lowest quantum n states $|0\rangle$ and $|1\rangle$—quantum bit. If dissipation in the system is absent, every new measurement of the state (every new atom) will provide the same result as the first measurement, since QND measurements are repetitive and the initial state will be preserved. If the Q factor is limited and the temperature is not zero, then, due to interaction with the heat bath, the cavity can lose and acquire photons and the lifetime of n states is limited; if, however, the rate of atoms $r \gg \gamma$, repetitive measurements are still possible and, plotting the dependence of the atom state on the time of measurement, we will observe characteristic steps of comparable length, corresponding to thermal transitions between the $|0\rangle$ and $|1\rangle$ states.

Figure 3 presents the results of a Monte Carlo simulation of this possible experiment.

Toroidal cavities with the $TE(001)$ mode were found to be most suitable for the experiment. The lines of electric field are wrapped around the center, vanishing on the cavity walls. The mode provides good atom–field coupling (Rabi frequency 47 kHz) and has axial symmetry, avoiding difficulties with mode orientation. The geometrical factor of the cavity is $\Gamma = 408\ \Omega$. Several cavities made of pure niobium (99.9%) were manufactured and tested. The cavities comprised two parts, a cup and a cover, welded by electron beam welding, chemically etched, and baked in ultrahigh vacuum at $1800°C$. The cover has a membrane for tuning the resonant frequency by mechanical and piezo squeezing. The internal dimensions of the cavities are as follows: inner diameter, 21 mm; outer diameter, 38 mm; height, 12.7 mm. The cavities were tested at 1.4 K, and a Q factor of 2×10^9 was observed. These obtained parameters were used in the theoretical calculations and simulations of the previous section. The measured frequency intervals for mechanical adjustment of the cavities (10 MHz) and piezo fine tuning (250 kHz) are appropriate for the achieved precision of cavity manufacturing.

The experimental setup for the QBD in general is similar to that described in [2, 9] and consists of a pumped ^{4}He cryostat (achievable $T = 1.3$ K) and laser system. A beam of Rb atoms is produced in an atomic oven connected to the cryostat. The cavity and tuning mechanism are fixed to the cold finger attached directly
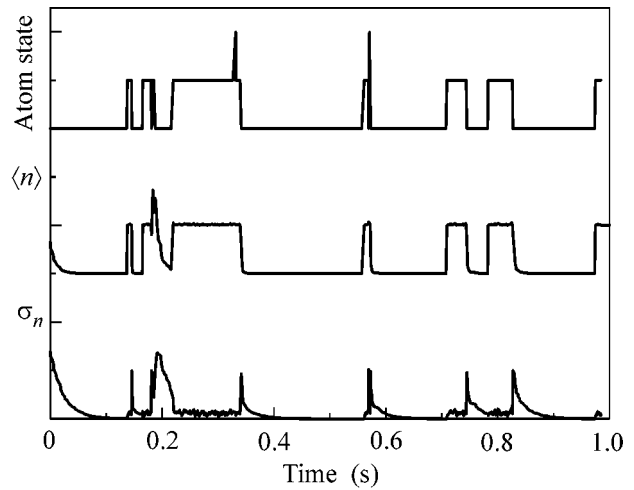

Fig. 3. Simulation of quantum bit detection regime at $\phi = \pi/2$. The parameters used in the calculations are the same as in Fig. 2. The upper curve is the state of the atoms detected, the central curve is the mean number of photons in the cavity $\langle n \rangle$, and the lower curve is the standard deviation of the QBD $\sigma_n = \sqrt{\langle n^2 \rangle - \langle n \rangle^2}$.

to the helium bath of the cryostat. The state-selective atom detector, mounted a few centimeters behind the resonator, allows atoms to be detected either in the ground and excited states or in the auxiliary and ground states. It consists of an electrostatic system creating gradient ionizing field and two channeltron electron detectors [2, 3].

The laser system for preparing the Rydberg excited state is based on a cw ring dye laser and external stabilized intracavity frequency doubler with a UV power output of about 15 mW at a wavelength of 297 nm. Since the experiment requires a defined interaction time, Doppler velocity selective excitation is employed with the laser beam inclined at an angle of about 11° to the normal angle. The laser frequency is stabilized on the same Rydberg transition using an auxiliary chamber with atomic beam.

To prepare atoms in the ground state, required for the final QBD experiment, the same laser setup can be used with the addition of an auxiliary Stark field to allow forbidden $5^2S_{1/2} \longrightarrow 61^2D_{5/2}$ transitions.

In preliminary experiments, the beam of Rydberg atoms in the excited state was guided through the cavity and detected. Count rates up to 30000 atoms/s were measured.

To sum up, the parameters already achieved in the experiment open the possibility of demonstrating repetitive QND detection of vacuum and single-photon states of a microwave field.

REFERENCES

1. *The Physics of Quantum Information: Quantum Cryptography, Quantum Teleportation, Quantum Computation*, Ed. by D. Bouwmeester, A. Ekert, and A. Zeilinger (Springer, Berlin, 2000; Postmarket, Moscow, 2002).

2. D. Meschede, H. Walther, and G. Müller, Phys. Rev. Lett. **54**, 551 (1985).

3. B. T. H. Varcoe, S. Brattke, M. Weldinger, and H. Walther, Nature **403**, 743 (2000).

4. M. Brune, S. Haroche, and S. M. Raimond, Nature **400**, 239 (1999).

5. V. B. Braginsky and F. Ya. Khalili, Phys. Lett. A **186**, 15 (1994).

6. C. Wagner, Dissertation (Univ. München, 1994).

7. B.-G. Englert, in *Proceedings of 19th Nathiagali Summer College on Physics and Contemporary Needs*, Ed. by S. A. Ahmad and S. M. Farooqi (Nathiagali, 1994).

8. P. Meystre and M. Sargent, *Elements of Quantum Optics* (Springer, Berlin, 1990).

9. G. Walther, Usp. Fiz. Nauk **166**, 777 (1996) [Phys. Usp. **39**, 727 (1996)].

Multiplex Quantum Cryptography Based on Time Coding without Interferometers

S. N. Molotkov

Institute of Solid State Physics, Russian Academy of Sciences, Chernogolovka, Moscow region, 142432 Russia
Faculty of Computational Mathematics and Cybernetics, Moscow State University,
Vorob'evy gory, Moscow, 119899 Russia
e-mail: molotkov@issp.ac.ru
Received March 3, 2004

Three fundamentally new experimental prototypes of optical fiber quantum-cryptography schemes are described. They are appreciably simpler than the available prototypes, contain fewer optical fiber components, and do not require adjustment during key generation. These cryptosystems can naturally be called quantum time-shift cryptography. They realize the B92 protocol and use a pair of nonorthogonal single-photon states as information states. One such scheme does not use fiber-optic Mach–Zehnder interferometers and, therefore, provides natural realization of the multiplex secure-key distribution regime. © 2004 MAIK "Nauka/Interperiodica".

PACS numbers: 03.67.Dd; 42.50.–p

Single-key cryptosystems provide the possibility of creating absolutely secure coding systems [1, 2]. In quantum cryptography, the secure key distribution between remote legitimate users is ensured by fundamental natural laws rather than by the limited computational or technical capabilities of an eavesdropper [3, 4]. The unconditional security of quantum cryptography in the nonrelativistic region is based, in essence, only on the Heisenberg uncertainty principle or, more formally, on the impossibility of simultaneously measuring observables described by noncommuting operators. In terms of a pair of state vectors into which classical information about the key is encoded, this means that it is impossible to gain any information about the transmitted quantum states without distorting them, provided that the latter are nonorthogonal [5]. Another fundamental quantum-mechanical exclusion closely connected to the preceding exclusion is the impossibility of copying an unknown quantum state [6]. Several various prototypes of quantum cryptosystems based on fiber-optic communication lines have been develop to date [7]. The maximal secure-key distribution distances in a quantum cryptosystem with the so-called self-compensation using Faraday fiber-optic reflectors were achieved by Japanese (100 km) [8] and Swiss (67 km) [9] groups. The available prototypes of quantum cryptosystems are mainly based on the following principles: (i) information about the key is encoded into the polarization degrees of freedom [10]; (ii) phase coding for which a Mach–Zehnder interferometer is used and information is encoded into the phase shift accumulated at the receiver and transmitter arms of the interferometer [11, 12]; (iii) quantum cryptosystems with car-

rier-frequency modulation [13]; and (iv) coherent-state quantum cryptography with the homodyne detection at the receiving end [14]. The greatest progress has been achieved in the phase-coding cryptosystems with self-compensation [8, 9] using Faraday reflectors [15]. The first local quantum cryptographic network was tested in Boston for the secure key distribution between users over a distance of 10 km (this project was ordered by the Defense Advanced Research Projects Agency) [16]. The prototypes of free-space quantum key distribution are also known [17, 18]. Among the available data [19], the longest distance is equal to 23.4 km in both daytime and at night. Quantum cryptosystems are aimed at generating and distributing secure keys between ground-based objects and satellites or between ground-based objects via satellites (this is not secreted in the western projects) [17]. According to the assessment of developers, such a system will be realized in near future, because the current level of technology is rather high and the estimated cost is quite acceptable. The above cryptosystems, particularly the schemes with phase coding and self-compensation, are difficult to realize.

Below, we describe the operation of the proposed scheme (Fig. 1). The input pulses are formed by a pulse generator circuit that excites a 1310-nm single-mode laser. This laser forms a synchronizing pulse, to which single-photon pulses of a 1550-nm single-mode laser are time-locked in a fiber-optic line (time diagram in Fig. 1). This laser sends information-state pulses, attenuated to a level of about 0.1 photons per pulse, to the fiber-optic communication channel. The delay circuit for selecting 0 or 1 is triggered by a clock generator to produce pulses that are time-shifted with respect to the
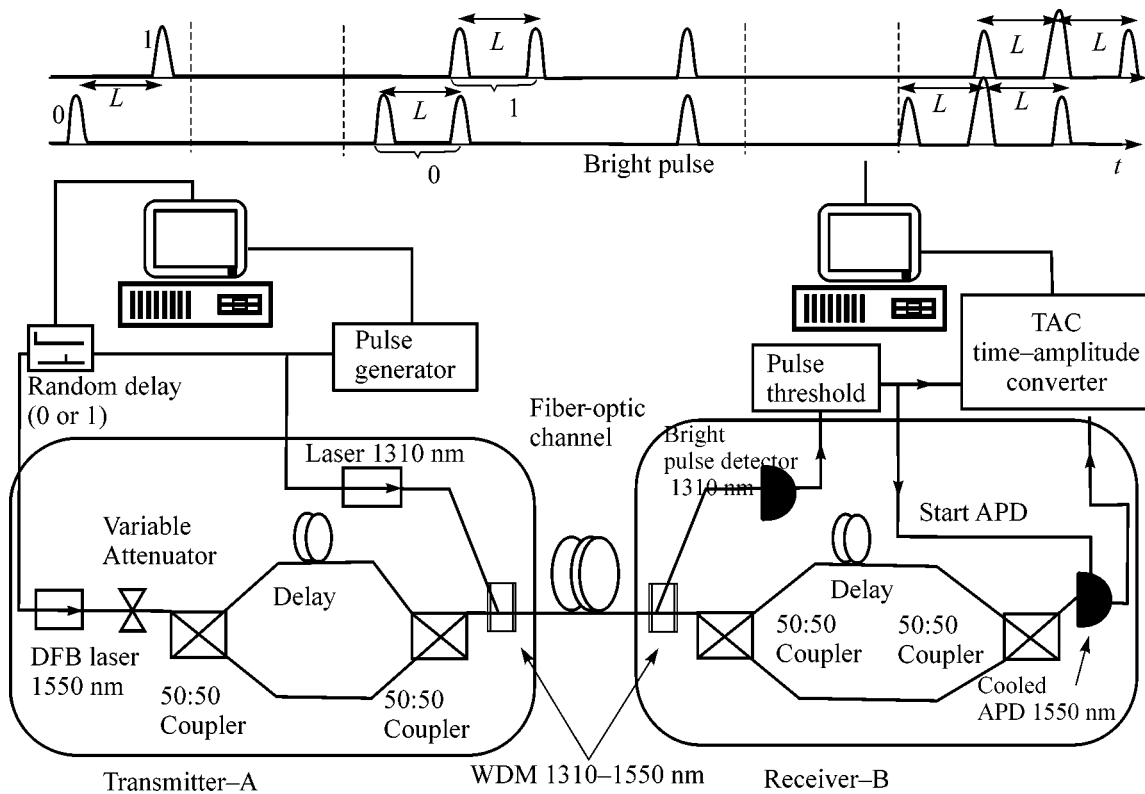
Fig. 1. Layout of a fiber-optic quantum cryptosystem based on time shifts according to the B92 protocol.

1310-nm synchronizing pulse and excite the 1550-nm laser. The time shift between the states 0 and 1 is equal to the difference in the passage times through the long and short paths in the transmitting arm of the interferometer (Fig. 1). Then, the state is fed into the input of a 50/50 fiber-optic beam splitter. Since the optical paths are different, a double-peak state (superposition of two halves of a single-photon state that are shifted due to the difference between the optical paths in the interferometer arm) arises. After the second beam splitter, the double-peak state is led to the communication channel in the wake of the synchronizing pulse from the 1310-nm laser. The synchronizing pulse in each bit is first to be led to the communication channel, and the time in each bit is measured from it. This pulse is classical (multiphoton) and is fed into a photodetector, which actuates the threshold circuit. The latter is required to exclude the spurious random triggering of the generator trigger circuit in the time–amplitude converter (TAC) circuit. After the arrival of the synchronizing pulse and the actuation of the threshold circuit, an avalanche-photodiode (APD) single-photon detector is "started." The detector operates in the trigger mode (Geiger photon-count mode). To reduce the probability of dark counts, back bias is applied to the detector at the time of arrival of information pulses. After the detection of the information pulse, the signal from the APD detector is led to the TAC, which detects the time of

triggering the APD detector. Correspondingly, the time of triggering the APD detector allows one to distinguish between states 0 and 1 (see above). According to the detection time, there are domains of conclusive result for states 0 and 1 (with the probability less than unity, because the states are nonorthogonal) and domains of inconclusive result (see time diagram in Fig. 1).

Some numerical estimates for the parameters of the system are as follows. This scheme does not require unduly accurate balance of the interferometer arms at the receiver and transmitter ends. Since the pulse duration $l \ll L$ (L is the shift, i.e., the difference between the long and short (upper and lower) paths in the interferometer arms), the perfect balance of the arms between the receiver and transmitter ends of the interferometer is not required. In other words, the halves of a state at the receiver end need not be exactly combined to form a state localized in the time window l. The shift due to the difference in the arm lengths at the receiver and transmitter ends must only not exceed L in order to distinguish between 0 and 1 in the corresponding time windows. In particular, if the duration of the input pulse is $l \sim 1$ ns, the shift between the halves is $T \sim 10$ ns. This shift arises due to the difference between the lengths of the long and short paths in the interferometer arm at the transmitter end. When recalculated to the difference between the paths in an optical fiber, it becomes $L = T(c/n) = 200$ cm ($n = 1.42$ is the index of refraction of
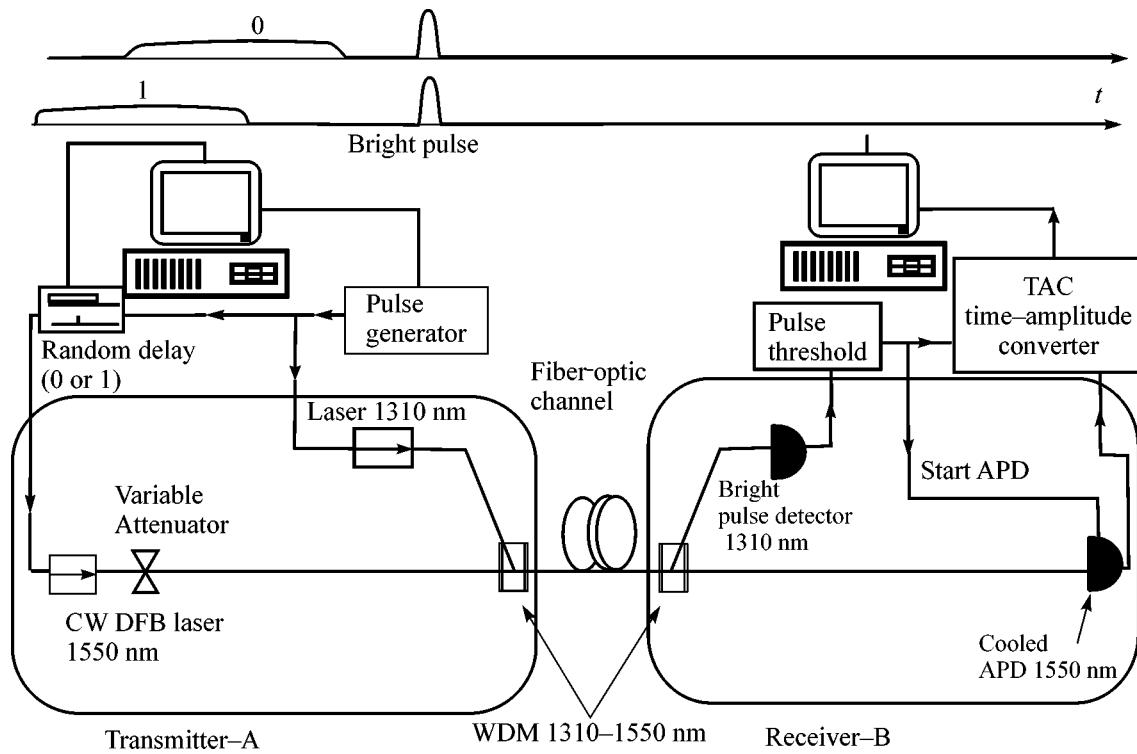
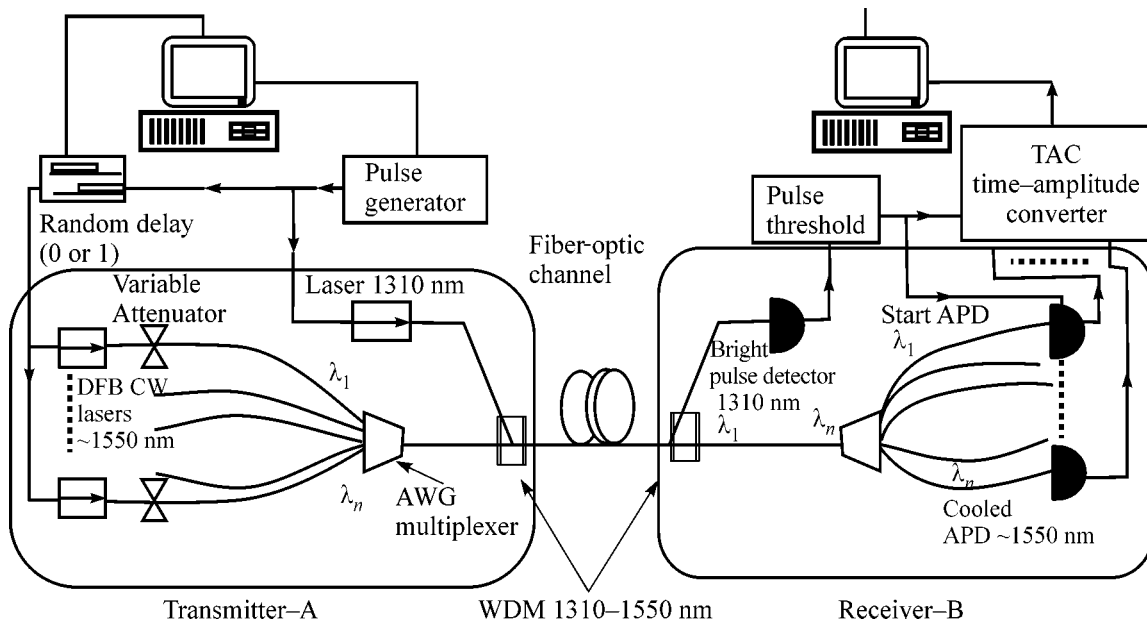**Fig. 2.** Same as in Fig. 1 but without interferometers.

Fig. 3. Same as in Fig. 1 but for a multiplex fiber-optic quantum cryptosystem.

the optical fiber). The joining of two halves at the receiver end requires the same difference in the arm lengths, with an accuracy on the order of the duration of an individual half. When recalculated to the length, it is $l \sim 20$ cm.

Since the time-shift scheme does not use phase relations and uses only the fact of overlapping, an interferometer need not be used to ensure overlapping. This possibility is a further radical simplification.

The schemes shown in Figs. 2 and 3 are also based on the time-coding idea. They differ from the above scheme only in the choice of information states. The clock pulse generator excites the laser with a wavelength of 1310 nm and the pulse duration l. After a random delay chosen between the two values, the 1550-nm CW laser is turned on. Roughly speaking, the CW laser is a source that either continuously operates and has a given output power or is nearly turned on (is slightly below the generation threshold). Under direct modulation, the application of an additional voltage step with the duration $L \gg l$ to the CW laser induces a signal in the fiber-optic communication line (see time diagram in Fig. 2). Thus, a voltage step shifted with respect to the synchronizing pulse in different bits gives rise to a pair of nonorthogonal (overlapping) states in the communication channel (see Fig. 2). The line width in good CW lasers with quantum wells can reach several hundred kilohertz. For our purposes, a duration of 20 ns (correspondingly, a CW laser line width of 10^7 Hz) suffices for the information state. It is senseless to take too long information states, because the APD detector must be back biased during this time, which increases the probability of spurious dark counts.

The block scheme operates in a similar way. The clock generator excites through the pulse-forming circuit the 1310-nm laser that produces a short synchronizing pulse. The sampling circuit for information states is simultaneously turned on. Depending on the state (0 or 1) of the random number generator, this circuit forms a driving current pulse that is shifted with respect to the synchronizing pulse by different time delays. When the synchronizing pulse arrives at the receiver end, the threshold circuit is triggered. It synchronizes the start of the TAC and applies back bias to the APD detector. The instant of time at which the APD detector comes into action is recorded through the TAC to memory.

This scheme can be naturally generalized to the multiplex case with the separation of channels according to wavelengths. Figure 3 shows the layout of a multiplex cryptosystem operating similarly to the scheme described above. The only change is the introduction of a multiplexer (diffraction grating on a waveguide array) that allows the states with different wavelengths to be led to one fiber-optic cable at the transmitter end and separated into different channels at the receiver end.

Let us give a brief comparative analysis of two fiber-optic schemes of quantum cryptography that are based on phase coding. At present, these schemes provide the maximal communication distances. The main advantage of this scheme over the phase-coding scheme, where the information is encoded into the phase difference, i.e., into the difference in the differences between the arm lengths of the interferometers at the receiver and transmitter ends, is that the accuracy of this difference must be a fraction of a wavelength. In other words, the difference of the differences between the arm lengths of interferometers located several tens of kilometers apart must be a fractions of a micron; otherwise, the scheme will not operate. Because of the strict requirements to the accuracy of path difference, polarization control must be used, which complicates the scheme and reduces its operation speed. The birefringence, responsible for different propagation speeds of radiation beams with different polarization components, leads to a spurious phase incursion. If this incursion is not compensated, the phase-coding scheme does not work at long distances. To remove this spurious effect, additional Faraday reflectors are used. Comparison should be made for the phase-coding scheme with self-compensation using Faraday reflectors. The maximal distances in quantum cryptosystems are reached in the schemes with self-compensation using Faraday reflectors. Besides the aforementioned fine items in realization, these schemes include additional optical fiber components. The Faraday reflectors solve the birefringence problem. The spurious phase incursion acquired by the different polarization components propagating from the transmitter to the receiver ends is compensated in the back passage. The above requirements to the arm adjustment are retained in this scheme. The scheme can operate at long distances (up to 100 km, as was demonstrated by the Japanese group) owing to the elimination of the spurious birefringence effects. However, due to the two-pass character of the scheme, it is more sensitive to attenuation, because it doubles the effective length of the optical fiber for the same physical distance of key transmission. Therefore, this scheme is more complicated and expensive than the preceding phase-coding scheme without self-compensation. One more drawback of the quantum cryptosystem with self-compensation using Faraday reflectors is its lower cryptoresistance to the specific Trojan-horse attack.

Note that the phase-coding schemes cannot be simply generalized to the multiplex case, because the phase-difference incursions are different for different wavelengths. Thus, the above schemes of quantum cryptographic prototypes have the following fundamental advantages over the available schemes:

Simplicity of the fiber-optic interferometer (Fig. 1) that does not require accurate (to a fraction of a micron) balance of its arms and continuous adjustment in operation. Electronics for the control of optical phase modulators in the interferometer arms are not required.

Time-coding schemes can be designed even without the use of fiber-optic Mach–Zehnder interferometers (Figs. 2 and 3). Schemes without interferometers can naturally be extended to the multiplex regime, which can increase the key transmission rate due to an increase in the number of frequency channels and makes it possible to use a cryptosystem in local networks, where each receiver has its own wavelength.

Since the thermal stabilization and the adjustment of interferometer arms are not required, the key-generation rate is higher than in the phase-coding schemes.

Since the scheme has the one-pass character and, therefore, the losses in the optical fiber are lower, the length of the fiber-optic quantum-communication channel can be increased.

REFERENCES

1. V. A. Kotel'nikov, Report (1941).
2. C. E. Shannon, Bell Syst. Tech. J. **28**, 658 (1949).
3. S. Wiesner, SIGACT News **15**, 78 (1983).
4. C. H. Bennett and G. Brassard, in *Proceedings of IEEE International Conference on Computers, Systems and Signal Processing* (Bangalore, India, 1984), p. 175.
5. C. H. Bennett, Phys. Rev. Lett. **68**, 3121 (1992).
6. W. K. Wootters and W. H. Zurek, Nature **299**, 802 (1982).
7. N. Gisin, G. Ribordy, W. Tittel, and H. Zbinden, quant-ph/0101098; Rev. Mod. Phys. **74**, 145 (2002).
8. H. Kosaka, A. Tomita, Y. Nambu, *et al.*, quant-ph/0306066.
9. D. Stucki, N. Gisin, O. Guinnard, *et al.*, quant-ph/0203118.
10. A. Muller, J. Breguet, and N. Gisin, Europhys. Lett. **23**, 383 (1993); A. Muller, H. Zbinden, and N. Gisin, Nature **378**, 449 (1995); Europhys. Lett. **33**, 335 (1996).
11. Ch. Marand and P. D. Tounsend, Opt. Lett. **20**, 1695 (1995); P. D. Tounsend, Nature **385**, 47 (1997); IEEE Photonics Technol. Lett. **10**, 1048 (1998).
12. R. Hughes, G. G. Luther, G. L. Morgan, and C. Simmons, Lect. Notes Comput. Sci. **1109**, 329 (1996); R. Hughes, G. Morgan, and C. Peterson, J. Mod. Opt. **47**, 533 (2000).
13. P. C. Sun, Y. Mazurenko, and Y. Fainman, Opt. Lett. **20**, 1062 (1995); Y. Mazurenko, R. Giust, and J. P. Goedgebuer, Opt. Commun. **133**, 87 (1997).
14. F. Grosshans, G. Van Assche, J. Wenger, *et al.*, Nature **421**, 238 (2003).
15. M. Martinelli, Opt. Commun. **72**, 341 (1989); J. Mod. Opt. **39**, 451 (1992).
16. C. Elliot, D. Pearson, and G. Troxel, *Quantum Cryptography in Practice* (2003); quant-ph/0307049.
17. J. G. Rarity, P. R. Tapster, P. M. Gorman, and P. Knight, New J. Phys. **4**, 82.1 (2002).
18. R. J. Huges, J. E. Nordholt, D. Derkas, and C. G. Peterson, *Practical Free-Space Quantum Key Distribution over 10 km in Daylight and at Night* (2002); quant-ph/0206092.
19. C. Kurtsiefera, P. Zarda, M. Halder, P. M. Gorman, P. R. Tapster, J. G. Rarity, and W. Weinfurter, *Long Distance Free Space Quantum Cryptography* (Ludwig-Maximilian-Univ., Munich, 2002).

Translated by R. Tyapaev